

HIGH EFFICIENCY DYNAMIC PRESSURE BASED
FLOW MEASUREMENT

Zoheir Moslemi

A Thesis

in

The Department

of

Mechanical, Industrial and Aerospace Engineering

Presented in Partial Fulfilment of the Requirements

For the Degree of Master of Applied Science at

Concordia University

Montreal, Quebec, Canada

August 2017

© Zoheir Moslemi, 2017

CONCORDIA UNIVERSITY

SCHOOL OF GRADUATE STUDIES

This is to certify that the thesis prepared

By: Zoheir Moslemi

Entitled: High efficiency dynamic pressure based flow measurement

and submitted in partial fulfilment of the requirements for the degree of

Master of Applied Science (Mechanical Engineering)

complies with the regulation of the University and meets the accepted standards with respect to originality and quality.

Signed by the final examining committee:

Dr. Chang Mynguan , MIAE Chair

Dr. Ramin Sedaghati , MIAE Examiner

Dr. Maria Electrovicz , BCEE Examiner (External)

Dr. Ion Stiharu , MIAE Supervisor

Dr. Amin Changizi Co-Supervisor

Approved by _____

Dr. S.Narayanswamy, M.A.Sc Program Director Department of
Mechanical, Industrial and Aerospace Engineering

Dr. A. Asif, Dean

Faculty of Engineering & Computer Science

Date August 28, 2017

Abstract

High efficiency dynamic pressure based flow measurement

Zoheir Moslemi,

Concordia University, 2017

Over the past few decades considerable attention have been directed towards the development of different types of flow-metering techniques. High pressure drop after passing the metering device and partial obstruction of the flow represent the two most common problems for the majority of the existing flow-metering devices. The main intention of the current study was to overcome or minimize these two issues.

The principle objectives were developing a low-cost measurement system and setup to measure the flow in pipes of small diameters (0.5" to 4"), and performing an analytical / numerical model that enables to extract the distinction of the dynamic pressure throughout the flow.

Both analytical and numerical solutions of the fluid flow inside the pipe indicate forming of a parabolic velocity profile across the pipe in the fully developed flow region. Dynamic pressure variation due to velocity change across the pipe is used as the fundamental measurement principle in this work. The equipped cantilever beams with piezo-resistive materials are used as sensor for detecting the induced signals in three different levels across the pipe. The collected signals are used to reconstruct the parabolic velocity profile. Further, the integration of the parabolic profile in the cross-section area of the pipe will yield to the flow value.

The constructed sensors with strain gages are connected to a Wheatstone-Bridge. The resistance variation due to the strain changing in cantilever platform converts to voltage variation by the Wheatstone-Bridge. Signal amplification and filtering are carried out by a dedicated circuit board.

The work was extended to inkjet-printing of the conductive ink which is introduced as an alternative method for piezoresistive sensor fabrication. Easiness and fast-fabrication process are two important factors which give ability to mass production of low-cost piezoresistive sensors.

Acknowledgment

I would first like to express my sincere thanks and gratitude to my thesis supervisor Dr. Ion Stiharu for his endless support and providing the opportunity to work under his supervision. I appreciate all of his encouragements, comments and suggestions. The door to Dr. Stiharu office was always open to guide me in every faced troubles.

I would like to appreciate my Co-supervisor Dr. Amin Changizi for his guidance and support. Thank you Dr. Amin for your extremely valuable suggestions in pursuing this thesis.

I would also like to thank my family; I wouldn't finish the thesis without them. My Special appreciation to my lovely wife, Saeideh, and my sweet daughter, Denise, for all their love and support. My parents have been always an inspiration to me, thanks father and mother.

I would like to extend thanks to Mr. Dan Juras for his help and friendly discussion. I would also like to thanks Mr. Dave Chu, Mr. Gilles Huard and Mr. Dmitry Rozhdestvenskiy. Special thanks are reserved for Charlene Wald and Maureen Thuringer.

Table of Contents

Chapter 1 Introduction and rationale	1
1.1 Introduction.....	2
1.2 Thesis layout	5
1.3 Content of the thesis.....	7
Chapter 2 Principles and measuring methods of fluid flow	10
2.1 Fluid flow measurement	11
2.1.1 Differential pressure flow-meter.....	11
2.1.2 Velocity flow-meters	16
2.1.3 Positive displacement flowmeter.....	31
2.1.4 Coriolis flowmeter	31
2.2 The proposed principle of flow measurement.....	36
Chapter 3 Modeling and Simulation of the Measurement Method	39
3.1 Introduction.....	40
3.2 The Entrance Region	42
3.3 Principles of the Model	52
3.3.1 Dynamic pressure variation in the cross-section of the pipe.....	53
3.3.2 The configuration of the design	57
3.4 Analytical principle of induced deflection to the beam by the flow.....	61

3.4.1 Structural phase theory	61
3.4.2 The fluid phase	64
3.5 The results of the numerical simulation	70
3.5.1 Computational fluid dynamic (Fluent).....	71
3.5.2 Static structural solver	76
3.5.3 Analytical induced deflection to a cantiliver beam under imported pressure collected from the numercial approach.....	78
Chapter 4 The Sensor	82
4.1 Miniature strain gage	83
4.1.1 Strain gage types	83
4.1.2 Strain gage location	85
4.1.3 Strain gage mounting	88
4.2 Sensor measurement	94
4.2.1 Wheatstone bridge construction.....	95
4.2.2 Filtering and amplification.....	97
4.3 The experimental set-up and the results	99
4.3.1 Triple sensor non-linear measurement.....	103
4.3.2 Alternative linear single sensor approach.....	108
Chapter 5 The conductive ink printed sensor	111

5.1 Inkjet printing	112
5.2 Color forming process	115
5.3 The properties of inkjet printing	116
5.3.1 Surface tension & viscosity	116
5.3.2 Surface resistance.....	119
5.4 Halftoning	121
5.5 Sensor construction.....	123
5.5.1 Compatible ink and printer.....	123
5.5.2 Refillable cartridge and coated sheet.....	124
5.5.3 Printing with conductive ink.....	126
5.5.4 Measurement the achieved resistance	130
5.5.5 Gage factor setup and calculation.....	131
5.6 Experiments and results.....	134
Chapter 6 Conclusion	141
6.1 Conclusion	142
6.2 Contribution to inkjet printing technique as an alternative method of beams instrumentation	144
6.3 Future work	144
References	146

Appendix A.....	156
Appendix B.....	159

List of abbreviations

MEMS	Micro-electromechanical system
IC	Integrated Circuits
TR	Turndown Rate
Mach	Ratio of the speed of a body to the speed of sound
Re	Reynolds number
RMSE	Root mean square error
RMSPE	Root mean square percentage error
CFD	Computational fluid dynamic
SST	Shear Stress Transport
GF	Gage factor
TCR	Thermal coefficient of resistance
CYM	Cyan-Yellow-Magenta color
min	Minimum/ Minute
max	Maximum

List of Symbols

P_i	Pressure in cross-section i / Pressure at point i
P_s	Static pressure
P_D	Dynamic pressure
dh	Height difference
A_i	Area of the i cross-section of the pipe
r	Radius of the pipe
θ	Contact angle / Twist angle / Cylindrical coordinate
ρ	Density
μ	dynamic viscosity
S	Signal
Q	Flow
Q_0	Known flow volume
Q_m	Mass flow rate
x	Cartesian coordinate
y	Cartesian coordinate
z	Cartesian coordinate
c	speed of sound in the fluid
v	flow velocity
ρ_L	density of the manometer liquid
g	Acceleration of gravity

h	Heat transfer coefficient / Thickness of polyester sheet
A_w	Area of the hot-wire
R_w	resistance of hot-wire
R_L	serial resistor with hot-wire
R_g	Gage Resistance
R_s	Sheet resistance
T	Temperature
T_w	temperature of the wire
T_f	temperature of the fluid
St	Strouhal number
f	frequency
d	Width of the bluff body / Diameter of pipe
V_{ave}	average velocity of the fluid
t_u	Time of the transmitted ultrasonic signal in upstream side of the fluid flow
t_d	Time of the transmitted ultrasonic signal in downstream side of the fluid flow
R	Resistance
ΔR	resistance variation
Y	Expansion of compressible gases
C_{Meter}	Meter coefficient in Orifice flowmeter
V_{out}	Output voltage
V_{in}	Input voltage
I	Current / Bending moment

N_f	total frequency numbers
C_{flow}	flow coefficient
w	Width
L	Length of beam / pipe/ distance between two transducer
ε	Strain / specific turbulent dissipation rate
B	Magnetic field
E	Young modulus of elasticity / induced voltage
ν	Poisson's ratio
m	Slop of the line
r	Cylindrical coordinate
z	Cylindrical coordinate
Z	Area under the graph
C	Centigrade
Ω	Angular velocity / Ohm
ω	Excited frequency to the system / Turbulent frequency
a_c	Coriolis acceleration
F_c	Coriolis Force to the pipe
T_c	Induced twist moment by Coriolis effect
C_u	Damping coefficient
I_u	Inertia of the U-shaped pipe filled with fluid
K_u	The stiffness of the elastic system
u	Velocity of fluid in x-direction

v	Velocity of fluid in y-direction
w	Velocity of fluid in z-direction
k	Kinetic energy
K	Correction factor
δ	Deflection of the beam
σ	Surface tension

List of Figures

FIGURE 1.1. VALVE DATED THE ROMANS TIME – FOUND IN OLD ROME..... 3

FIGURE 2.1. ORIFICE PLATE METHOD OF MEASURING FLOWRATE (ADAPTED FROM [10])..... 12

FIGURE 2.2. VENTURI TUBE FLOW METERING TECHNIQUE (ADAPTED FROM [10])..... 14

FIGURE 2.3. FLOW NOZZLE METHOD OF FLOWMETER (ADAPTED FROM [2]) 15

FIGURE 2.4. ROTAMETER PRINCIPLE IS BASED ON DYNAMIC EQUILIBRIUM BETWEEN 16

FIGURE 2.5. VELOCITY PROFILE IN LAMINAR AND TURBULENT FLOW (ADAPTED FROM [11])..... 17

FIGURE 2.6. VELOCITY BASE MEASURING: PITOT TUBE (ADAPTED FROM [2]) 18

FIGURE 2.7. THE SCHEMATICS OF THE HOT-WIRE SENSING PLATFORM [16, 17] 21

FIGURE 2.8. WHEATSTONE-BRIDGE PRINCIPLES 22

FIGURE 2.9. CONSTANT TEMPERATURE TECHNIQUE..... 23

FIGURE 2.10. SCHEMATIC OF TURBINE FLOW METER PRINCIPLE (ADAPTED FROM [18]) 24

FIGURE 2.11. VORTEX FLOWMETER PRINCIPLE 26

FIGURE 2.12. THE GENERATED TRAIL OF SWIRLS WHICH PROPAGATED BY 180^0 PHASE DIFFERENCES FROM EACH SIDE
..... 26

FIGURE 2.13. ELECTRO-MAGNETIC FLOWMETER (ADAPTED FROM [8]) 28

FIGURE 2.14. ULTRASONIC DOPPLER FLOWMETER (ADAPTED FROM [21]) 30

FIGURE 2.15. ONE CYCLE OF PD-FLOWMETER (ADAPTED FROM [22])..... 31

FIGURE 2.16. CORIOLIS FLOWMETER, THE FLOW SPLIT INTO TWO U-SHAPED TUBE; THE DISPLACEMENT SENSORS 32

FIGURE 2.17. FRONT VIEW OF THE SYSTEM; A) NON-FLOW CONDITION; B) FLOW CONDITION (ADAPTED FROM [25])
..... 33

FIGURE 2.18. PHASE DIFFERENCES ΔT BETWEEN NO-FLOW AND FLOW CONDITIONS.	33
FIGURE 2.19. CORIOLIS EFFECT OF THE U-SHAPED PIPE	34
FIGURE 2.20. FRONT VIEW OF THE U-SHAPED PIPE.	36
FIGURE 2.21. PARABOLIC VELOCITY PROFILE AND THE CONTROL POINTS	37
FIGURE 3.1. THE VELOCITY BOUNDARY LAYER DEVELOPMENT IN A PIPE (ADAPTED FROM [11]).	43
FIGURE 3.2. THE WALL SHEAR STRESS VARIATION IN THE FLOW DIRECTION (ADAPTED FROM [11]).....	44
FIGURE 3.3. UNIFORM VELOCITY PROFILE AS INITIAL CONDITION AT THE ENTRANCE OF THE PIPE.....	46
FIGURE 3.4. THREE DIFFERENT VELOCITY VALUES WITH ZERO VELOCITY IN WALL MAKE HALF-PARABOLIC VELOCITY PROFILE.....	47
FIGURE 3.5. THE INVESTIGATED CROSS SECTIONS BETWEEN 10D AND 22.8D AT REYNOLDS NUMBER EQUAL TO 80000	48
FIGURE 3.6. SCHEMATICS OF COMPARING THE VELOCITY VALUES UNDER THE INVESTIGATED VELOCITY PROFILES AT THE SAME LOCATION VS. THE REFERENCE PROFILE.	49
FIGURE 3.7. DIFFERENT GEOMETRY OF CANTILEVER BEAMS	58
FIGURE 3.8. SCHEMATIC VIEW OF SENSOR RING	59
FIGURE 3.9. BENDED CANTILEVER BEAM INDUCED BY FLOW.....	60
FIGURE 3.10. THE PRESSURE ACTED UPON CANTILEVER BEAM INSIDE THE PIPE (TRIANGULAR DISTRIBUTED LOAD). 62	
FIGURE 3.11. BENDING MODEL OF EULER'S BEAM.....	63
FIGURE 3.12. THE CONFIGURATION OF THE CASE STUDY	64
FIGURE 3.13. THE STATIC PRESSURE VALUE IS DECREASING LINEARLY FROM P1 TO P2.	67
FIGURE 3.14. THE SCHEMATIC VIEW OF SENSOR RING INSIDE THE PIPE	70
FIGURE 3.15. TETRAHEDRAL MESH AT THE SENSOR LOCATION SECTION	72

FIGURE 3.16. MESH QUALITY AROUND MICRO-CANTILEVER BEAM & PIPE.....	73
FIGURE 3.17. SKEWED AND IDEAL SHAPES OF THE QUADRILATERALS AND TRIANGLES	73
FIGURE 3.18. MESH QUALITY ACCORDING TO THE SKEWNESS FACTOR	74
FIGURE 3.19. SOLUTION CONVERGENCE YIELDS BY ANSYS FLUENT	75
FIGURE 3.20. THE FLOW HITS THE BEAM AND CREATES VORTEX BEHIND THE BEAM.....	76
FIGURE 3.21. INDUCED DEFORMATION IN CANTILEVER BEAMS DUE TO WATER FLOW	77
FIGURE 3.22. INDUCED ELASTIC STRAIN INTENSITY IN CANTILEVER BEAMS DUE TO WATER FLOW	77
FIGURE 3.23. A) STRAIN INTENSITY INDUCED IN 18.4 LITRE FLOW B) STRAIN INTENSITY INDUCED IN 1.84 LITRE FLOW	78
FIGURE 3.24. INDUCED PRESSURE DISTRIBUTION TO THE CANTILEVER BEAM.....	79
FIGURE 3.25. THE SCHEMATIC OF IMPORTED PRESSURE FROM THE NUMERICAL SOLUTION EXTRACTED FROM THE FLOW SIMULATION	80
FIGURE 3.26. THE MAXIMUM DEFLECTION FOR THE CURRENT CASE STUDY (THE MAXIMUM DEFLECTION IS 0.094 μ m)	81
FIGURE 4.1. SCHEMATIC VIEW OF A FOIL STRAIN GAGES	83
FIGURE 4.2. THE SELECTED DIMENSIONS FOR THE THREE CANTILEVER BEAMS, IN ORDER TO INSTALL IN A 4" PIPE...	86
FIGURE 4.3. THE INDUCED STRAIN TO THE 20MM CANTILEVER BEAM UNDER THE 10 PA UNIFORM DISTRIBUTED LOAD (HIGHEST STRAIN AREA L/4)	87
FIGURE 4.4. THE INDUCED STRAIN TO THE 20MM CANTILEVER BEAM UNDER THE 10 N POINT LOAD AT THE FREE-END (HIGHEST STRAIN AREA APPROXIMATELY IS L/3)	87
FIGURE 4.5. SCHEMATIC VIEW OF THE STRAIN GAGE INSTALLATION LOCATION ON THE CANTILEVER BEAM	88
FIGURE 4.6. Z70 SUPERGLUE AND PACKAGE EQUIPMENT	89

FIGURE 4.7. TWO MOUNTED STRAIN GAGES A) THE FOIL GAGE WITH 350 Ω RESISTANCE	91
FIGURE 4.8. MOUNTED FOIL STRAIN GAGE ON MELLINEX WITH THE SOLDERED WIRES TO THE PADS	92
FIGURE 4.9. THE HALF-CYLINDERS MANUFACTURING PROCESS.....	93
FIGURE 4.10. THE INSTALLED SENSORS IN THE SEGMENT OF PIPE	94
FIGURE 4.11. BASIC WHEATSTONE BRIDGE- BASE MEASUREMENT BLOCK DIAGRAM	95
FIGURE 4.12. WHEATSTONE BRIDGE WITH SINGLE ELEMENT VARYING	96
FIGURE 4.13. THE PHIDGET-BRIDGE INTERFACE BOARD.....	97
FIGURE 4.14. THE COMMUNICATING WINDOW OF SOFTWARE WITH PHIDGET-BRIDGE.....	98
FIGURE 4.15. THE CONSTRUCTED WHEATSTONE BRIDGE BOARD ALONG WITH THE PHIDGET-BRIDGE.....	99
FIGURE 4.16. A) PVC PIPE ADHESIVE. B) REGULATOR. C) CONNECTED FAN TO THE PIPE-LINE	100
FIGURE 4.17. THE ENTIRE SET-UP OF EXPERIMENT	101
FIGURE 4.18. THE WIRES FROM THE SENSOR ARE CONNECTED TO THE WHEATSTONE BRIDGE	102
FIGURE 4.19. THE USB CABLE CONNECTED AND RECOGNIZED BY THE COMPUTER	103
FIGURE 4.20. CONFIGURATION OF THE MEASUREMENT IN EXPERIMENTAL PHASE.....	104
FIGURE 4.21. THE AREA UNDER THE HALF PARABOLIC VELOCITY PROFILE IS NAMED AS Z.....	105
FIGURE 4.22. THE MEASURED SIGNALS FROM SENSORS IN DIFFERENT FLOWRATES	106
FIGURE 4.23. BRIDGE # 2 IS CALIBRATED. A) CALIBRATED IN 74 AND 57 CFM. "CONVERTED VALUE = 66.37", B) MEASURED VALUE BY REED FLOW-METER "64.284 CFM"	110
FIGURE 5.1. CONTINUOUS INKJET PRINTING PROCESS (ADAPTED FROM [64])	113
FIGURE 5.2. DROP-ON-DEMAND INKJET PRINTING TECHNOLOGY " PIEZO & THERMAL"	114
FIGURE 5.3. COLOR COMPOSITION IN INKJET PRINTING	116
FIGURE 5.4. SCHEMATIC OF SURFACE ENERGY EQUILIBRIUM AND CONTACT ANGLE IN DROPLET	117

FIGURE 5.5. SURFACTANT INFLUENCE ON SURFACE TENSION (A) 12 ML DROPLET OF WATER (B) 12 ML DROPLET OF WATER MIXED WITH ETHANOL 70%.....	119
FIGURE 5.6. HALFTONE DOTS. B: HUMAN EYE SEEING ABILITY FROM SUFFICIENT DISTANCE.....	121
FIGURE 5.7. THE DIFFERENT RECOMMENDED ANGELS FOR CMYK (ADAPTED FROM [64])	122
FIGURE 5.8. THREE DIFFERENT COLOR RESULTS BY THE SAME COLOR COMPOSITION (ADAPTED FROM [64])	123
FIGURE 5.9. REFILLABLE CARTRIDGES PRODUCED FROM INKOWL COMPANY	125
FIGURE 5.10. FILLING FIVE CARTRIDGES WITH CARBON AND SILVER INKS	126
FIGURE 5.11. THE SCHEMATIC VIEW OF THE PRINTED RESISTOR	127
FIGURE 5.12. A) COLOR COMPOSITION ON COREL SOFTWARE B) PRINTED RESISTORS ON COATED POLYESTER....	128
FIGURE 5.13. THE LAYOUT DESIGN OF INKJET PRINTING THE SENSOR AND WHEATSTONE BRIDGE.	129
FIGURE 5.14. THE FABRICATED SENSOR AND WHEATSTONE-BRIDGE IN ONE-TIME INKJET PRINTING.....	129
FIGURE 5.15. THE MEASUREMENT JIG OF THE PRINTED RESISTORS	130
FIGURE 5.16. THE CONFIGURATION OF THE CANTILEVER BEAM UNDER THE POINT LOAD	131
FIGURE 5.17. DIMENSIONS OF THE CANTILEVER BEAM AND U-SHAPED INKJET-PRINTED RESISTOR	132
FIGURE 5.18. THE IMAGE OF THE U-SHAPED RESISTOR A) AT THE COREL-SOFTWARE B) INKJET-PRINTED RESISTOR	133
FIGURE 5.19. THE EXPERIMENTAL SETUP FOR GF-MEASUREMENT. A) BEFORE DEFLECTION B) AFTER DEFLECTION	134
FIGURE 5.20. COMPARISON BETWEEN RESISTORS No. 7 & 8.	137
FIGURE 5.21. COMPARISON BETWEEN RESISTORS No. 1 & 3.	137
FIGURE 5.22. COMPARISON BETWEEN RESISTORS No. 2 & 6.	138
FIGURE 5.23. THE MICROSCOPIC VIEW OF THE RESISTOR.....	139

List of Tables

TABLE 1.1. COMMON TYPES OF FLOW MEASURING SYSTEMS.....	6
TABLE 3.1. VELOCITY VALUE VARIATION IN DIFFERENT CROSS-SECTIONS ON VELOCITY PROFILE PLOT (RE 80000)..	50
TABLE 3.2. DYNAMIC PRESSURE VALUE, COMPARISON BETWEEN ANALYTICAL AND NUMERICAL RESULTS.	56
TABLE 3.3. DISORDERED AREA-PERCENTAGE BY CANTILEVERS.....	60
TABLE 4.1. COMPARISON THE ERROR PERCENTAGE BETWEEN REAL VALUE AND PREDICTED VALUE BY INDIVIDUAL K VALUE FOR THE CONSTRUCTED SENSOR "K=30.3".	108
TABLE 5.1. THE RESISTANCE OF THE SELECTED COLOR COMPOSITION AT FOUR DIFFERENT PRINTING PROCESS.....	135
TABLE 5.2. THE THREE SAMPLE RESISTORS ANALYZED BY IMAGJ.....	140
TABLE 6.1. A COMPARISON BETWEEN TWO TYPES OF FLOWMETERS FROM REED COMPANY AND THE CURRENT RESEARCH FLOWMETER	143

Chapter 1 Introduction and rationale

The past few decades have marked a significant development of miniature devices. They are made using microelectronics and non-conventional technologies. Hence, they have received a suitable name: Micro-Electro Mechanical Systems (MEMS). As MEMS are made using technologies that are used in microelectronic circuitry, they are capable to embed intelligence and versatility as a complement to their size advantage. Such devices are mainly used for sensing and detection. The main beneficiaries of the technologies are the automotive, the healthcare and the telecommunications industries.

However, the small sizes make MEMS suitable for specific applications and not suitable for many others. The engineering research investigated avenues to extend the capabilities of fast and precise Integrated Circuits (IC) within the larger devices. Thus, associated technologies have been created and developed. 3D printing, PCB printing or printing of electronic circuits on flexible substrate represent only few of such technologies that enable some of the above mentioned objectives. This thesis will present a potential application of the conductive ink printing for flow measurement in small size pipes.

1.1 Introduction

The microelectronics circuits carry about 60 years of history. Over this time, one finding was generalized enounced – the substrate for the implementation of the active circuits needs to be a semiconductor material. Silicon was the most suitable candidate given the abundance of SiO_2 material on the earth. Si carries significant advantages but its properties may also play as disadvantages in some applications [1].

The brittleness of Si makes it unsuitable with many sensing devices at larger scale. This condition pointed towards the possibility of the implementation of some modified specific technologies associated with MEMS fabrication to other substrates. For an example, polymer based substrates could cover for applications where compliance is required and the high sensitivity achieved through the reduced stiffness of the structure. Hence, one of the intentions of this work is to prove the capability to achieve practical flow measurement using some of the technologies used in nonconventional fabrication.

The last two decades have proved that the old fashion technologies need to update. There are parts such as valve that conceptually, are same for about 2000 years. The problem does not stay with the valve, which was quite well conceived at the time. The problem comes with the capability of the valve to be controlled.



Figure 1.1. Valve dated the Romans time – found in old Rome
(Pipes and Valves of Ancient Rome – Enzo Faisstelli, Rome, 1972)

More and more processes and operations are required to be controlled on line, remotely. High accuracy is required to flow measurement in pharmaceutical or food industries. To keep competitive, an industry needs to adapt to the market requirements.

One of the main objectives of this work is to propose some low cost means to measure the flow in small diameter pipes which are usually not equipped with valves or other devices which enable them with the capability of measuring flow. Throughout this thesis new directions of investigation have been investigated. These directions resulted from the findings associated with the present work. The directions will be discussed in the future work at the end of this thesis.

While planning for some means to measure flow, one has to consider phenomena associated with the effect of flow directed within a pipe. It is desired that the measurement principle to be carried out into a steady environment. This need points towards the laminar flow conditions. Moreover, one should investigate if the fluid is subjected to variations in viscosity or if the fluid

may be spited with debris or fibres. Any of the above situations will lead to a set of design solutions used to protect the sensing elements.

A second concern associated with the measurement will be triggered by the temperature variations which might produce viscosity variations as well as strain effects induced by temperature variation.

However, it is necessary to establish a principle of measurement at first. Based on that, one should analyze the possibility of flow measurement using as proposed in this work, the dynamic pressure variation within the cross section of the pipe. To avoid flow obstruction, the present solution includes small size cantilever beams that will obstruct around 2% of the flow cross section area. The beams will be instrumented such that they could meter the flow at few levels inside the pipe such that the flow could be extracted with a reasonable accuracy (~5%). The flow conditions were formulated in equations.

The final objective of this investigation is to propose a control scheme for valves used in flow circuits with the small diameter of the pipes. The variants of the proposed technologies have to be further investigated in the thesis.

Returning to the challenges posted at the beginning of the introduction, the printing of the conductive ink by inkjet-printing technology in an accurate position, will be a good idea for sensing based on piezo-resistive principle. The inkjet printing technologies are increasingly recognized as an important progressing technique in light-weight, low-cost flexible circuit board industries. Hence, in this study inkjet-printed resistor on polyester-based cantilever beam is introduced as flow-metering sensor inside a pipe.

Meanwhile, a standard approach was also investigated in this project. This method uses the miniature scale high sensitive strain gage as a signal detecting sensor. The mounting process of the tiny strain gage requires high skills and capability of accurate handling. Moreover, accurate positioning and alignments are required to achieve high sensitivity for the measurement. The strain measurement is performed through Wheatstone bridges. One of the challenges associated with this work is measuring the micro-strain induced from the deflection of beam. According to the piezo-resistive principle the generated strain on the beam will convert in resistance variation and further into micro-volt signal when processed through Wheatstone bridge circuit board. Detectable signals need to be collect from the bridge under all flow conditions and a correlation between the signals and flow needs to be carried out.

1.2 Thesis layout

The thesis is divided into five chapters, which content is outlined in the below sections. In the second chapter different types of flow-meters are briefly discussed. Generally, variation parameters of the fluid flow are used as reference for estimating the flow value. Some of the characteristics that change with flow are the pressure drop and velocity changing through the flow within the cross-sectional area. Thus, the flow-metering systems are categorized into five popular groups but not limit to them. Differential pressure flow-meter, Velocity flow-meter, Positive displacement flow-meter, Mass flow-meter and Electronic flow-meters represent the major groups of flow measuring systems.

On the other hand, some of the flow-measurement devices such as the “Electromagnetic flow-meter” is associated with both velocity and electromagnetic flow measurement principles.

Some common types of flow measurement systems are briefly compared in table 1.1.

Table 1.1. Common types of flow measuring systems

Sensor	Benefits	Drawbacks
FLOW NOZZLE [2]	<ul style="list-style-type: none"> • Applicable in slurry flow • Middle pressure loss in compare with Orifice and Venturi 	<ul style="list-style-type: none"> • Expensive than orifice • Confined pipe sizes
VENTURI [2]	<ul style="list-style-type: none"> • Pressure loss less than orifice plate • Slurry applicable system 	<ul style="list-style-type: none"> • Expensive
ORIFICE [3]	<ul style="list-style-type: none"> • Low cost • Wide industrial application 	<ul style="list-style-type: none"> • High pressure drop • Clogging by slurries
TURBINE [4]	<ul style="list-style-type: none"> • Cover wide range of flow value • High accuracy 	<ul style="list-style-type: none"> • Expensive • Pre-filtering is required
VORTEX SHEDDING [5]	<ul style="list-style-type: none"> • Independent of density, temperature, viscosity and pressure variations • Cover wide range of flow rates 	<ul style="list-style-type: none"> • Expensive
POSITIVE DISPLACEMENT [6]	<ul style="list-style-type: none"> • High accuracy • Cover wide range of flow rates 	<ul style="list-style-type: none"> • High Pressure Drop • Pre-filtering is required
CALORIMETRIC FLOWMETER (Hot-Wire) [7]	<ul style="list-style-type: none"> • Directly proportional with flow velocity variation 	<ul style="list-style-type: none"> • “Thermally conductive fluid” measuring only
ELECTROMAGNETIC FLOWMETER [8]	<ul style="list-style-type: none"> • Same measuring accuracy in vertical and horizontal direction • Applicable for slurry and corrosive fluid. 	<ul style="list-style-type: none"> • High power consumption • “Electrically conductive fluid” only like salted water.

The common problem for several flow measuring systems are the relative high-pressure drop of flow after passing the metering device and also disordering which imposed to flow by

devices. The small scale cantilever sensing platform, which is suggested in this study, has the ability to overcome both of the mentioned problems. Moreover, the inkjet printing piezo-resistive sensor is introduced as a new technique here and, due to its economic and easiness to fabricate which represents an alternative in the flow metering field.

1.3 Content of the thesis

In the first chapter of the thesis, an introduction of MEMS technology along with its benefits and drawbacks are discussed in relation with industrial applications. It is proved that, new economic fabrication process represents a logic challenge through the enhancement trend. Moreover, in thesis layout section, the brief description of few selected types of flow-meters is given.

In the second chapter, a detailed literature survey has been carried out. The survey topic includes two major parts. First, the various types of flow-meters and their categorized principles are discussed. The governing equations as well as principles of formulations are also discussed in detail. In the second part of the chapter the proposed principle of flow measurement will be explained. The flow prediction governing equation will be derived and the final form of the formulation will be introduced.

Third Chapter includes the modeling and simulation of flow through circular pipes. The analysis is used further to locate the position sensors within the pipe. The governing equation are derived. According to the existing boundary conditions is shown that the analytical solution will not be achievable. Thus numerical methods are considered. Hence, ANSYS Multiphysics

modules is used. Moreover, based on wide range of Reynolds number in this application, it is proved that locating of the sensors to measure flow requires specific constraints.

In forth chapter, micro-cantilever platforms as a detecting device are analyzed using the loads found in the previous chapter. Moreover it is shown that traditional issues of flow-metering devices which are high drop pressure and disordering the fluid flow are significantly reduced by this method. The miniaturized semi-conductor strain gage is introduced as sensors.

Another aspect of concern is positioning of the strain gauge on the beam to achieve best possible sensitivity of measurement. Thus, an analysis of the position of the strain gauges vs. the sensing beam will be investigated in this chapter. In this chapter, sensor construction process as well as amplification circuit board are explained in detail. The detected signals from cantilever beams are used for predicting the flow value based on the parabolic velocity profile equation.

In the fifth chapter, two types of inkjet printing technologies, namely “continuous and drop-on-demand Inkjet printing” are discussed. According the comparison between different types of inkjet-printing technologies, it is concluded that the drop-on-demand inkjet printing exhibit major advantages than continuous method. The principles of inkjet printing as well as their various technology are investigated. The inkjet-printable ink properties are investigated in conjunction with the printing output. One of the main features of the printed resistor is represented by the value of surface resistance. The two market available types of inkjet printable conductive ink are carbon and silver based inks. The surface resistance of the two types of ink are very much different. Silver based inks exhibit resistances in the range of 10^{-2} - to

$10^{-6} \Omega/\square$. Carbon based inks exhibit large values of surface resistance, usually ranging from 10^4 – $10^7 \Omega/\square$. This unfortunate situation makes extremely difficult to print circuits with overall resistance ranging from 100 to 700 Ω if the surface of the printed circuit represents a design constraint. The intention is to build small beams equipped with small strain gauges such that the sensing system would not interfere with the flow.

The constituency of the two types of conductive inks make them immiscible. Hence, a stoichiometric mix would not yield inks with surface resistance within the required range. However, in this paper another solution was investigated. The solution is based on the printing technology known as “Half-toning”. This printing method would not mix the inks in liquid form but in solid form, while the print pattern is on the substrate. The results obtained from inkjet printing using two different conductive inks are presented at the end of the fifth chapter.

In sixth chapter, the conclusion and future works ideas are presented, which outlined in three sections. The first section is assigned to general conclusion of the thesis as well as a brief comparison between the fabricated flowmeter in this study and the commercial flowmeter in the market. Also, contribution of the inkjet printing as an alternative method in sensor fabrication field is stated at the second part of the chapter. The final section of the chapter is discussed about suggested possible future works.

Chapter 2 Principles and measuring methods of fluid flow

As many applications require metering of liquid, fluid flow measurement systems are highly important. The main target of measuring in this regard is the accuracy. The chemical and the food industries often need very accurate controlled flow grids. This condition points to the need to ensure the capability to control the flow through valves during a process. Thus, the reproducibility has received considerable critical attention.

Typically, any flow network requires energy for running the fluid in the system. Pumps and compressors provide the driving force of the fluid through the piping system. Clearly, the sensors should exhibit small flow resistance against the flow to reduce the energy consumption and the interference with the flow.

2.1 Fluid flow measurement

There are several different phenomena which occur through and across the pipe while a fluid flows through it. These phenomena could provide hints towards measuring the flow features such as: differential pressure, velocity, dynamic pressure, and flow profile [2]. This chapter will discuss the above mentioned principles implemented in measuring devices.

2.1.1 Differential pressure flow-meter

The principle of this method is based on Bernoulli's laws. In this method the pressure drop over a measuring device is due to the pressure drop of a fluid while its flow velocity increases. This is Bernoulli principle which is quantified based on the conservation of energy which imposes that the lost work or heat transfer are negligible. Some type of restrictors associated to this method are: orifice plate, flow nozzles, Venturi tubes, and variable area "rotameters" [9].

2.1.1.1 The orifice plate method

In this measurement principle, the pressure differences are calculated between upstream and downstream side of partially obstructed pipe by an orifice plate. The orifice plate technique is simple, low-cost and it is widely used in industries [3]. One of important parameters in flowmeter devices is the "Turndown Rate (TR)", which is defined by:

$$TR = \frac{q_{\max}}{q_{\min}} \quad (2.1)$$

Where the q_{\max} and q_{\min} are the maximum and the minimum measured flow with such device. This ratio for orifice technique is 5:1, which yields relatively poor accuracy. The figure 2.1 shows a schematic of this method used to measure flowrate.

According to the figure 2.1, Bernoulli equation will be simplified to:

$$\frac{P_1}{\rho g} + \frac{1}{2g}v_1^2 = \frac{P_3}{\rho g} + \frac{1}{2g}v_3^2 + \sum f \quad (2.2)$$

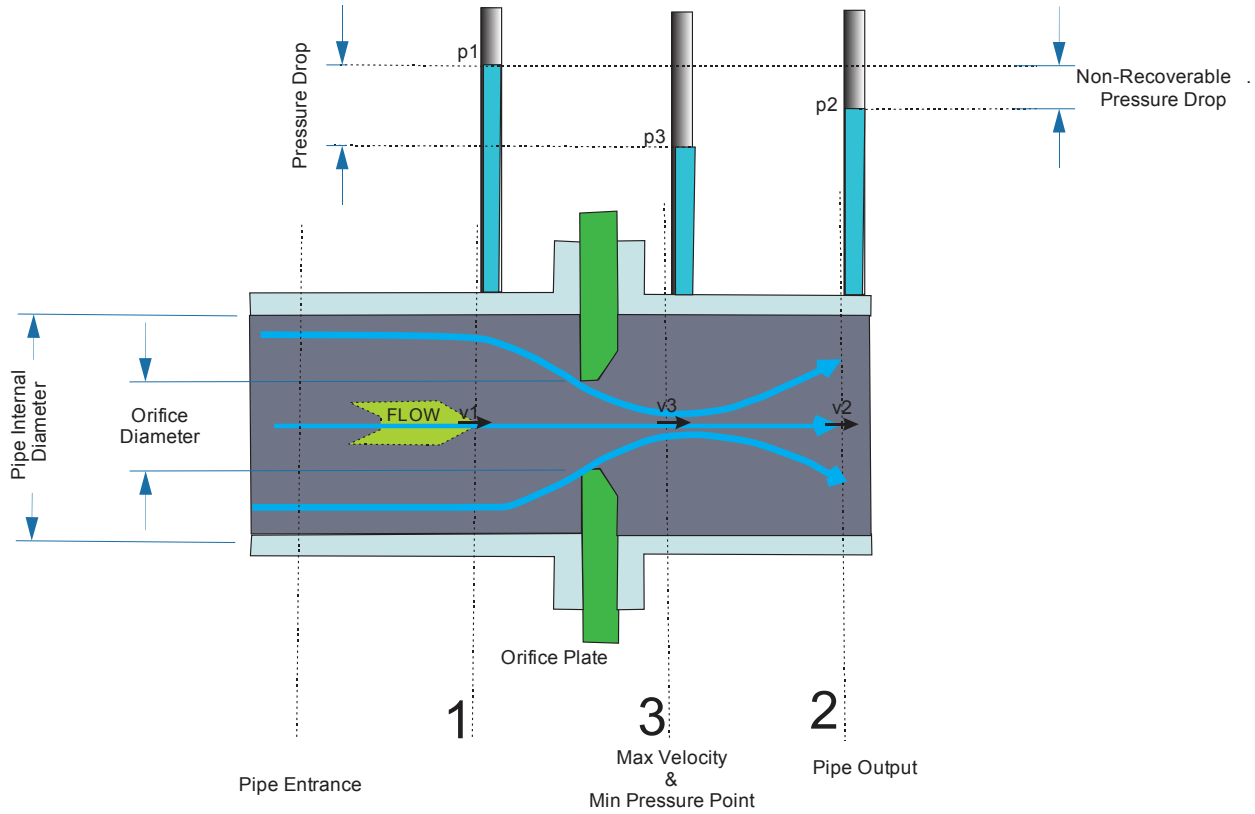


Figure 2.1. Orifice plate Method of measuring flowrate (Adapted from [10])

Where $\sum f$ is the total friction loss, which is assumed as negligible. The equation is simplified and rearranged and presented in the below format which is known as general head meter equation [11].

$$Q = A_1 V_1 = C_{\text{meter}} Y A_3 \sqrt{\frac{2(P_1 - P_3)}{\rho \left(1 - \frac{A_3^2}{A_1^2}\right)}} \quad (2.3)$$

The principle of equation 2.3, is based on the flux consistency in every cross-sections of the pipe. “Q” is flowrate. Also A, V and P are the area of cross section of the pipe, flow velocity and pressure, respectively. The indices are addressing the associated cross-section for different parameters, figure 2.1.

The meter coefficient C_{Meter} is dependent on the friction loss and it is function of ratio of cross sections and Reynolds number. The compressibility factor Y represents the expansion of compressible gases; so for incompressible fluid $Y = 1.0$. Both of these parameters can be calculated from equation 2.2 or from [12].

The term “non-recoverable pressure drop”, which is shown in figure 2.1 will be discussed below. The pressure trend after an abrupt decreasing in the vena contracta (orifice-plate location) will reach to its minimum value at 3rd cross-section P_3 , where the maximum velocity will occur V_3 . Then the flow experiences pressure rise, and reaches to its final value in 2nd cross-section “ P_2 ”. The P_2 is lower than P_1 , because of metering device resistance. The differences between the first and second pressure is known as “non-recoverable pressure drop”, which is illustrated in figure 2.1.

2.1.1.2 Venturi tube method

Reliability and simplicity are two important features of this method. Moreover, higher turndown ratio and less non-recoverable pressure drop, compare to orifice plate represent other advantages of this technique. In the Venturi tube, the flow path gradually decreases for creating the pressure difference along the device. Further the fluid is guided to a recovery exit

area to compensate the pressure loss in convergent zone. The recovered pressure is up to 80% of the initial pressure [2]. The turndown ratio for this method is around 10:1.

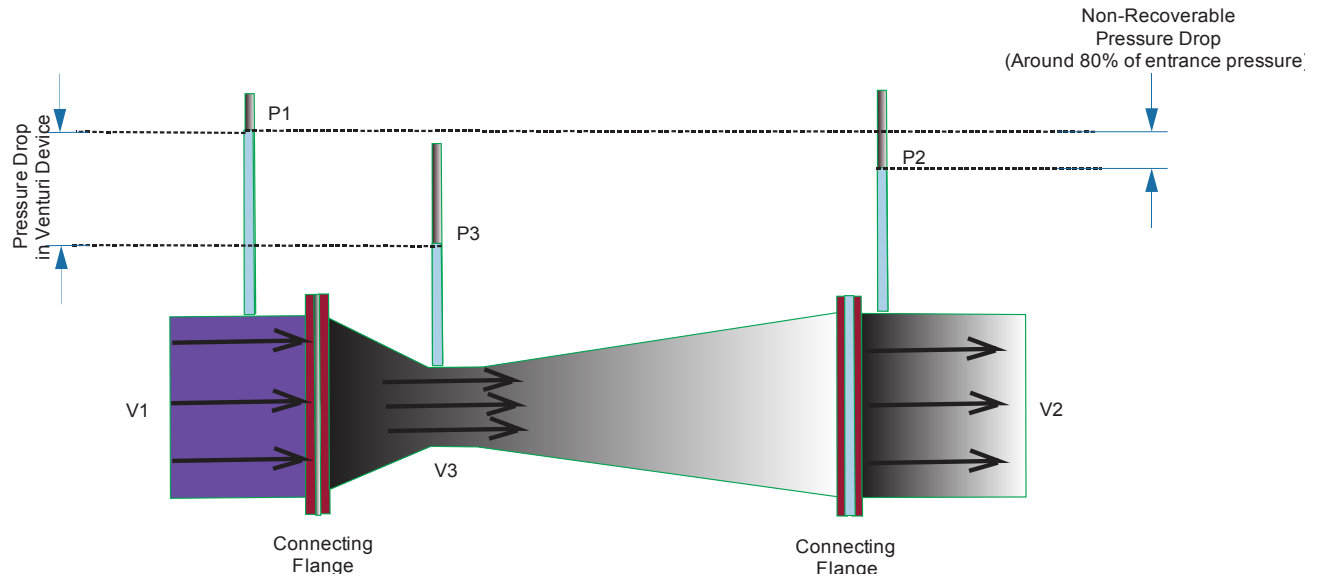


Figure 2.2. Venturi Tube flow metering technique (Adapted from [10])

2.1.1.3 The flow nozzle method

The flow-nozzle method includes constricted area with an elliptical contour part, which is ended to a cylindrical throat part. The pressure drop is measured between the first and the second cross sectional area, figure 2.3. The second pressure collection point is located at one-half of the pipe diameter. In comparison with orifice and Venturi techniques, this method provides intermediate pressure drop along the device. The flow-nozzles are used in gas and even slurry flow measurement in industry [2].

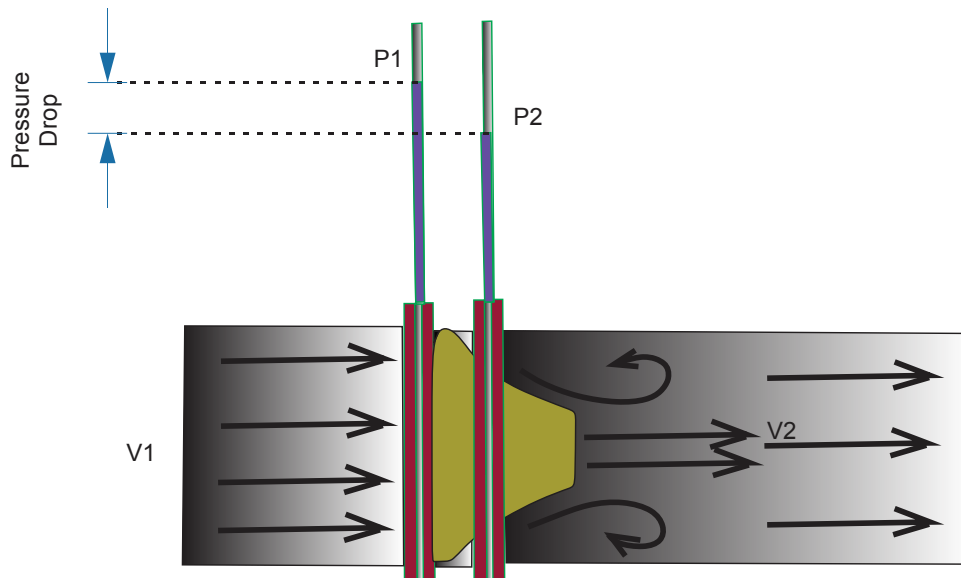


Figure 2.3. Flow nozzle method of flowmeter (Adapted from [2])

In the measuring method of flow nozzles, the phenomena known as choked flow conditions could occur [13]. Due to accelerating fluid along the nozzle, the velocity will increase thus a pressure (and density) drop will occur. The ultimate achievable velocity in the constricted zone is the Mach 1 which represents breaking or sonic point, which is called the choked condition. The choked flow situation plays a major role in the system control area. This phenomenon needs to be predicted and avoided.

2.1.1.4 Rotameter (variable area flow-meter)

This technique uses the balance of the lift force of the flow with gravity force to measure the flow. The rotameter consists of one conical tube (plastic or glass), which is oriented vertically and its larger end is at the top. The conical tube has a metering float, which can freely move up and down. The float rises by flow pressure with overcoming the gravity force until the ring shape area between the tube and float reaches the sufficient value for make dynamic

equilibrium between gravity force, differential pressure and buoyancy factor [2, 14]. The turndown ratio may reach 12:1 and accuracy is around 1%.

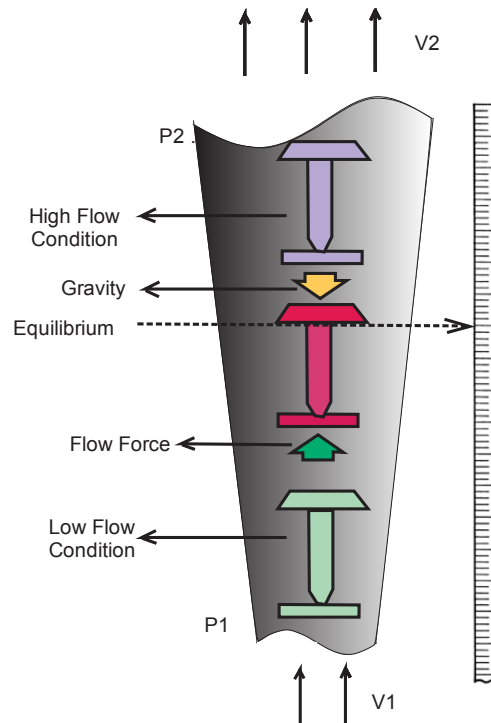


Figure 2.4. Rotameter Principle is based on dynamic equilibrium between gravity force and flow force (Adapted from [10])

2.1.2 Velocity flow-meters

The velocity flowmeter is popular technique, due to the direct measurement of velocity. Therefore, the characteristic is normally associated with flow rate. The primary assumption of velocity flow metering method is constant velocity profile. In laminar flow, the flow velocity varies from zero to maximum from wall to the center of the pipe, respectively. According to this property, the method is very sensitive to Reynolds number and piping geometry [15]. The Pitot

tube is most popular method that uses velocity as a measure of the flow. The operational principle will be discussed below in detail.

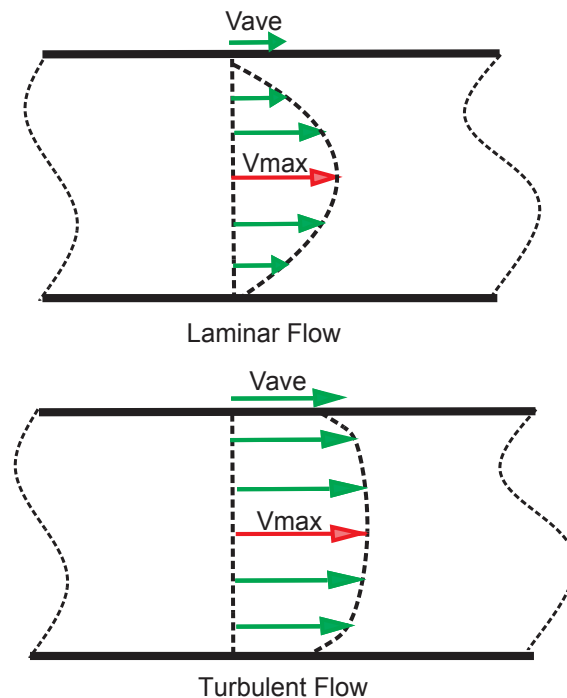


Figure 2.5. Velocity profile in Laminar and Turbulent Flow (Adapted from [11])

2.1.2.1 Pitot tubes

Traditionally in aviation technology, the Pitot tube has been widely used to determine the velocity of aircrafts. Also, it is used for local velocity measurement purposes inside a pipe. Hence, the measured value is not the average velocity but it is the local velocity. According figure 2.5, the average velocity value is very close to the local velocity value in turbulent flow. Thus this method is better applicable for turbulent flows. The measurement principle is based on transformation of the kinetic energy of flow into the potential energy of the column of fluid in the measurement tubes as illustrated in figure 2.6.

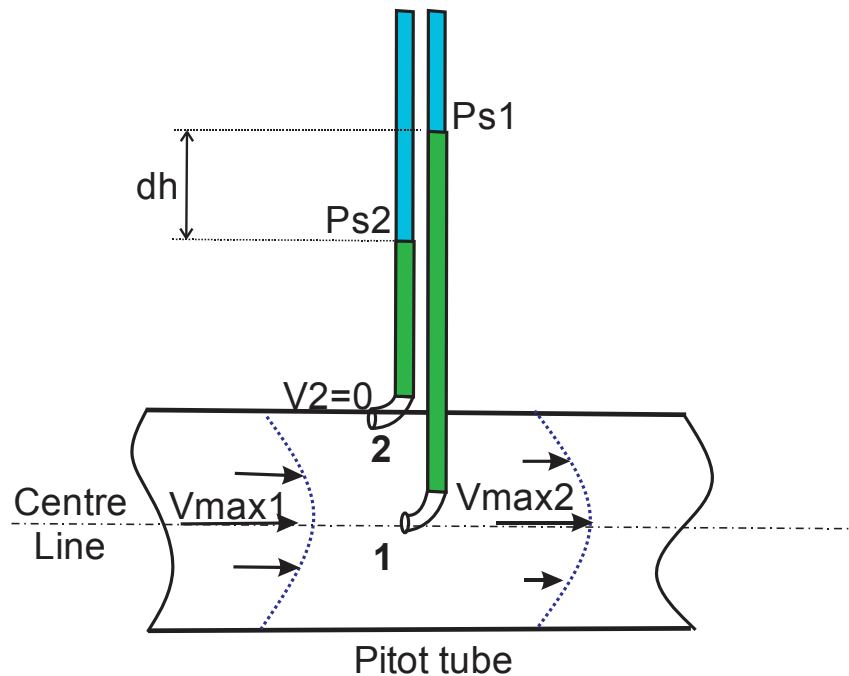


Figure 2.6. Velocity base measuring: Pitot tube (Adapted from [2])

The basic Pitot flow measurement device includes two tubes, which collect the pressure of the fluid from dedicated ports as shown in figure 2.6. One of the tubes collects fluid at the center of the pipe, where the velocity is maximum as shown in figure 2.5. The second tube collect fluid next to the wall, where the velocity is zero. The moving fluid will stagnate the fluid inside the tube at locations, which are known as the static pressure. The Bernoulli equation, can be written as:

$$P_s + \frac{\rho V^2}{2} + \rho gH = \text{constant in streamline} \quad (2.4)$$

Where, P_s is static pressure, and V and ρ are the flow velocity and moving fluid density, respectively. The g is the gravitational acceleration. The H is elevation height, which the associated term is representing pressure due to change in height level and known as hydrostatic pressure.

In regard to energy constancy along a streamline as illustrated in figure 2.6:

$$P_{s1} + \frac{\rho V_1^2}{2} + \rho g H_1 = P_{s2} + \frac{\rho V_2^2}{2} + \rho g H_2 \quad (2.5)$$

The indices “1 & 2” are the parameters related to port number “1 and 2” respectively, in figure 2.6. The hydrostatic pressure within the tube is negligible. On the other hand, since the velocity in wall is zero “ $V_2=0$ ”, the equation (2.5) will become:

$$P_{s1} + \frac{\rho V_1^2}{2} = P_{s2} \quad (2.6)$$

$$\text{Pressure differences} = \Delta P = P_{s2} - P_{s1} = \frac{\rho V_1^2}{2} = \text{Dynamic Pressure} \quad (2.7)$$

By solving for the velocity term:

$$V_1 = \sqrt{\frac{2(P_{s2} - P_{s1})}{\rho}} \quad (2.8)$$

The pressure differences ΔP will be in the form given by the equation (2.9). Flow could be measured by measuring the difference of height in the two tubes.

$$dh = \frac{\Delta P}{\rho_L g} \quad (2.9)$$

Where dh is the height difference of the two column in meters, ρ_L is the density of the liquid and g is the gravitational acceleration. Finally the velocity will found by:

$$V_1 = \sqrt{\frac{2(dh \times (\rho_L g))}{\rho}} \quad (2.10)$$

2.1.2.2 The Hot-wire method

Generally, the hotwire flow-metering method be classified in two types. The constant current and constant temperature techniques are two main classes that will be discussed below. Under constant current mode, the platinum wire serves as heating sources for the system. The Pt-wire maintains in a constant temperature by passing constant current through it. The constant current is provided by the energy source along with one series resistor as illustrated in figure 2.7. Further it is connected to a Wheatstone-bridge, which in one of the branches, the hot-wire " R_w " is serial with one resistor " R_L ". The series resistor of the energy source is selected large enough in compare with Wheatstone bridge resistance, in order to keep the current constant.

The mentioned constant temperature should be higher than the liquid temperature. The flow will cool the wire, thus the temperature variation makes resistivity changes in the hot-wire, which induces a voltage differences along the diagonal arm of Wheatstone bridge that is related to the flow velocity.

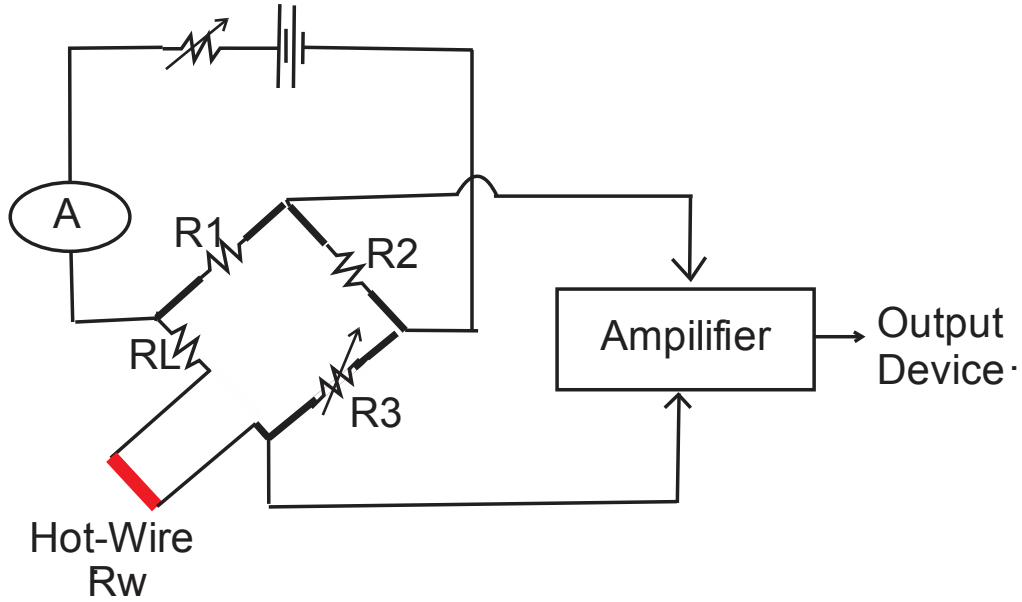


Figure 2.7. The schematics of the Hot-Wire sensing platform [16, 17]

Wheatstone bridge sensing scheme exhibits high sensitivity to small resistance variation. Therefore, the method is frequently used in piezoresistive sensing configurations such as strain gage and hot-wire techniques. According to the figure 2.8, V_{in} and V_{out} are the input and output voltage to the bridge respectively, R_1 , R_2 , R_3 are the resistances of the bridge. R_g is the only resistor in bridge that change resistance. The “ R_g ” resistor in this investigation will be considered the set that includes the hot-wire sensor. Based on the circuit configuration, the output voltage V_{out} is a function of V_{in} , R_1 , R_2 , R_3 and R_g . The governing equation is:

$$V_{out} = V_{in} \left[\frac{R_3}{R_3 + R_g} - \frac{R_2}{R_1 + R_2} \right] \quad (2.11)$$

One of the important concepts of Wheatstone bridge, which play a major role in sensing field is the bridge balancing condition. In balanced condition the output voltage is equal to zero, which will occur if: $(R_1/R_2) = (R_g/R_3)$. In figure 2.8, the variable resistor is reset in R_2 position,

which provides balance condition $V_{out} = 0$ by adding the capability of resistance adjustability to the bridge. Any small resistance change in the hot-wire branch, will generate a difference of potential as V_{out} , which is related to flow velocity. The generated voltage in system, will be fed to an amplifier for converting the signal to detectable range.

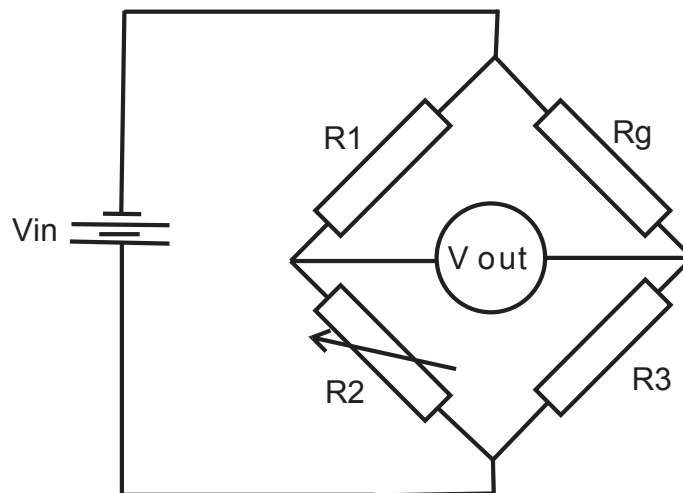


Figure 2.8. Wheatstone-Bridge principles

In the constant temperature technique, the device consists of two components: constant heating source and thermometer or thermocouple, which are installed in the upstream and downstream of the flow, respectively, as shown in figure 2.9. The thermometer/thermocouple measures the temperature of the fluid that passed by the heated wire and is locally warmed up. Thus, under steady state flow condition the temperature difference will be constant. The temperature difference between the two components “heater and thermocouple” will be related to the effective flow. Further, different known flow rates will be used for calibrating and validation of the system.

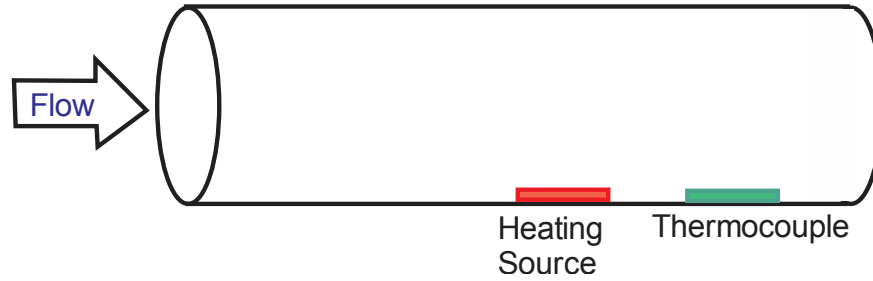


Figure 2.9. Constant temperature technique

Theoretically, the electrical power dissipation comes from (2.10). On the right side of the equation, the total heat loss in convective heat transfer is equal to the dissipated electrical power (2.12).

$$\text{Electrical power dissipation: } P_e = I^2 R_w \quad (2.10)$$

$$\text{Heat Loss in convection heat transfer: } Hl = h A_w (T_w - T_f) \quad (2.11)$$

$$I^2 R_w = h A_w (T_w - T_f) \quad (2.12)$$

Where h is the heat transfer coefficient, A_w is the area of the hot-wire (heating source) and R_w is the resistance of the hot-wire. The T_w & T_f are the temperature of the wire and fluid, respectively. According to the King's law [16, 17] the heat transfer coefficient is:

$$h = a + b V_f^c \quad (2.13)$$

One can show that by substituting the equation (2.13) in (2.12), the fluid velocity is the only function of current (2.14). The constant coefficients of "a, b & c" are defined during the calibration process.

$$a + b V_f^c = \frac{I^2 R_w}{A_w (T_w - T_f)} \quad (2.14)$$

The fluid thermal characteristic has a direct effect on the measuring accuracy of the system. In high thermally conductive fluids, lower fluid velocity yields accurate measurements and conversely [7].

2.1.2.3 Turbine flow-meter

Different types of turbine designs are available for flow measuring systems and all follow a basic principle. The necessary energy for rotation of the turbine is collected from the flow. A simplified schematic of the systems is illustrated in figure 2.10. This type of flow measurement system includes four main parts: free rotating rotor, permanent magnet, flux pick up coil, and a detection device.

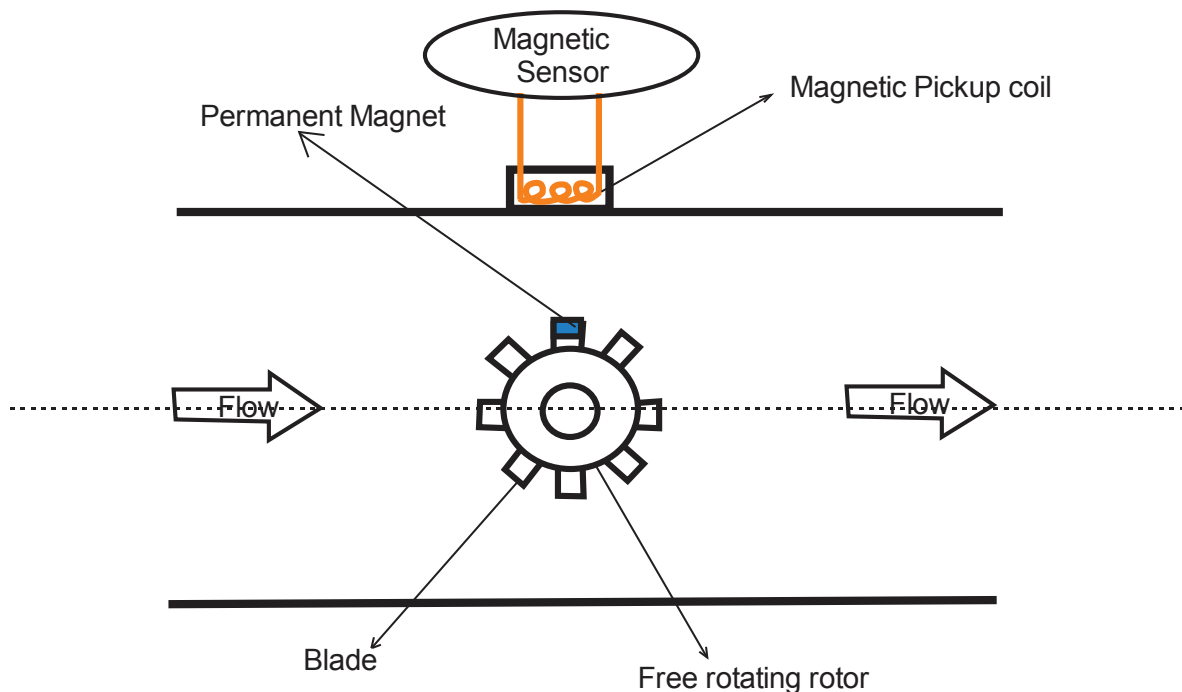


Figure 2.10. Schematic of Turbine flow meter principle (Adapted from [18])

The freely rotating rotor is usually fixed to the wall of the pipe which flow rate is to be measured. A permanent magnet is installed and balanced on one blade of the rotor. The polarization axes of the permanent magnet is perpendicular to the rotation axis of the rotor. The rotation of the permanent magnet will produce a rotational magnetic field. This field will be picked-up by the magnetic pick-up sensor at every turn. This phenomenon will generate a pulse voltage, which the frequency of voltage pulses will be sensed by magnetic sensor.

The frequency of pulses at the magnetic sensor serves as a measuring indicator of the flow. Calibration is usually performed on such systems. The volume of the flow is given by equation 2.15. In this equation, the Q , N_f and C_{flow} are the flow-rate volume, total pulse numbers and the flow coefficient, respectively.

$$Q = \frac{N_f}{C_{flow}} \quad (2.15)$$

As it is shown in equation 2.15, the flow and the number of pulses are in a linear relationship. One of the major drawbacks of turbine technique is the bearing friction, which may affect the linear output of the method. The turndown ratio and accuracy for this technique usually are 100:1 and $\pm 0.1\%$, respectively [4].

2.1.2.4 Vortex flow metering

The vortex flow-metering includes a blunt obstacle, which is located in the flow path of the pipe as illustrated in figure 2.11. The obstacle is called bluff body. Flow oscillations occur after the bluff body and generates the vortices on both sides of the blunt obstacle [5]. The generated vortex series was formulated by “Von Karman” and called “Karman Vortex Street”. The Karman vortex includes a trail of swirls that are frequently propagated from each side of an obstacle by

180° phase differences as shown in figure 2.12. The wave of the flow is well evoked by a flag flapping in the wind.

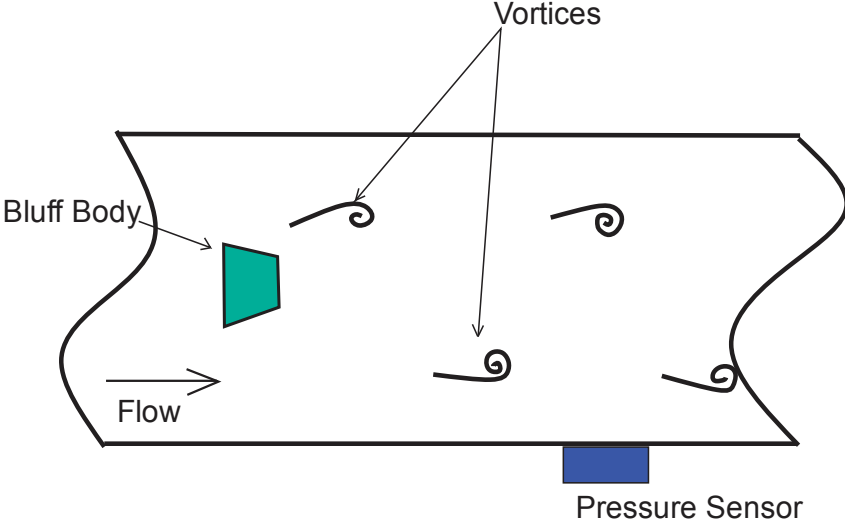


Figure 2.11. Vortex Flowmeter principle

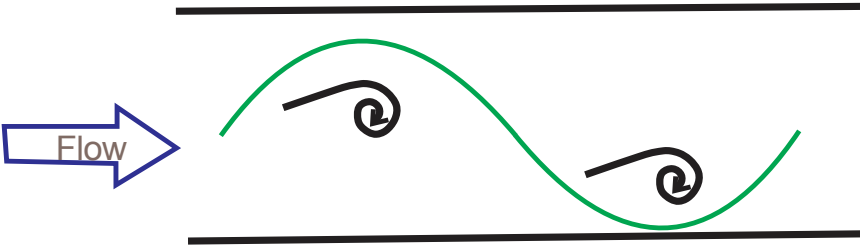


Figure 2.12. The generated trail of swirls which propagated by 180° phase differences from each side of the bluff body, that is perceived as sinus wave (Adapted from [5]).

In the downstream of the pipe, one sensitive pressure sensor is located as illustrated in figure 2.11. The pressure sensor records every pressure variations that occur with every passing vortex wave. After calibration of the system which is performed by measuring velocities, based on the Karman equation in (2.16), the number of vortices in a defined period of time is directly proportional to the velocity of the fluid flow and the width of the bluff body.

$$f = \left(S_t \frac{V_{ave}}{d} \right) \quad (2.16)$$

In equation (2.16), the S_t is a constant known as Strouhal number. The parameters f , d , and V_{ave} are the frequency of the shedding, the width of the bluff body and the average velocity of the fluid. By using the below equation (2.17) by a known vortex frequency, the flow rate will be determined. In equation (2.17), Q and A are the volumetric flow rate and the cross-sectional area of the flow-metering body, respectively.

$$Q = A V_{ave} = \frac{f d A}{S_t} \quad (2.17)$$

2.1.2.5 Electromagnetic flowmeter

The fundamentals of the measuring principle are related to Faraday's law of electromagnetic induction. This law indicates that a voltage is induced by moving a conductor through a magnetic field [19]. The liquid flow acts as a conductor in an electromagnetic flow-meter device. The appropriate liquid conductivity is required for this method.

The conductivity of water is in a direct correlation with the concentration of a salt dissolved in the water or the Total Dissolved Solids (TDS). Dissolved salts in the water are decomposed to positively and negatively charge ions which conduct electricity (ion conduction and not electron based conduction). The unit for conductivity is micro Siemens per centimeter " $\mu\text{S}/\text{cm}$ " or deci-Siemens per meter " dS/m ". Generally, the electromagnetic flowmeters are suitable for fluids with electrical conductivity above $10 \mu\text{S}/\text{cm}$. Thus, the flow measurement of the distilled water or other non-conductive fluid is not suitable with this method.

According to Faraday's Law, when a conductive fluid passes perpendicular to a magnetic field B an induced voltage E will be generated as illustrated in figure 2.13. Here E is proportional to the density of magnetic field B , the length of the conductor L and the flow velocity v , as expressed in the equation (2.18). From a practical point of view, the induced voltage will be collected by two metallic electrodes, which are located inside the pipe opposite of each other as illustrated in figure 2.13. The voltage will be sent to an electronic circuit for post processing of the signal.

$$\mathbf{E} = \mathbf{BLv} \quad (2.18)$$

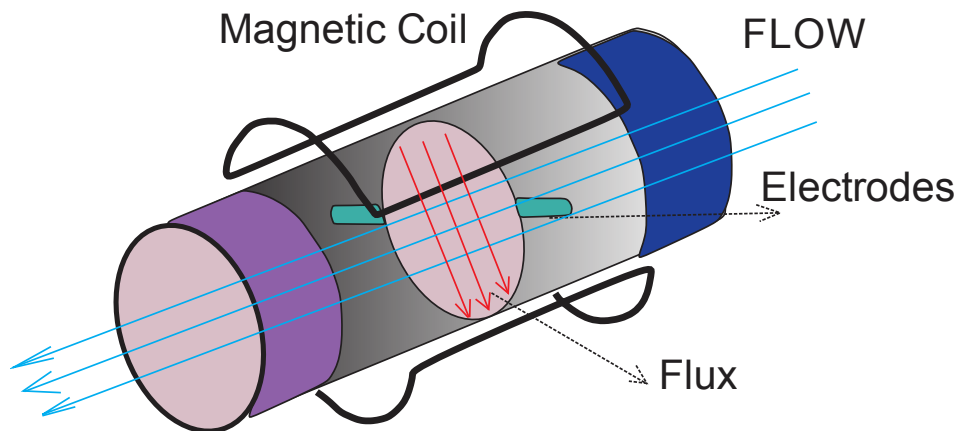


Figure 2.13. Electro-magnetic Flowmeter (Adapted from [8])

Based on figure 2.13, the volumetric flow rate for a pipe with diameter d is given by the equation (2.19) where v represents an average velocity. Further, by substituting the value of velocity from equation (2.18) in equation (2.19), another formulation will be found (2.20). In this final relationship one constant k is required, which is found from the calibration phase of the device as in equation (2.21).

$$Q = \frac{\pi d^2}{4} \times v \quad (2.19)$$

$$Q = \frac{\pi d^2}{4} \times \frac{E}{BL} \quad (2.20)$$

$$Q = k \times E \quad (2.21)$$

The electromagnetic method is suitable to measure wastewater, slurries and corrosive liquids. The monitoring accuracy when flow is in vertical or horizontal directions is the same. High power consumption and conductive liquid requirements represent the drawback of the electromagnetic flow measurement [8].

2.1.2.6 Ultrasonic doppler flowmeter

This method is based on Christian Johann Doppler principle [20]. The frequency of reflected signal from a fluid flow is modified by the velocity and direction of the fluid flow. This method requires of one pair of transducers which are installed on the outer surface of the pipe, one on the upstream and the other on the downstream as illustrated in figure 2.14. Each of the transducers are used as transmitter and receiver of ultrasonic signals. When transmitting the ultrasonic signal against the flow direction in the upstream direction, more emitting time is needed, t_u . In comparison with upstream side, less propagation time is required for transmitting the signal along the downstream side in the flow direction, t_d . The time differences between t_u and t_d are proportional with the flow speed and is used as a scale point for measuring the velocity and the flow rate.

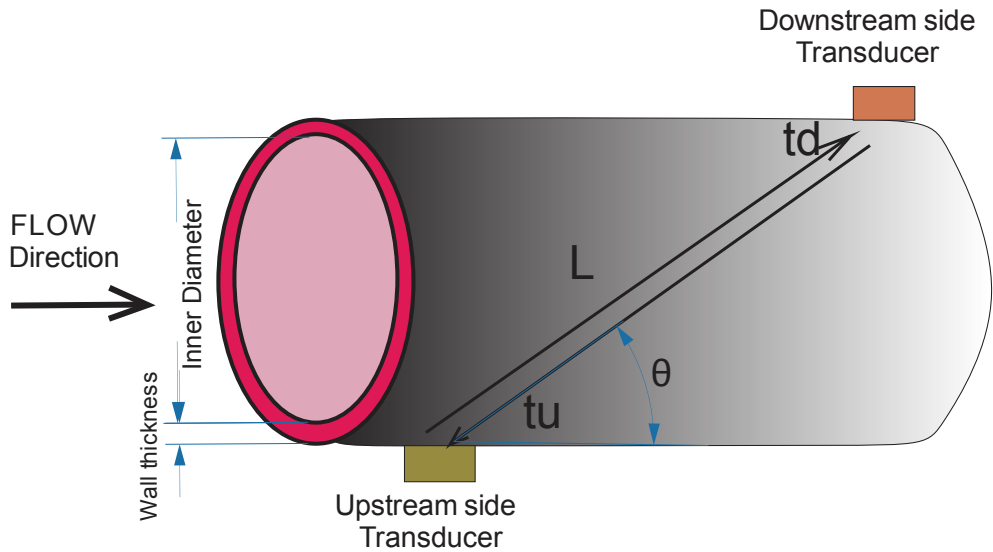


Figure 2.14. Ultrasonic Doppler Flowmeter (Adapted from [21])

According to figure 2.14, the formulations are:

$$\begin{cases} t_d = \frac{L}{c + v \cos\theta} \\ t_u = \frac{L}{c - v \cos\theta} \end{cases} \quad (2.22)$$

Where c is the speed of sound in the fluid, L is the distance between two transducers, θ is the angle between flow direction and the line formed by the transducers, and v is the velocity of the flow. The Δt after some simplification is given by:

$$\Delta t = t_u - t_d = \frac{\frac{2vx}{c^2}}{1 - \left(\frac{v}{c}\right)^2 \cos^2\theta} \quad (2.23)$$

In equation (2.23), the parameter x is $L \times \cos \theta$. The flow velocity v is negligible in compare with sound speed c , thus “ $(v/c)^2 \approx 0$ ”. Finally, the formulation for the velocity stems from the equation (2.24).

$$v = \frac{c^2 \Delta t}{2x} \quad (2.24)$$

2.1.3 Positive displacement flowmeter

Basically, this method consists of a chamber which restricts the flow. Generally, two rotors are precisely fitted inside the chamber. The known and constant volume (Q_0) of flow are passing in every full cycle through the chamber. Thus by counting the number of cycles and multiply into the known volume Q_0 , the flow rate is achievable. The positive displacement flowmeter measures directly the volumetric flow rate. The measuring accuracy is around 0.1% [6].

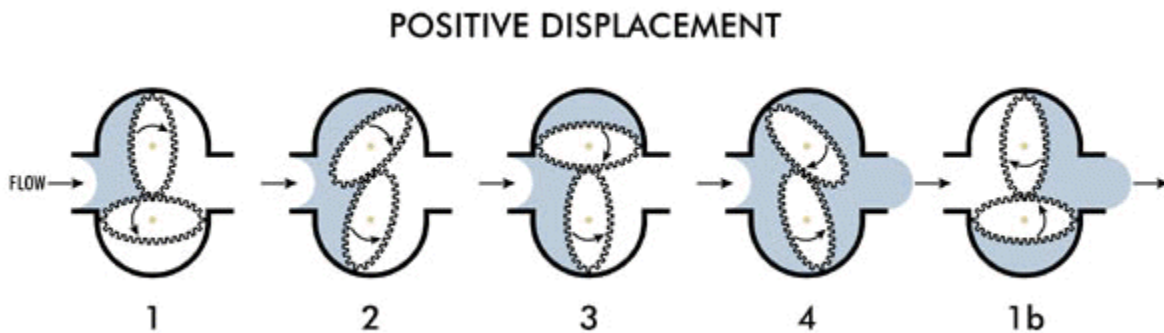


Figure 2.15. One cycle of PD-flowmeter (Adapted from [22])

2.1.4 Coriolis flowmeter

Generally, the physical quantities such as density, pressure or viscosity of liquids do not have any effect in the Coriolis based measurements. However, the ability to work effectively with

slurries and gas makes this principle a universal measuring method. A travelling mass through a rotating system will experience one force perpendicular to the direction of motion, which is called Coriolis Effect, due to Coriolis acceleration.

As illustrated in figure 2.16, the fluid is split to two U-shaped pipe. The velocity transducer or electric coils provide oscillating excitation force. Then the U-shaped pipes will oscillate synchronized. The generated vibration is measured by a magnetic sensors. In no-flow condition the curved pipes are vibrating in pure sin-wave shape. When flow is present, the Coriolis acceleration induces a rotation or a twist to the system as illustrated in figure 2.17. The Coriolis force modifies the harmonic vibrating of two U-shaped tubes. Their new oscillating conditions are shown in figure 2.18. As illustrated, the sin-wave of the entrance-side and exit-side exhibit a ΔT phase difference which is proportional with mass flow rate [23, 24].

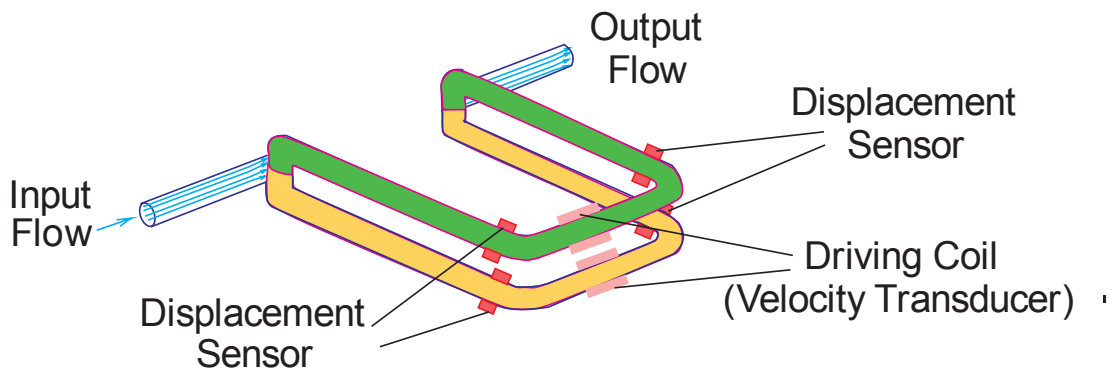


Figure 2.16. Coriolis Flowmeter, the flow split into two U-shaped tube; the displacement sensors are located in the corners and the driving coils is in the center (Adapted from [23, 24]).

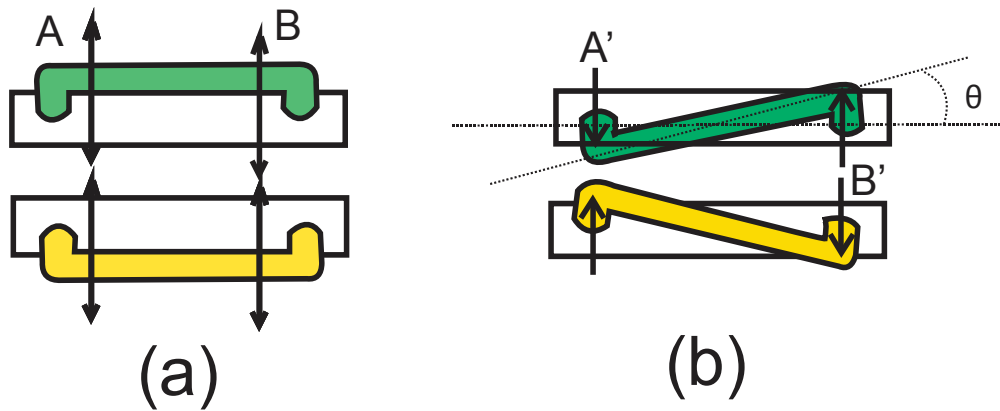


Figure 2.17. Front view of the system; a) Non-flow condition; b) Flow condition (Adapted from [25])

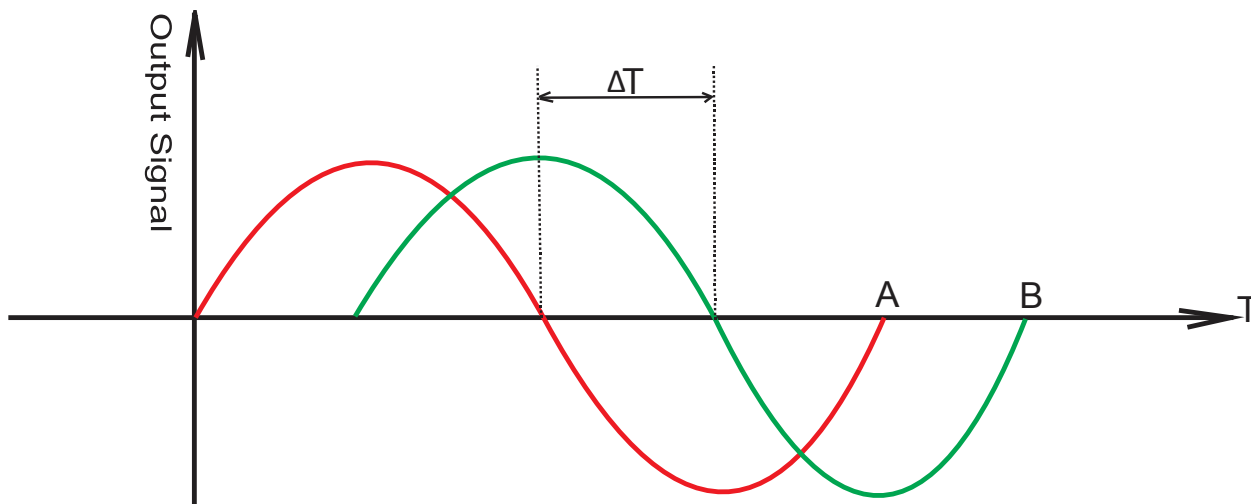


Figure 2.18. Phase differences ΔT between no-flow and flow conditions.

A: Entrance side output, B: Exit-side output. (Adapted from [24])

2.1.4.1 Operation principle

As it is shown in figure 2.19, the effect of the Coriolis force on the section of the fluid " δm " is given by:

$$\delta F_c = \delta m \cdot a_c = \delta m \cdot 2\Omega \times V \quad (2.25)$$

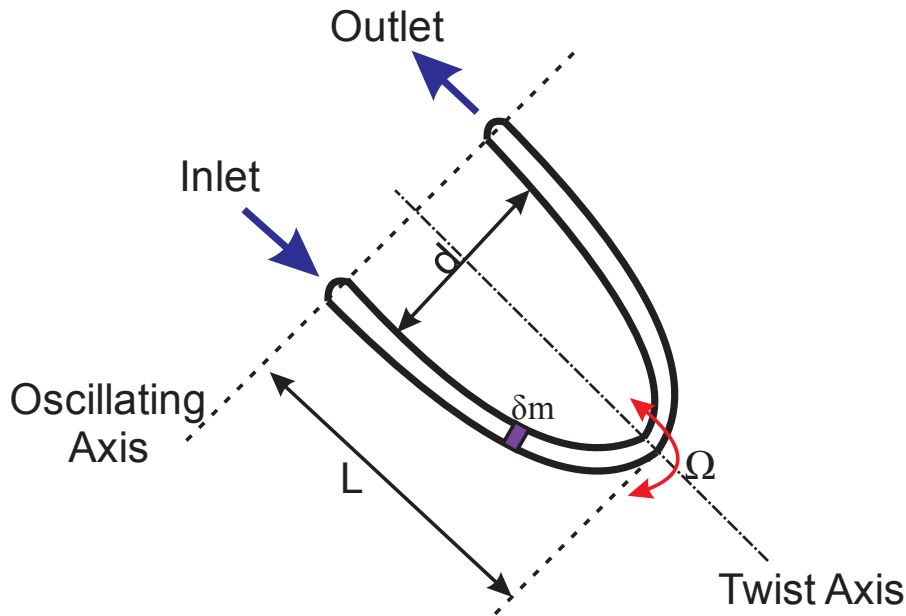


Figure 2.19. Coriolis Effect of the U-Shaped pipe

The curved pipe assumed to have a perfect U-shape and the cross sectional area of pipe is assumed to be A . According the figure 2.19, the geometric parameters l and d are the length and width of the loop of the U-shaped pipe, respectively. The twist induced moment T_c by the Coriolis effect is:

$$T_c = F_c \cdot d = m \cdot a_c \cdot d = \rho A l \cdot 2\Omega V \cdot d \quad (2.26)$$

The K factor will be added to the formulation as a calibration coefficient. By replacing the mass flow rate formulation $Q_m = \rho AV$ in equation (2.26):

$$T_c = 2K\Omega\rho AVdl = 2K\Omega Q_m dl \quad (2.27)$$

The governing equation for this type of rotational motion is of the form:

$$I_u \frac{d^2\theta}{dt^2} + C_u \frac{d\theta}{dt} + K_u \theta = T_c \quad (2.28)$$

Where: I_u : Inertia of the U-shaped pipe filled with fluid, C_u : Damping coefficient, K_u : The stiffness of the elastic system, θ : Twist angle and t is the time.

The driving coil excites the U-shaped pipe at a frequency ω , thus the real angular velocity formulation is a function of ω :

$$\Omega = \Omega_0 \cos \omega t \quad (2.29)$$

The form of equation (2.28), by assuming the damping coefficient as zero is:

$$I_u \frac{d^2\theta}{dt^2} + K_u \theta = T_c \quad (2.30)$$

By substituting the T_c from (2.27) the formulation will be:

$$I_u \frac{d^2\theta}{dt^2} + K_u \theta = 2K\Omega Q_m dl \quad (2.31)$$

The final form of the equation (2.31) by using the equation (2.29) can be written:

$$I_u \frac{d^2\theta}{dt^2} + K_u \theta = 2KQ_m dl \cdot \Omega_0 \cos \omega t \quad (2.32)$$

The steady state solution (particular answer) of the equation (2.32) will be:

$$\theta = \theta_0 \cos \omega t = \frac{2KQ_m dl \cdot \Omega_0}{K_u - I_u \omega^2} \cos \omega t \quad (2.33)$$

The θ_0 value based on the solution (2.33) is:

$$\theta_0 = \frac{2KQ_m dl \cdot \Omega_0}{K_u - I_u \omega^2} \quad (2.34)$$

According to figure 2.19 and figure 2.20, the velocity of two corners of the U-shape pipe is “ $\Omega \times l$ ”. The maximum displacement between the two corners, figure 2.20 is: “ $\theta \times d$ ”. Thus the time differences between corners are:

$$\Delta T = \frac{x}{V} = \frac{\theta d}{\Omega l} = \frac{(\theta_0 \cos \omega t) d}{(\Omega_0 \cos \omega t) l} = \frac{\theta_0 d}{\Omega_0 l} = \frac{\left(\frac{2KQ_m dl \cdot \Omega_0}{K_u - I_u \omega^2}\right) d}{\Omega_0 l} = \frac{2KQ_m d^2}{K_u - I_u \omega^2} \quad (2.34)$$

By solving the equation 2.34, the mass flow can be calculated:

$$Q_m = \frac{K_u - I_u \omega^2}{2Kd^2} \Delta T \quad (2.35)$$

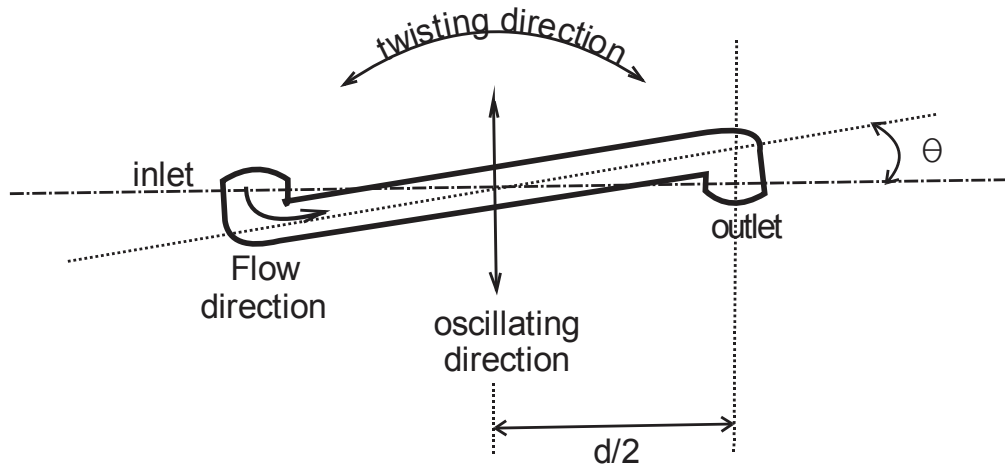


Figure 2.20. Front view of the U-shaped pipe.

2.2 The proposed principle of flow measurement

In the third chapter, the finite element analysis (FEA) reveals the significant dynamic pressure differences from zero to maximum in wall and center of the pipe, respectively. The

dynamic pressure variation in the cross section of the pipe stems from velocity variation across the pipe. As it is illustrated in figure 2.5 (section 2.1.2), the velocity profile theoretically has a perfect parabolic shape when laminar flow occurs and semi-parabolic in turbulent flow.

Theoretically, the idea is to measure three different points within half cross section area of the pipe. Small sensing elements should be used to avoid interference of the measurement system with the flow. Further, the velocity profile is found by matching a parabolic curve passing through these control points. Furthermore two boundary conditions are applied in the formulation. First, the velocity value near the wall is zero and the second one is the maximum velocity value at the center of the pipe.

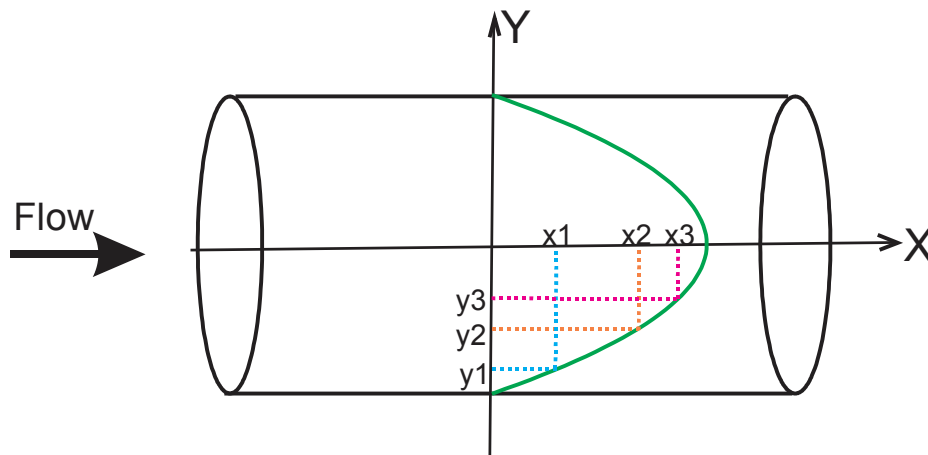


Figure 2.21. Parabolic velocity profile and the control points coordinate positioning inside the pipe.

According to figure 2.21, the x-axis is selected along the flow direction in the pipe while the y-axis is oriented along with cross-section of the pipe. Thus, for the configuration showed in figure 2.21, the parabolic velocity profile is given by:

$$x = a y^2 + by + c \quad (2.35)$$

$$\text{B. C.} \begin{cases} x_{\max y=0} = c = V_{\max} & (V_{\max} \text{ is unknown}) \\ \text{In } y_{1,2} = \pm (d/2) \rightarrow x = 0 \end{cases} \quad (2.36)$$

The three coordinates of the measurement points are: (x_1, y_1) , (x_2, y_2) and (x_3, y_3) . Finally, the three equations with three unknowns could be written:

$$\begin{cases} x_1 = a y_1^2 + b y_1 + c \\ x_2 = a y_2^2 + b y_2 + c \\ x_3 = a y_3^2 + b y_3 + c \end{cases} \quad (2.37)$$

The only unknowns in the equation (2.35) are a, b, c coefficients. The coefficients could be found by solving the equation (2.37).

$$\begin{bmatrix} x_1 \\ x_2 \\ x_3 \end{bmatrix} = \begin{bmatrix} y_1^2 & y_1 & 1 \\ y_2^2 & y_2 & 1 \\ y_3^2 & y_3 & 1 \end{bmatrix} \begin{bmatrix} a \\ b \\ c \end{bmatrix} \rightarrow \begin{bmatrix} a \\ b \\ c \end{bmatrix} = \begin{bmatrix} y_1^2 & y_1 & 1 \\ y_2^2 & y_2 & 1 \\ y_3^2 & y_3 & 1 \end{bmatrix}^{-1} \begin{bmatrix} x_1 \\ x_2 \\ x_3 \end{bmatrix} \quad (2.38)$$

Consequently, the parabolic velocity profile is determined by the solutions of the set of three equations and the two boundary conditions. The distance of detection of the sensors from entrance of the pipe has a direct influence on velocity profile, which will be discussed in detail in the third chapter.

Chapter 3 Modeling and Simulation of the Measurement Method

In this chapter the sensing issues will be discussed. The remarkable advantages of piezoresistive based sensing element hints towards using of this classic principle in flow measurement [1]. The small cantilever beam as an elastically deformable surface is designed and positioned within the fluid flow. The velocity profile will be predicted by signals coming from the piezoresistive effect of the strain gauge built or installed on the bending cantilever beam.

Since the nature of phenomena is fluid-structure coupling, the analytical formulation is carried out in both fluid and structural fields. The finite element analysis is a practical method which enable numerical solving of complex problems. The numerical solution phase is performed using ANSYS workbench [26]. Finally, the results of the modeling and simulation are presented.

3.1 Introduction

When building a measurement system or as a matter of fact, any system, one has to build first a model of the targeted system. The considered model may be reduced, which is usually the case of complex systems. The reduced model may not exhibit the suitable accuracy to be used for the conversion of the measurement but it may be extremely useful into establishing the most influential parameters in the process that may mostly influence the measurement. With this information, one could focus the design into addressing the most influential factors and ensure a sensitive and robust measurement scheme.

A more detailed model could be conceived in the second step of the design iteration as more information and more parameters are known at this time. The model could be more accurate and equally, more complex at this level. The construction of the model may require for solving numerical solutions to the complex formulation that may not have analytical solution.

Starting from the design consideration of a low cost system capable to measure with good accuracy fluid flow through small diameter pipes while accounting for temperature variation of the agent points towards a classic approach. Thus, piezoresistive based measurement is associated with the low cost and simplicity but it is quite sensitive to temperature variations. The “small” attribute will associate with a measurement device that would be small too.

Thus, a small surface which could elastically deform for the loads associated with the dynamic pressure of fluids in small diameter pipes is positioned versus the fluid flow such that it would minimally interfere with the continuity of the fluid. The beam will bend proportional to the flow and it would restore when there is no flow. Further, it is stated that if in a laminar flow

the velocity profile is known, the flow could be estimated through calculation. The deflection of the beam could be corrected by a thermal factor that will be acting as a correction coefficient. To enhance the accuracy of the measurement, more than one beam is considered for the measurement system.

As it is mentioned in section 2.2, the flow profile for laminar flow in a pipe is a parabola equation (2.34), which could be identified if three points of the parabola are known. Further the parabola coefficients will be found based on the equation (2.37). Enhanced accuracy could be obtained by measuring the dynamic pressure at more than three points. Hence, by using two boundary conditions which are explained in equation (2.35) and applying symmetry across the pipe cross section more accurate result are achievable.

Once the parabola profile is evaluated the flow through the pipe is determined. As the flow needs to be controlled, the sensing element should be located somehow close to the valve. As the valve is a variable restrictor, the flow through the valve is usually turbulent. At a certain distance from the valve, flow could regain the laminar state. A quite reasonable question is: at what distance from the valve the flow regains its linearity such that a parabolic profile would define the flow profile? This is the main reason for which in the following part, the investigation of the flow is carried out. The below investigation will analyze the flow profile in a generic circular pipe at a given distance from a restrictor.

3.2 The Entrance Region

One of the important parameter that plays an important role in sensing accuracy is the location of sensor with respect to the valve. Previously it was stated that the sensing elements would be positioned close to the valve such that the valve control could be evaluated. Further, assume liquid entering to pipe at a uniform velocity. The fluid velocity varies within the pipe cross section. At the boundary the velocity of the fluid is equal to the speed of the solid wall that it means zero, which is called the no-slip condition. The velocity varies from zero to maximum from the wall of the pipe to its centerline, respectively. As the velocity of the fluid in contact with the pipe is zero and the flow occurs by keeping constant of mass flow-rate in pipe, the fluid velocity at the center streamline has to increase. Hence, a velocity gradient will appear along the pipe.

Viscous shear force stems from fluid viscosity and creates a region that is known as velocity boundary layer. The flow in pipe divides to two regions by this assumptive boundary surface, the first zone is “Velocity boundary layer region”, where the velocity variations and viscous influence are significant. The second one is called “core – flow - region”, where the velocity remain constant in radial direction and the frictional effects are negligible, figure 3.1 A.

The boundary layer thickness continuously increases along the flow direction until reaches the pipe center and fills in the whole pipe. The region from the inlet of the pipe to the point that the boundary layer merges to center line is known as hydro-dynamically entrance region “ L_H ”, figure 3.1 A. Flow in L_H region called hydro-dynamically developing flow, since velocity profile is developing in this area attempting to the laminar condition. The region beyond the L_H

is known as hydro-dynamically fully developed region, since the velocity profile is fully developed and unchanged in the rest of the duct as illustrated in, figure 3.1 B.

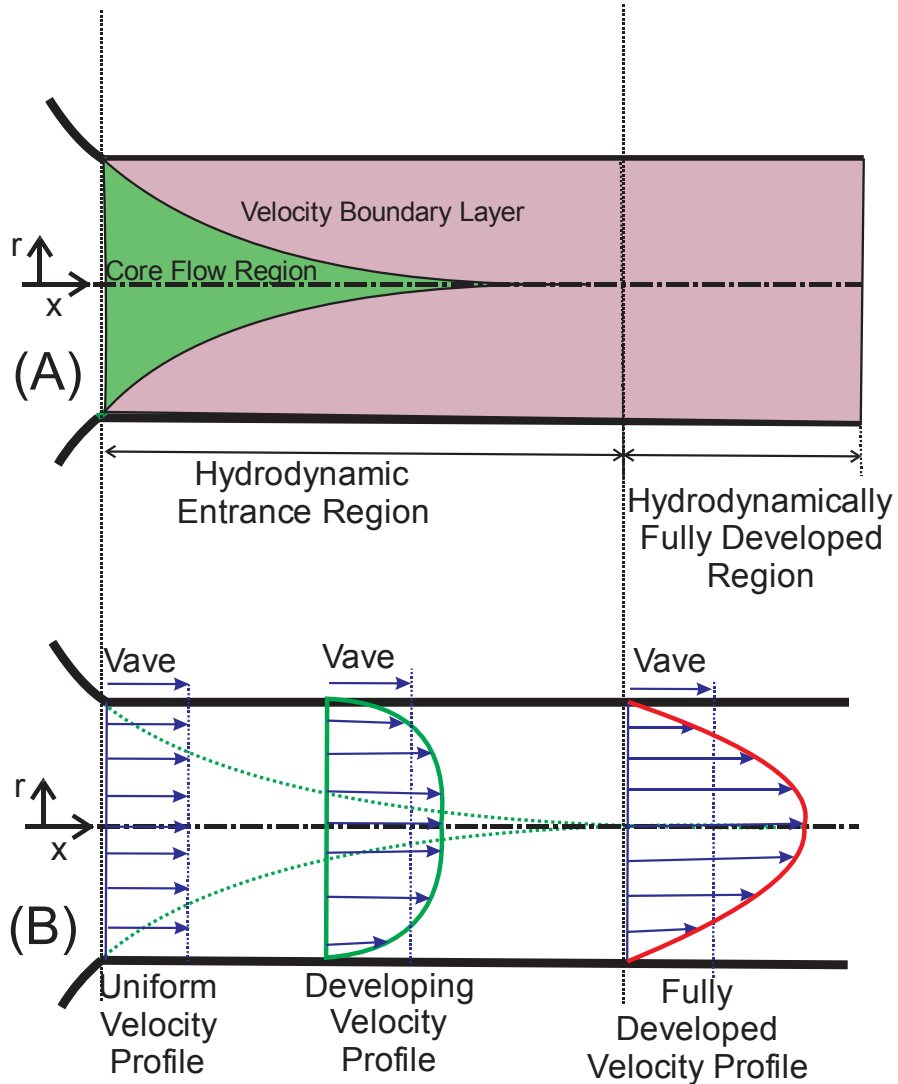


Figure 3.1. The velocity boundary layer development in a pipe (Adapted from [11]).

The velocity profile in fully developed area is parabolic as in the laminar flow. In turbulent flow, due to the Eddy motion¹ [27] and more intensive mixing in radial direction, the velocity profile is a little fluttered but still parabolic [28]. In addition, wall shear stress is gradually

¹ The swirling and current reversing condition appears in turbulent flow, which it is known as Eddy motion.

decreasing from its highest value at the valve which is the pipe entrance to its minimum value in fully developed region as illustrated in figure 3.2. Also, the entry length is defined as a distance from the pipe inlet to where boundary shear stress reaches a value which error is not more than 2 percent of the value of the fully developed value.

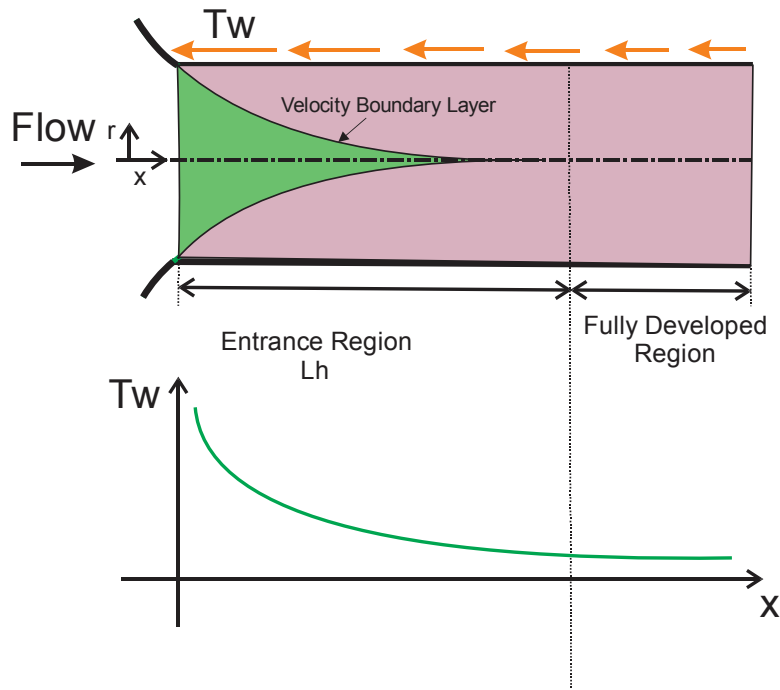


Figure 3.2. The wall shear stress variation in the flow direction (Adapted from [11])

One of important parameters that demonstrates the flow transition from laminar to turbulent is Reynolds number [29]. The Reynolds number is a dimensionless quantity (3.1), which is dependent on pipe diameter “D”, mean velocity “V”, dynamic viscosity “μ” and density “ρ” of the fluid. Osborn Reynolds stated that the laminar flow in pipe changes to turbulent if “Re” number reaches its critical value around 2000. Hydrodynamic entry length in laminar flow [30, 31] is given by the equation (3.2).

$$\text{Re} = \frac{\rho V D}{\mu} \quad (3.1)$$

$$L_H = 0.05 \text{ Re } D \quad (3.2)$$

Based on this formulation, the entry length to achieve a laminar flow in a pipe, varies from 1D to 115D, as Re changes from 20 to 2300. The hydro-dynamic entry length in turbulent flow is given by the below equation [30, 32].

$$L_{H_{\text{Turbulent}}} = 1.359 D \text{ Re}^{0.25} \quad (3.3)$$

In this regard for the turbulent Reynolds number of 2300, the calculated value of the entry length will be 9.4D, which is much shorter than the hydrodynamic length (115D) in laminar flow. In some of fluid engineering sources, it is mentioned that: “In the majority of flows in the pipe of feasible engineering applications, the entrance effect after 10D is negligible” [11]. On the other hand, much longer length such as “40D” and “150D” are recommended by other authors [33, 34]. The objective of this analysis is finding an acceptable entry length with reasonable error percentage based on appropriate Reynolds categories of flow in the pipe.

Hence these conditions of flow are simulated for different Reynolds numbers. The numerical modeling phase is carried out using the commercial general purpose application ANSYS. The complete modeling details will be presented in section 3.4. The velocity profile deviation is investigated for the range of 3,800 to 80,000 Reynolds, which occurs when the velocity in a 1 ½ inch pipe varies from 10 cm/s to 210 cm/s.

The accurate analysis can be started from investigating the flow after the valve at the entrance of the pipe. In regard to different geometry of the valves and complexity of the output

flow from the valves, simplified entrance condition will be used. On another hand, due to the axisymmetric nature of the geometry, the 2D model will be studied as a first step. The significant reduction in computation time occurs using 2D model instead of 3D one.

From an experimental point of view, it should be mentioned that due to laboratory equipment restrictions, air will be used instead of water. Thus, the simulation will be easily validated by using a fan in the vacuum orientation for providing more uniform flow at the entrance. Figure 3.5 demonstrates the uniform import velocity at the entrance of the pipe as the initial condition of the flow.

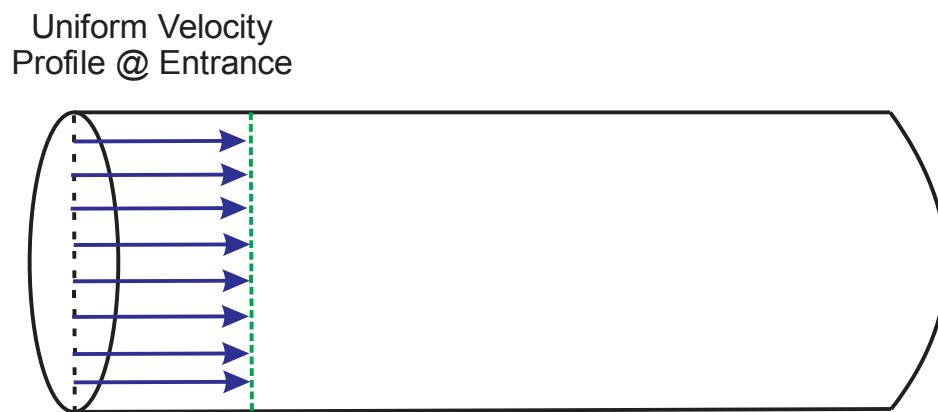


Figure 3.3. Uniform velocity profile as initial condition at the entrance of the pipe

The maximum range of Reynolds number is approximately two times higher than the catalog values provided by the valve manufacturer. The velocity profile represents one of the best measures to evaluate the flow. The fluid flow is then measurable by integrating of velocity profile in the cross section of the pipe.

First, the velocity profile in ten different cross-sections in a 1 ½ inch pipe is investigated. The velocity profile is analyzed in 3 points within the selected cross section. The reference is the

value of flow at the selected locations at the point of fully developed laminar flow. The differences of velocity at the three locations is analyzed in nine more sections and the root mean square error “RMSE” of the difference between the value recorded within the fully developed region and the values at same points in the selected cross sections will be evaluated.

As it is illustrated in figure 3.4, three different velocity values in every individual cross-section as well as one constant velocity in wall which is equal to zero, are used for plot parabolic velocity profile. Where the P1, P2, P3 are the control points with d1, d2 and d3 distances from wall of the pipe. In this case study, the diameter of the pipe is 38.1 mm (1 ½ inch) and the distance of the P1, P2, P3 from wall are 5, 10 and 15 mm, respectively.

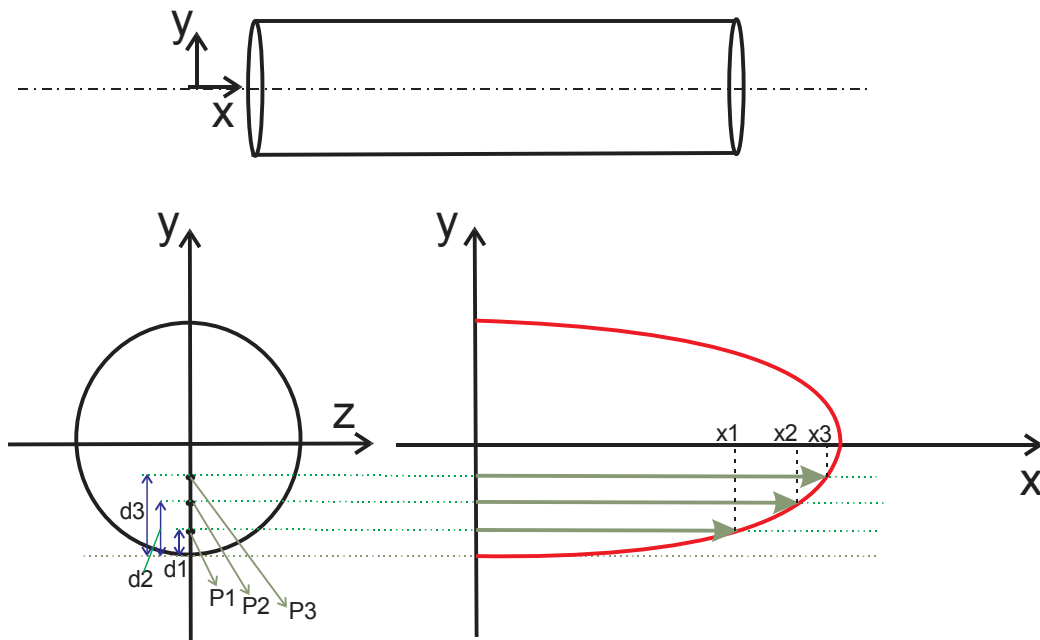


Figure 3.4. Three different velocity values with zero velocity in wall make half-parabolic velocity profile.

As it was mentioned, the recommended entry length in feasible engineering applications is 10D. Thus for the investigated Re range in this study “3800 – 80000”, the maximum predictable error may occur at 80000 Re. The computed entry length for this Re number according to the (3.3), is 22.8D. Hence the eight investigated cross-sections are selected between 10D and 22.8D, figure 3.5.

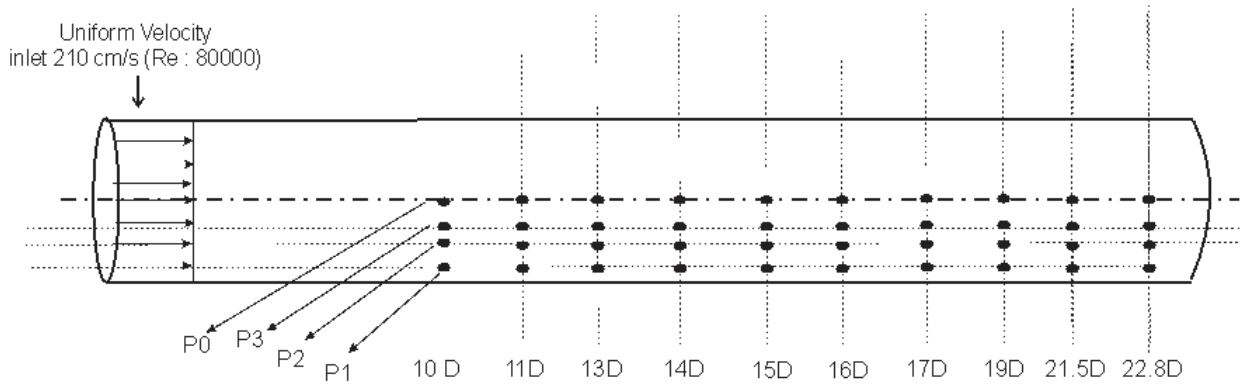


Figure 3.5. The investigated cross sections between 10D and 22.8D at Reynolds number equal to 80000

The velocity profile in 22.8D is named as reference profile. The plotted velocity profiles at different cross-sections will be compared with reference profile. As it is demonstrated in figure 3.6, RMSE error of velocity profile in every cross section is calculated based on reference velocity profile plot. The Root mean square error “RMSE” formulation in this case is given by:

$$\text{RMSE} = \sqrt{\frac{1}{N} \sum_{i=1}^N (x_i - \mu_i)^2} \quad (3.4)$$

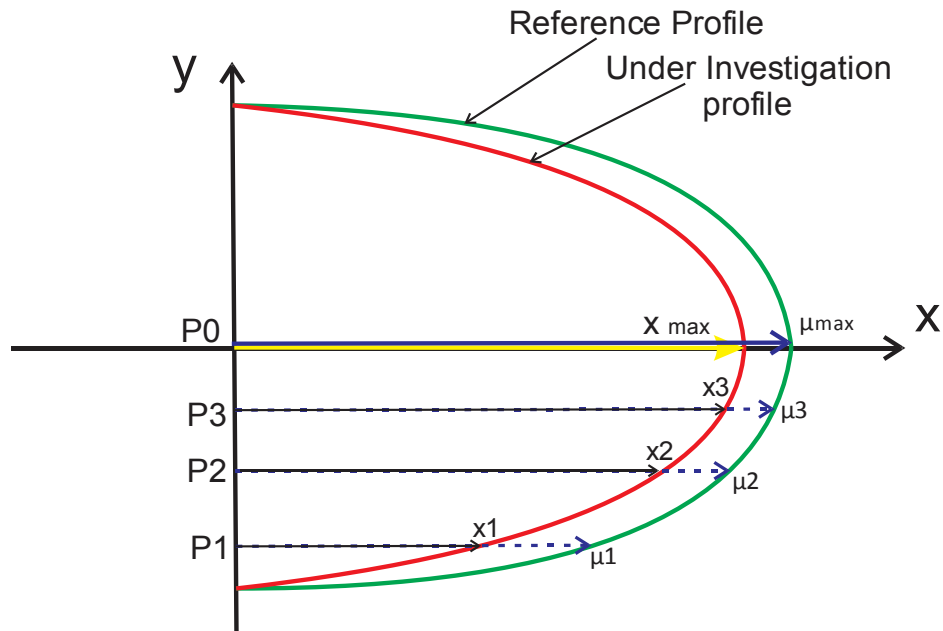


Figure 3.6. Schematics of comparing the velocity values under the investigated velocity profiles at the same location vs. the reference profile.

The error percentage between the points (P0,P1,P2,P3) in one investigated cross-section and reference-profile cross-section comes from RMSPE, which is the root mean square percentage error [35]. The (3.5) illustrates the RMSPE formulation. In both of (3.4) and (3.5), the x_i is the velocity value on analyzed cross section at point “i” and the “ μ_i ” is that value in reference profile at the fully developed region.

$$\text{RMSPE} = \sqrt{\frac{1}{N} \sum_{i=1}^N \left[\left(\frac{x_i - \mu_i}{x_i} \right) \times 100 \right]^2} \quad (3.5)$$

In table 3.1, the results of the simulated fluid flow in a 1 ½ inch pipe are studied. The velocity values in nine different investigated cross-sections as well as the reference profile are

presented. In every individual cross section 4 points are studied, figure 3.5. These points include “P0, P1, P2, P3”. The maximum velocity value occurs at the center of the pipe and it is named “P0”.

Table 3.1. Velocity value variation in different cross-sections on velocity profile plot (Re 80000).

Flow initial Condition	Exact entry Length based on formulation (3.3)	Investigated cross section	Velocity Values in different points “cm/s”				Root Mean Square Error “RMSE”	RMSPE %
			P1	P2	P3	Max Point "P0"		
Reynolds 80000 & Velocity 210 cm/s	22.8 D	Velocity @ 10 D	213.68	232.78	234.56	234.66	13.8889	5.6
		Velocity @ 11 D	211.17	234.59	236.51	236.42	12.1304	4.86
		Velocity @ 13 D	210.15	237.28	239.94	239.92	9.4349	3.78
		Velocity @ 14 D	209.37	238.02	241.58	241.63	8.1609	3.26
		Velocity @ 15D	208.36	236.93	242.71	243.36	7.157	2.85
		Velocity @ 16 D	206.43	238.88	244.56	245.07	5.6746	2.24
		Velocity @ 17 D	204.6	239.26	245.97	246.87	4.5612	1.81
		Velocity @ 19 D	204.64	241.06	248.85	249.59	2.7129	1.08
		Velocity @ 21.5 D	205.02	238.5	250.29	252.71	1.2032	0.5
		Reference profile Velocity @ 22.8D	205.89	239.91	251.33	254.11	0	0

It should be mentioned that, the “RMSE” and “RMSPE” column of table 3.1, are calculated according to the (3.4) and (3.5). As an example for “17 D” cross-section based on equation (3.4), the RMSE value will be “4.5612 cm/s”. Where the “ x_i ” and “ μ_i ” are given by:

$$\begin{cases} \mu_i = [205.89 & 239.91 & 251.33 & 254.11] \\ x_i = [204.6 & 239.26 & 245.97 & 246.87] \end{cases} \quad (3.6)$$

Therefore, the RMSPE percentage according to the (3.5) will be:

$$\begin{aligned} \text{RMSPE} &= \sqrt{\frac{1}{4} \left[\left[\left(\frac{246.87 - 254.11}{246.87} \right) \times 100 \right]^2 + \left[\left(\frac{245.97 - 251.33}{245.97} \right) \times 100 \right]^2 + \right. \\ &\quad \left. \left[\left(\frac{239.26 - 239.91}{239.26} \right) \times 100 \right]^2 + \left[\left(\frac{204.6 - 205.89}{204.6} \right) \times 100 \right]^2 \right]} \quad (3.7) \\ &= 1.8\% \end{aligned}$$

With regards to the results in table 3.1, it comes clear that using “10 D” position as estimation for entry length in the high Reynolds number range will induce a significant error expressed through the RMSPE (5.6%), which will definitely affect the accuracy of the results. Logically, one should be searching for an optimum entry length. However, more accurate flow could be also obtained if the domain could be divided in zones where the flow could be more effectively monitored.

The most obvious finding from the table 3.1, is defining a 14D entry distance as an optimum cross section for the Re range up to 80,000. At 14D cross section the RMSPE is approximately 3.2%, which suggests it as a recommendable entry distance in the selected Re range. Thus the value will be considered as the optimum sensor positioning location through the pipe.

In the entry identified distance, which one could consider that the laminar flow is re-established for the entire range of considered Re values, the sensing elements are positioned. The measurement system consists of three small beams of three different lengths that will capture the dynamic pressure induced by the flow at three different points on the flow path within the same cross section. Under such conditions, the signals collected from the three sensors will be used to reconstruct the profile of the flow parabola.

The parabola will be related to the flow after applying the thermal correction factor, which will be experimentally established. This information can be collected from a thermocouple that could be positioned anywhere along the flow path. The deflection of the three beams is modeled using FEA. The model is built as described above and the analysis of the deflection of the beam coupling with the fluid flow is established using ANSYS software.

3.3 Principles of the Model

The cantilevers platform as proposed earlier offers the advantages of good sensitivity, little interference with the flow and capability to produce it at a low-cost. These advantages would enable investigating different geometries and materials for increasing the sensitivity of these devices and reducing the flow interference.

Two types of measurement applications of the cantilever beam configuration are widely used for sensing applications. First, the static mode, where the cantilever bends due to mass or the static force acting upon it. The dynamic mode is the second type of measurement and normally employed with cantilever beams. Here, the resonant frequency of the beam is measured as it shifts due to the mass addition to the structure. The variations in deflection /

angle or resonant frequency are correlated to the physical quantity of interest. The differences in resonant frequency correlated to the amount of added mass [36].

In the dynamic mode measuring technique, the cantilever resonant frequency is dependent on the stiffness of the beam in bending and the equivalent mass of the system. Equation (3.8) illustrates the above, where the “k” and “m*” are the spring constant and effective mass of the cantilever, respectively. Resonance differences is correlated to the amount of added mass. In regards to the formulation, added mass shifts the resonant frequency toward to a lower frequency value. The dynamic mode performance is directly related to the surrounded media, as an example in the liquid, the higher viscosity causes higher damping value which is less suitable for this measurement mode.

$$f_r = \frac{1}{2\pi} \sqrt{\frac{k}{m^*}} \quad (3.8)$$

The measurement technique for our application is based on the static mode. The cantilever beam bends due to induced distributed force generated by the flow. Theoretically, bended cantilever beam produces a strain intensity, which is detectable by positioning piezo-resistive gauge on beam at the most suitable location. In the following sections, the static mode of measurement will be discuss in detail.

3.3.1 Dynamic pressure variation in the cross-section of the pipe

One of the important characteristics of the fluid flow is the dynamic pressure, which has a direct effect on the flow rate. Theoretically the dynamic pressure is the ratio of kinetic energy to the unite volume of a particle of the fluid [37]. The main goal of studying the dynamic

pressure trend is to attempt to predict the fluid flow behaviour through the pipe. The governing equations of the fluid flow have been known for long term as the Navier-Stocks equations. In our flow in the pipe, by considering an incompressible, isothermal, and Newtonian flow, the application of Newton second law to the viscous flow yields equations expressed in (3.9). The spatial coordinates of x and y is according to figure 3.4. The density ρ and viscosity μ are assumed constant.

$$\frac{\partial u}{\partial x} + \frac{\partial v}{\partial y} + \frac{\partial w}{\partial z} = 0 \quad (3.9)$$

Where the velocity is determined by below relationship:

$$\vec{V} = (u(x, y, z), v(x, y, z), w(x, y, z)) \quad (3.10)$$

The vector form of the Navier-Stocks equation is defined by:

$$\rho \frac{D\vec{V}}{Dt} = -\nabla P + \rho \vec{g} + \mu \nabla^2 \vec{V} \quad (3.11)$$

Thus in case of uniform velocity in one direction the equation will become:

$$\rho \left(\frac{\partial u}{\partial t} + u \frac{\partial u}{\partial x} + v \frac{\partial u}{\partial y} + w \frac{\partial u}{\partial z} \right) = -\frac{\partial P}{\partial x} + \rho \vec{g}_x + \mu \left(\frac{\partial^2 u}{\partial x^2} + \frac{\partial^2 u}{\partial y^2} + \frac{\partial^2 u}{\partial z^2} \right) \quad (3.12)$$

The possible hypothesis under the current condition is assuming the steady flow situation, so the term of “ $\frac{\partial u}{\partial t}$ ” will be equal to zero. Moreover, the velocity appears only in x-direction, so the v and w terms will be eliminated. In addition, the acceleration in x-direction is zero and also, the hydro-static pressure in a horizontal pipe in the vertical direction is negligible. Thus the final equation will become:

$$\rho u \frac{du}{dx} = - \frac{dP}{dx} \Rightarrow \frac{dP}{dx} + \rho u \frac{du}{dx} = 0 \quad (3.13)$$

Where ρ is the density of the fluid and p is the pressure, x is the direction of the flow, and u is the velocity in the “x-direction”. Obviously, in incompressible flow the density is constant, so it is allowed to bring the “ $\rho \times u$ ” term inside the differential:

$$\frac{dP}{dx} + \frac{d}{dx} \left(\frac{\rho u^2}{2} \right) = 0 \quad (3.14)$$

After collecting all:

$$\frac{d}{dx} \left(P + \frac{\rho u^2}{2} \right) = 0 \quad (3.15)$$

By integration of this differential equation:

$$P_s + \frac{\rho u^2}{2} = \text{Constant} = P_{\text{Total}} \quad (3.16)$$

The “ P_s ” term is static pressure and “ $\frac{\rho u^2}{2}$ ” is the dynamic pressure and “ P_{Total} ” is the total pressure. Based on equation (3.16), the dynamic pressure value only depends on velocity along the pipe. In the table 3.2, the dynamic pressure at four different locations is studied. The system configuration and the location of the measurement points are exactly same as figure 3.3 and 3.4. The velocity and dynamic pressure values are investigated in three cross-sections for two Reynolds numbers. In addition, the theoretical estimate of the dynamic pressure based on formulation “ $\frac{\rho u^2}{2}$ ” is inserted to the table in every individual cross-sections.

Table 3.2. Dynamic pressure value, comparison between analytical and numerical results.

Flow Condition	Investigated cross section	P0	P1	P2	P3
Reynolds 3800 & Velocity 10 cm/s, $\rho = 998 \text{ kg/m}^3$	Velocity @ 10.6 D (Numerical solution)	0.1321	0.1007	0.1263	0.1292
	Dynamic Pressure @ 10.6 D (Numerical solution)	8.7928	5.0772	7.9432	8.3481
	Calculated dynamic pressure : $\rho u^2/2$	8.7077	5.0601	7.9619	8.3296
	Error percentage	0.9	0.3	-0.23	0.22
Reynolds 80000 & Velocity 210 cm/s , $\rho = 998 \text{ kg/m}^3$	Velocity @ 10 D (Numerical solution)	2.3466	2.1368	2.3278	2.3456
	Dynamic Pressure @ 10D (Numerical solution)	2748.797	2283.746	2706.668	2747.179
	Calculated dynamic pressure : $\rho u^2/2$	2747.8	2278.4	2703.9	2745.4
	Error percentage	0.0004	0.0023	0.001	0.0006
	Velocity @ 22.8 D (Numerical solution)	2.5411	2.0589	2.3991	2.5133
	Dynamic Pressure @ 22.8 D (Numerical solution)	3222.426	2146.019	2885.381	3151.101
	Calculated dynamic pressure : $\rho u^2/2$	3222.1	2115.3	2872.1	3152
	Error percentage	0.0001	0.0143	0.0046	0.0003

The error comes from the differences between calculated dynamic pressure and numerical dynamic pressure value from numerical solution in ANSYS software. As an example

the velocity and dynamic pressure values for the point “P0” at the cross-section in “22.8 D” are “2.5411 m/s” and “3222.426 Pa”, respectively. Finally, the error percentage is given by:

$$\left\{ \begin{array}{l} P_{D(\text{from ANSYS})} = 3222.426 \\ P_{D(\text{Analytical})} = \frac{\rho u^2}{2} \rightarrow P_D = \frac{998(2.5411 \frac{\text{m}}{\text{s}})^2}{2} = 3222.1 \end{array} \right. \quad (3.17)$$

$$\Delta P = 0.326 \text{ pa} \rightarrow \frac{0.326}{3222.426} \times 100 = 0.0001\% \quad (3.18)$$

Clearly, the errors are small and the dynamic pressure expression is verified in every streamlines.

3.3.2 The configuration of the design

The cantilever configuration is one of simplest mechanical structure, which is fixed at one end and free to the other. Cantilevers have usually rectangular shapes with a large length to thickness ratio. The sensitivity of cantilever beam in static and dynamic modes has a direct dependence on the material properties and the geometry of beam. In geometrical point of view, different shapes (Fig. 3.7) were investigated [36, 38]. As a results of findings, the V-shaped beam is recommended for dynamic mode measurement due to maximizing of the resonance frequency in the cantilever beam. In the static mode which was selected for this application, the configuration of “b” followed by “a” in figure 3.7, are suggested for maximizing the deflection, respectively.

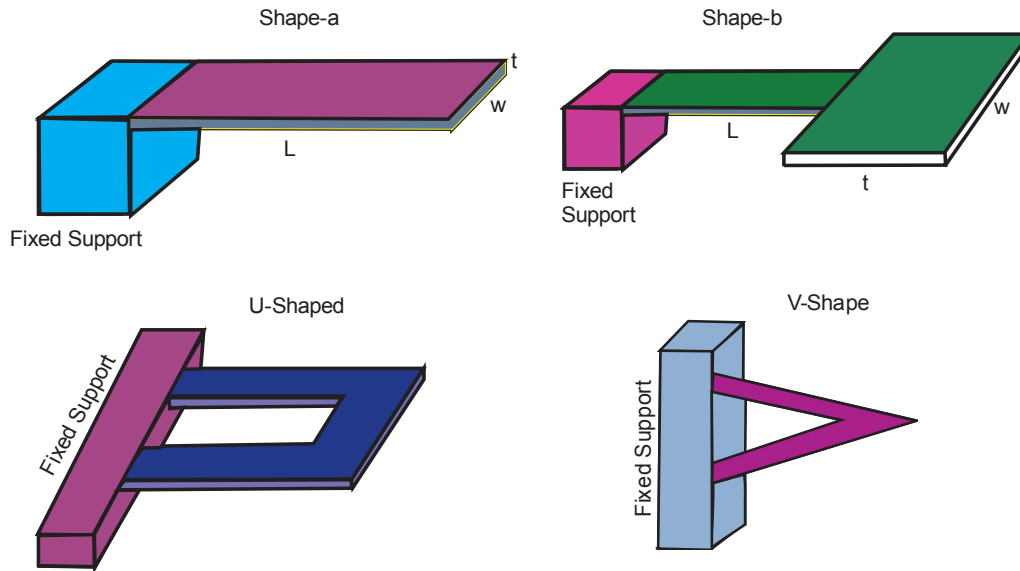


Figure 3.7. Different geometry of cantilever beams

As it is illustrated in the table 3.2, the dynamic pressure and the velocity are varying across the pipe. These variable parameters have a direct influence on the flow value. In this study, the dynamic pressure variation within the cross-section is used as metering variables for measuring the flow. Hence, the configuration of the sensor will be set to follow the principle of operation.

The model is conceived a ring of the same size as pipe, which is made from a type of polyester that it is commercially known as Mellinex339 [39]. The three rectangular cantilever are attached to this ring. The length of the cantilevers are different, hence the dynamic pressure is detected at different locations at the same cross section of the flow. The angular differences between cantilevers are 120° . The schematic view of designed ring is shown in figure 3.8.

The dimensions of the three cantilevers were selected based on size constraints and the results of the numerical analysis. The beams need to yield under the lowest velocity flow such

that flow is detected and metered. Meanwhile, the beams must perform at the maximum velocity without structural damage. The calculations and the multiple run analyses indicated for the cantilevers operating under $Re=3,800$ and $Re=80,000$ in $1\frac{1}{2}$ " pipe, a good sensitivity is obtained when the beams are 2mm wide while the lengths are 3, 4 and respectively 5 mm. The polymer was procured in thicknesses of 0.05 mm which was selected for the same reason indicated above.

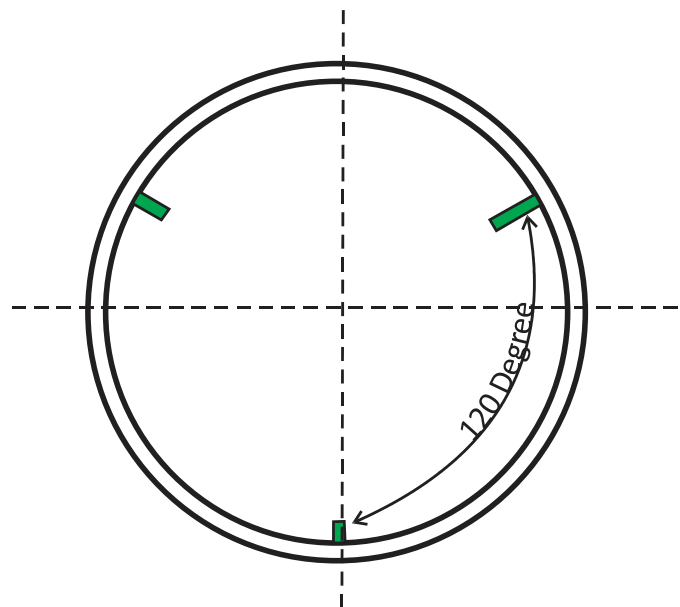


Figure 3.8. Schematic view of Sensor Ring

The selected sizes of the cantilever are also regarded from the perspective of interference with the flow. The area of the beams (24 mm^2) is 2.1% of the total cross section area (1140.09 mm^2). Hence, the interference of the measurement system with the flow is 2.1% which is small enough to be neglected. The table 3.3 illustrates the maximum interference area by three cantilevers. It is shown that the disordered area is approximately 2 percent, which can be neglected.

Table 3.3. Disordered Area-percentage by cantilevers

Area of the 1 ½ inch pipe (mm ²)	Area of the first Cantilever beam (mm ²)	Area of the second Cantilever beam (mm ²)	Area of the third Cantilever beam (mm ²)	Disordered area (mm ²)	Interfered area percentage (%)
1140.09	6	8	10	24	2

The cantilevers will bend due to the dynamic force by the fluid flow upon them. In the section 3.4 the bending phenomena of the cantilever beam is analyzed using both analytical and numerical methods. As illustrated in figure 3.9, the compression and tension forces will generate along the flow facing side and the opposite side of the cantilever beam, which induced strain to the beam.

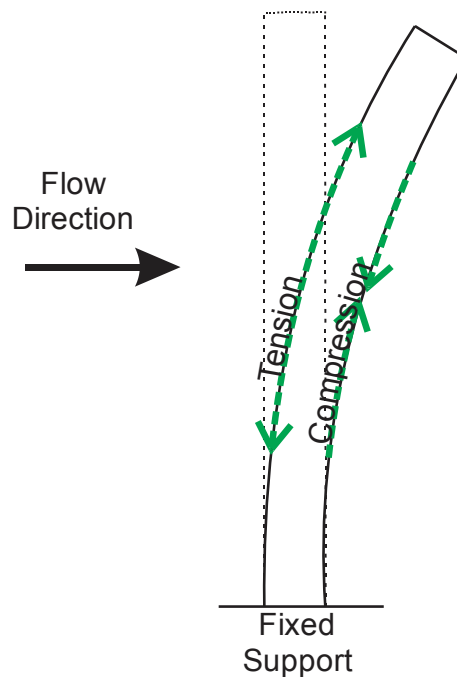


Figure 3.9. Bended cantilever beam induced by flow

The induced strain/deflection to the cantilever is measurable by a strain gauge. One of the considered models of measurement is using a thin layer of piezoresistive material on the surface of cantilevers for monitoring resistance variation. In regard to the piezoresistive principle, resistance variation stems from deflection of the beam. A Wheatstone bridge is used for transforming the deflection/strain to the resistance variation. The resistance variation is in the range of microstrains, thus one amplifying circuit board is designed. Details on the design of the circuit board and optimum strain gage location on the beam will be discussed in the next chapter.

3.4 Analytical principle of induced deflection to the beam by the flow

In this study, the measurement ring consists of three cantilevers instrumented with strain gauges installed using two technologies: printed strain gauge and bonding. The beams are located inside the pipe. According the entry length discussion in section 3.2, the ring is installed at “14D” distance from entrance of the pipe which represents the position of the valve. The dynamic pressure induced by the flow is actually a fluid structure interaction problem. Thus, the entire interaction requires modeling of flow and the induced deflection of the beams.

3.4.1 Structural Phase Theory

As it is discussed in section 3.3, the cantilever platform can be used for sensing in both static and dynamic mode. As mentioned above, the proposed design makes use of the static mode for detecting the dynamic pressure and hence, measuring the flow. Thus, the theoretical part of the static mode measurement is explained in this section.

As it is mentioned in section 3.3.1, the value of the dynamic pressure varies in the cross section of the pipe from the minimum value at wall (zero) to the maximum value at the center of the pipe. As a matter of fact the acting pressure upon cantilever beam is parabolic but given the small segment of the parabola, is assumed as a straight line. Thus the acted force upon the cantilever beam will be a triangular distributed load, figure 3.10 [40]. Where q_0 and L are the distributed load and the length of the beam, respectively.

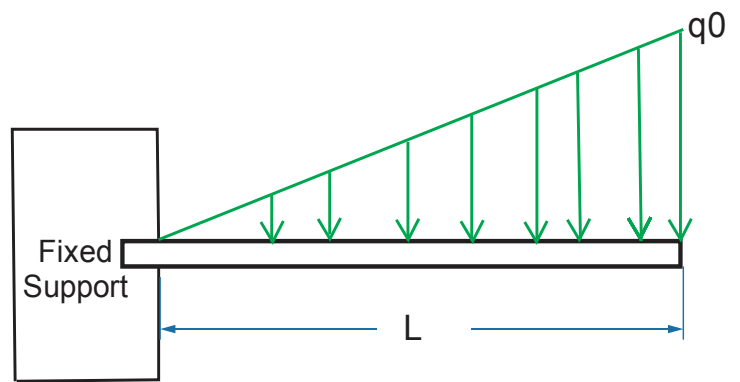


Figure 3.10. The pressure acted upon cantilever beam inside the pipe (Triangular distributed Load)

In this study, the deflection due to the fluid flow is evaluated small using Euler-Bernoulli beam theory. Although it is expected that high values of pressure yield large deflections, small deflection theory is suitable to describe the cases reported in this work. According to the model of bending for Euler's beam, figure 3.11, the governing equation is (3.19). Where the q and Y are the loading of the beam and the displacement of the beam neutral axis, respectively [40]. The term of " EI " is known as flexural rigidity and consists of the young modulus " E " multiply to moment of inertia " I ".

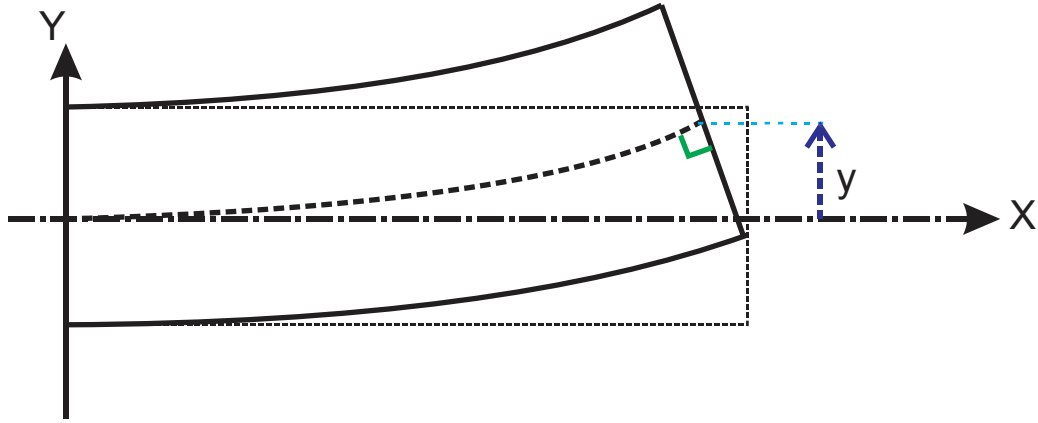


Figure 3.11. Bending model of Euler's beam

$$EI \frac{d^4 y}{dx^4} = q(x) \quad (3.19)$$

The appendix A includes the derivation of the (3.19). Finally the deflection equation after applying the defined boundary conditions, can be written as following:

$$y = -\frac{q_0}{6EI} \left[\frac{x^5}{20L} + \frac{L}{2} x^3 - L^2 x^2 \right] \quad (3.20)$$

Also the slope and the maximum deflection at the tip are given by:

$$\delta_{\max} = y_{x=L} = -\frac{11q_0 L^4}{120 EI} \quad (3.21)$$

$$\theta = \frac{dy}{dx} = -\frac{q_0 L^3}{8 EI} \quad (3.22)$$

The slop and maximum deflection equations, in the large deflection condition are represented in Appendix B [41].

3.4.2 The fluid phase

In fluid phase due to the cylindrical symmetry of the pipe, cylindrical coordinates are used for studying the phenomena in the pipe. The investigated case in this part is a steady laminar flow passing a circular pipe with the radius of “a”, as illustrated in figure 3.12. The velocity is only in z-direction and in the wall of the pipe will decrease to zero, which is called no-slip boundary condition “ $V_z(a) = 0$ “. Thus the velocity is a function of r (3.23). As is mentioned, the velocity profile in laminar flow is parabola, which it will be analytically proved in this section.

$$V_z = f(r) \tag{3.23}$$

$$V_r = V_\theta = 0$$

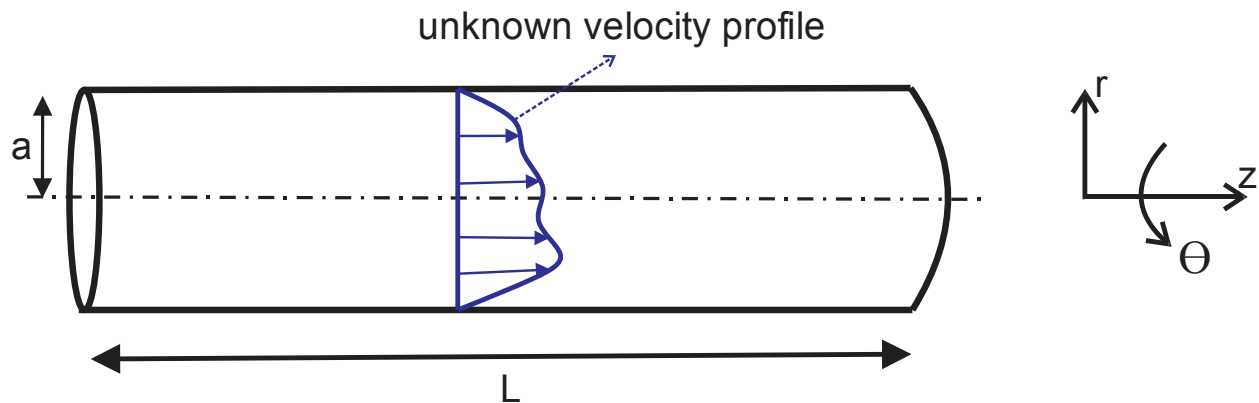


Figure 3.12. The configuration of the case study

The analytical solution for this case study is achieved by applying two conservation equations. First, the conservation of mass which is called continuity equation (3.24) will be applied.

$$\frac{\partial \rho}{\partial t} + \frac{1}{r} \frac{\partial}{\partial r} (\rho r V_r) + \frac{1}{r} \frac{\partial}{\partial \theta} (\rho V_\theta) + \frac{\partial}{\partial z} (\rho V_z) = 0 \quad (3.24)$$

Since the case is a steady state problem, any derivatives to “t” will be eliminated. According to the (3.23) the second, third and the fourth terms of the equation (3.24) will be zero, also. Thus it shows that, we are able to satisfy the conservation of mass but it is not giving any useful information for determining the form of the velocity profile.

Another conservation law is the conservation of the momentum. In the case of incompressible-Newtonian fluid, the law is known as Navier-Stocks equation. The Navier-Stocks equation consists of three components form. The equations of (3.25), (3.26) and (3.27) belong to r, θ and z components, respectively.

$$\rho \left(\frac{\partial V_r}{\partial t} + V_r \frac{\partial V_r}{\partial r} + \frac{V_\theta}{r} \frac{\partial V_r}{\partial \theta} - \frac{V_\theta^2}{r} + V_z \frac{\partial V_r}{\partial z} \right) = \quad (3.25)$$

$$- \frac{\partial P}{\partial r} + \rho g_r + \mu \left[\frac{\partial}{\partial r} \left(\frac{1}{r} \frac{\partial}{\partial r} (r V_r) \right) + \frac{1}{r^2} \frac{\partial^2 V_r}{\partial \theta^2} - \frac{2}{r^2} \frac{\partial V_\theta}{\partial \theta} + \frac{\partial^2 V_r}{\partial z^2} \right]$$

$$\rho \left(\frac{\partial V_\theta}{\partial t} + V_r \frac{\partial V_\theta}{\partial r} + \frac{V_\theta}{r} \frac{\partial V_\theta}{\partial \theta} + \frac{V_\theta V_r}{r} + V_z \frac{\partial V_\theta}{\partial z} \right) = \quad (3.26)$$

$$- \frac{1}{r} \frac{\partial P}{\partial \theta} + \rho g_\theta + \mu \left[\frac{\partial}{\partial r} \left(\frac{1}{r} \frac{\partial}{\partial r} (r V_\theta) \right) + \frac{1}{r^2} \frac{\partial^2 V_\theta}{\partial \theta^2} + \frac{2}{r^2} \frac{\partial V_r}{\partial \theta} + \frac{\partial^2 V_\theta}{\partial z^2} \right]$$

$$\rho \left(\frac{\partial V_z}{\partial t} + V_r \frac{\partial V_z}{\partial r} + \frac{V_\theta}{r} \frac{\partial V_z}{\partial \theta} + V_z \frac{\partial V_z}{\partial z} \right) \quad (3.27)$$

$$= - \frac{\partial P}{\partial z} + \rho g_z + \mu \left[\frac{1}{r} \frac{\partial}{\partial r} \left(r \frac{\partial V_z}{\partial r} \right) + \frac{1}{r^2} \frac{\partial^2 V_z}{\partial \theta^2} + \frac{\partial^2 V_z}{\partial z^2} \right]$$

Where the V_r, V_θ, V_z are the velocity in r, θ and z direction, respectively. From the discussion in section 3.3.1, the dynamic pressure is a function of velocity and, the static pressure is constant in individual cross-sections. Thus the term P in Navier-Stocks equation is the static pressure, which is independent from velocity. The term μ is the dynamic-viscosity term.

In this investigation the flow velocity was assumed as steady state, so the acceleration is zero. It means that any differential terms into t such as $\frac{\partial V_r}{\partial t}$ can be eliminated. Also the gravity terms are negligible in the context of this case. Moreover, according to the (3.23), any term that includes V_r or V_θ will be zero and will not contribute in the equations. Since V_z is only function of r , its derivatives to the z and θ will be zero. The simplified final form of equation for the r, θ and z -component equations are given by (3.28), (3.29), and (3.30), respectively.

$$\frac{\partial P}{\partial r} = 0 \Rightarrow P \neq f(r) \quad (3.28)$$

$$\frac{\partial P}{\partial \theta} = 0 \Rightarrow P \neq f(\theta) \quad (3.29)$$

$$\frac{\partial P}{\partial z} = \frac{\mu}{r} \frac{\partial}{\partial r} \left(r \frac{\partial V_z}{\partial r} \right) \quad (3.30)$$

The equations (3.28) and (3.29) indicate that, the static pressure value is neither function of r , nor function of θ , which means that it is only function of the z . The equation (3.30) is a second order differential equation, which by two boundary conditions, is solvable. These two boundary conditions are:

$$\text{BCs} \begin{cases} @ r = a \Rightarrow V_z(a) = 0 & \text{(I)} \\ @ r = 0 \Rightarrow V_z = \text{Finite quantity} & \text{(II)} \end{cases} \quad (3.31)$$

At the equation (3.30), the quantity on the left hand side is a function of z and the right hand side quantity is a function of r . Thus the only way that a function of z can be equal to a function of r , is that both are equal to a constant (3.32). Since the right and left side of the equation (3.30) are the function of z and r only, the partial derivatives are changed to regular derivatives in equation (3.32).

$$\frac{dP}{dz} = \frac{\mu}{r} \frac{d}{dr} \left(r \frac{dV_z}{dr} \right) = \text{constant} \quad (3.32)$$

The (3.32) consists of two equations (3.33). The first equation indicates that the constant value should be a slope of the pressure as a function of z . Therefore the static pressure in z -direction varies linearly as illustrated in figure 3.13.

$$\begin{cases} \frac{dP}{dz} = \text{constant} \Rightarrow P(z) = \text{linear} & \text{(I)} \\ \frac{\mu}{r} \frac{d}{dr} \left(r \frac{dV_z}{dr} \right) = \text{constant} & \text{(II)} \end{cases} \quad (3.33)$$

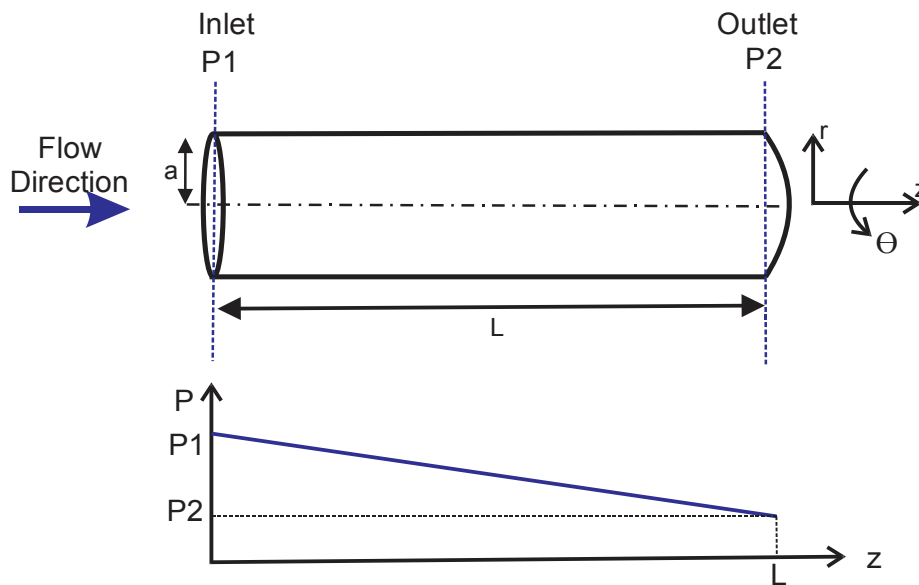


Figure 3.13. The static pressure value is decreasing linearly from P_1 to P_2 .

The pressure difference between inlet and outlet cross-section areas is called pressure drop and is given by (3.34). In order to have a flow in the positive z-direction the P_1 should be higher than P_2 . According to the figure 3.13, the first equation of (3.33) can be expressed as the pressure difference at the inlet and outlet over the position differences at the inlet and outlet of the pipe in z-direction (3.35).

$$\Delta P = P_1 - P_2 \quad (3.34)$$

$$\frac{dP}{dz} = \frac{P_2 - P_1}{z_2 - z_1} = \frac{P_2 - P_1}{L} = -\frac{\Delta P}{L} \quad (3.35)$$

The below equation is the final form of the equation (3.32), which is a second order ordinary differential equation for the $V_z(r)$.

$$\frac{dP}{dz} = -\frac{\Delta P}{L} = \frac{\mu}{r} \frac{d}{dr} \left(r \frac{dV_z}{dr} \right) \quad (3.36)$$

The above ODE can be solved by integration. The final form of the velocity equation is given by (3.37).

$$V_z = -\frac{r^2 \Delta P}{4\mu L} + C_1 \ln(r) + C_2 \quad (3.37)$$

According to the defined boundary condition in (3.31), by applying the no-slip boundary condition at the wall of the pipe, the C_2 value is determined.

$$C_2 = \frac{a^2 \Delta P}{4\mu L} - C_1 \ln(a) \quad (3.38)$$

Based on second boundary condition of (3.31), by substituting the zero value instead of r , the velocity equation will be:

$$V_z = 0 + C_1 \ln(0) + C_2 \quad (3.39)$$

In equation (3.39) the natural log of the zero goes minus infinity, which it does not make sense. Moreover, the velocity in center line of the pipe cannot be infinity and it should be a finite value. Thus the only way to have finite velocity value inside the pipe is “C₁=0”. The final form of the (3.37) is given by:

$$V_z = \frac{a^2 \Delta P}{4\mu L} \left(1 - \frac{r^2}{a^2}\right) \quad (3.40)$$

The term of “r²” in the equation (3.40), proved that the velocity profile has a parabola shape. On the other hand as it is noticed in section (3.3.1), the dynamic pressure value is a function of velocity. In addition according to the (3.40), the parabolic velocity profile is a function of radius of the pipe “r”. Consequently, it has been proved that the dynamic pressure value varies at one cross-section along the r-direction.

The interaction between fluid and cantilever beam inside the pipe has an interaction fluid - structure coupling. In this coupling, the pressure induced from the fluid flow will be applied to the beam. This pressure is called total pressure value, which consists of two terms, dynamic pressure “P_D” and static pressure “P_s”. Due to the constant static pressure in the individual cross-section, the only varying pressure term is P_D. Deriving the total pressure value from the final form of the velocity profile equation (3.40), at every point in cross-section of the pipe is a very cumbersome process. Thus the numerical approach is carried out by ANSYS software.

3.5 The results of the numerical simulation

The model geometry consists of a horizontal flow pipe, where the designed sensor ring, figure 3.8, acts as an obstacle against fluid flow. The air as a fluid flows from right to left in minus x-direction along center-line of the pipe, figure 3.14. The transported fluid is considered as an incompressible, isothermal Newtonian flow, which density ρ and viscosity μ are constant.

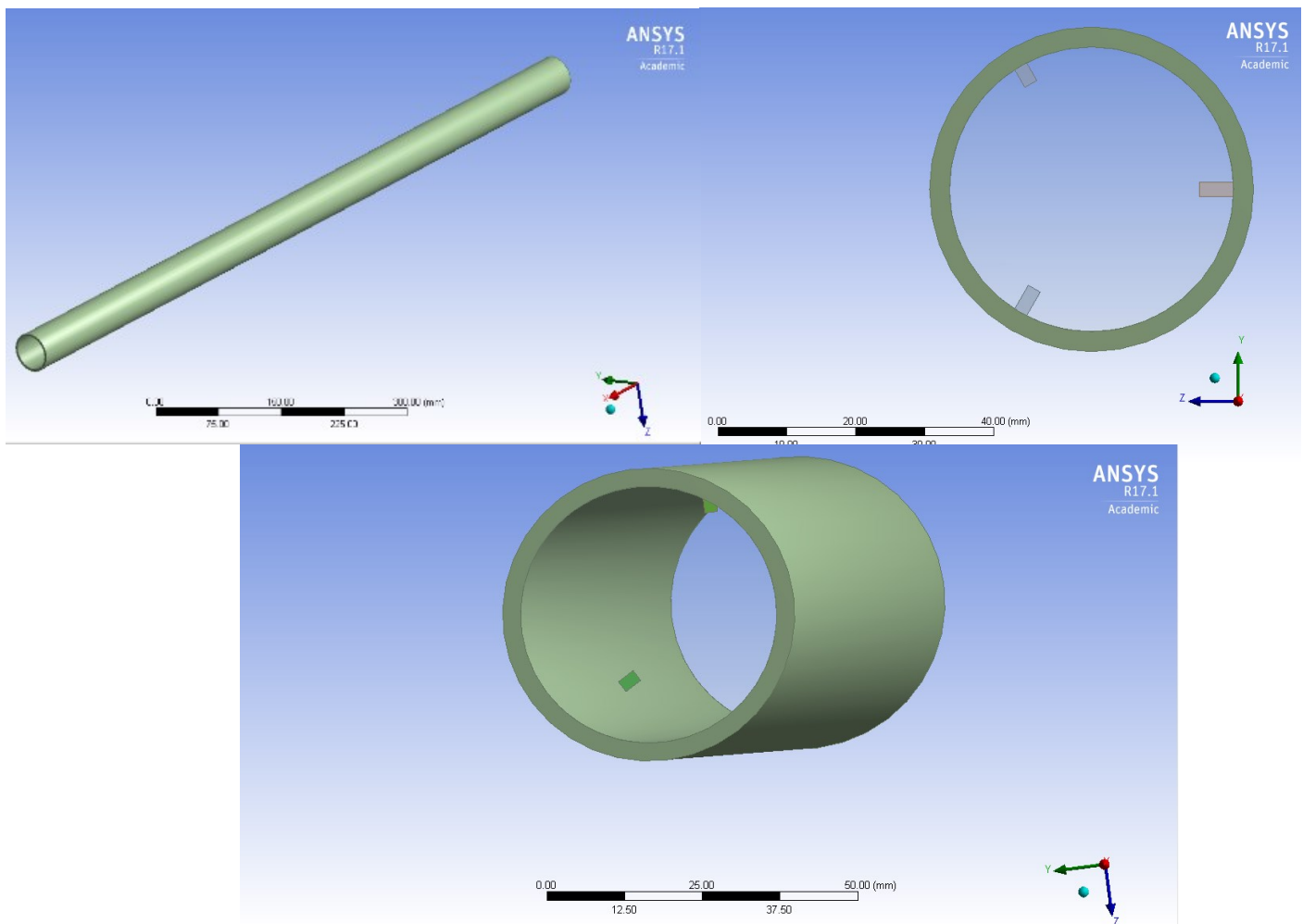


Figure 3.14. The schematic view of sensor ring inside the pipe

The numerical solutions are carried out by ANSYS WORKBENCH 17. Different modules are used for combining the fluid structure coupling nature of phenomena such as Design Modeller,

Mesh tool, Fluent (computational fluid dynamic “CFD” solver), and Static Structural (quasi-static solver).

3.5.1 Computational fluid dynamic (Fluent)

In CFD modeling a necessary condition to ensure is that the CAD model to be “water tight”. This means that all surfaces must be knitted and gaps if any, must be eliminated. The three rectangular cantilever beam are designed as part of a ring, which the centre coincides the coordinate system. According to entry length explanation, section 3.2, the sensor ring is located at “14D” distance far from the inlet of the pipe. Also, the mechanical properties of the fluid are set to liquid water at 20° C. On the other hand, the material of sensor ring is one type of polyester that called Mellinex339.

According to the experimental limitation in the laboratory, the air is used as fluid instead of the water in this experimental phase. The experimental length of the pipe is around “20D”, and the maximum testing velocity will be around 20 meters per second, so the air is assumed as an incompressible fluid. The experimental work will be discussed in the next chapter.

Due to fluid-structure coupling nature of phenomena, the system is clasified into two different investigation phases: fluent and static-structural. In regard to the geometry of the system, the fluid in the pipe and the three cantilever beams are designed. One end of the beams is fixed to the wall of the pipe. Then the geometry is imported to the meshing tool of the fluent.

The fluent mesh sub-domain generates the mesh of the system. This software has the ability to produce convenient mesh type for CFD, very quickly. Furthermore, it is equipped with

advanced tools for refining the meshed area depending on geometry and tolerance compatibility.

In the fluent-meshing section, the beams are subtracted from the system and only the mesh is generated for the fluid body. To increase the reliability of simulation sufficiently fine mesh is required, particularly where the key parameters of flow performance (pressure, velocity, temperature) vary rapidly.

In terms of boundary conditions, the no-slip boundary condition are defined for the wall of the pipe. From the fluid dynamics point of view, the no-slip condition means zero velocity for fluid in the solid boundary. Hence, the flow will experience velocity gradient near the wall. The “inflation layer meshing” is applied for accurately capturing the variation of the parameters in the boundary layer region [42, 43]. The fine tetrahedral mesh is used for meshing, figure 3.15 and moreover, one sphere of influence is defined around each cantilever for creating smaller meshing elements as illustrated in figure 3.16.

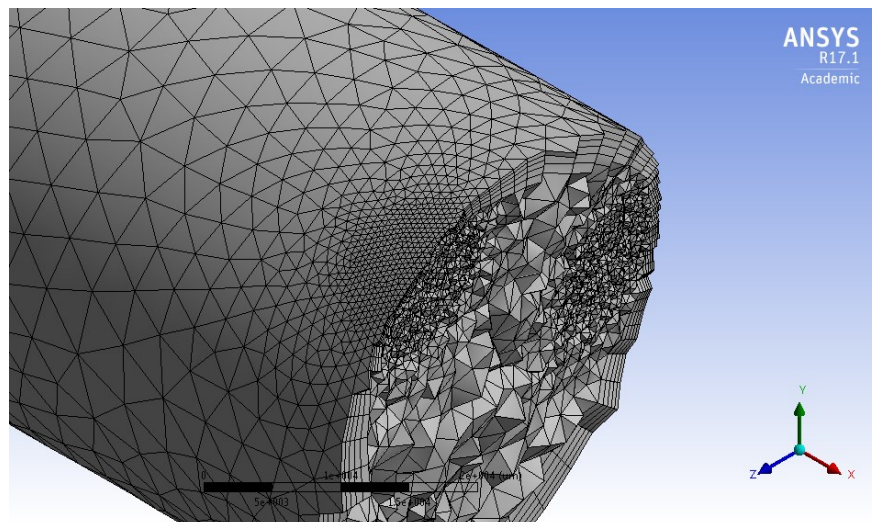


Figure 3.15. Tetrahedral mesh at the sensor location section

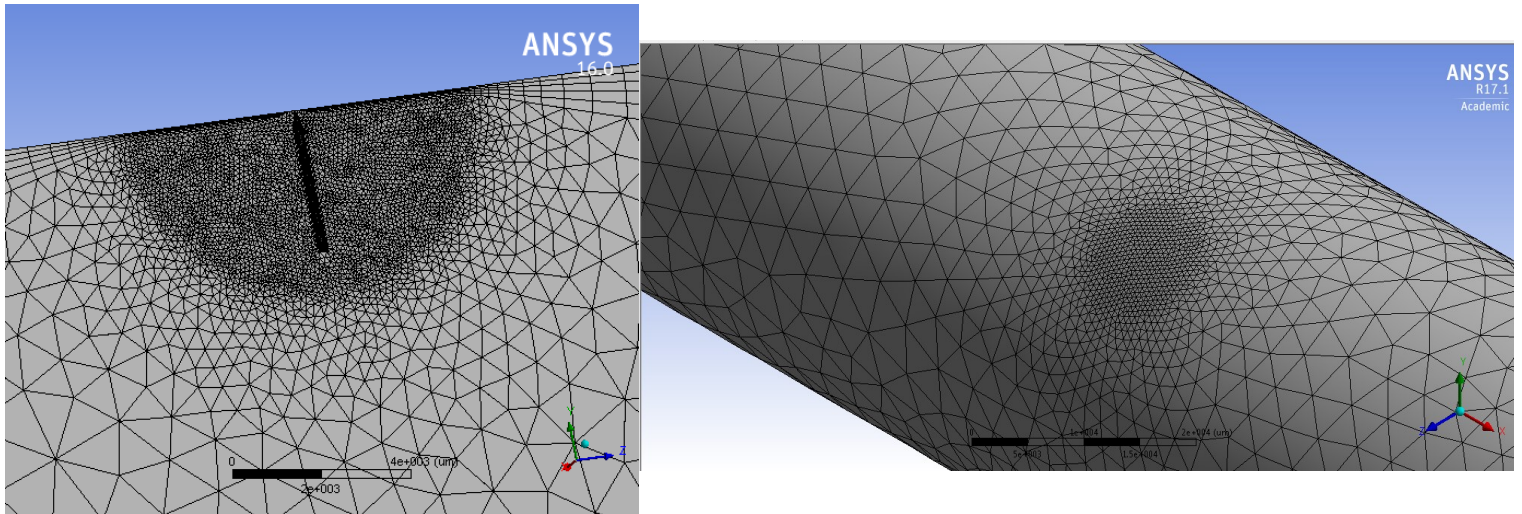


Figure 3.16. Mesh Quality around micro-cantilever beam & pipe.

One sphere of influence with smaller mesh is defined around every cantilever beam

One of the important control feature of the quality of the mesh in the system is skewness factor [44]. The skewness parameter, determines that the generated mesh shape “2D or 3D” how close is to the ideal shape, figure 3.17.

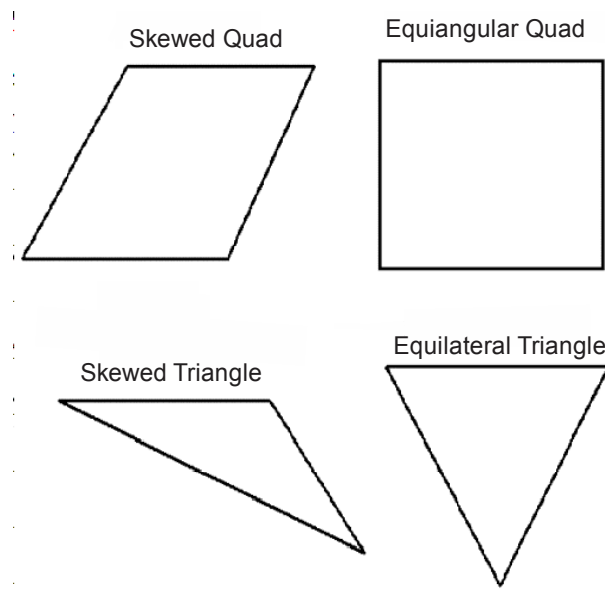


Figure 3.17. Skewed and Ideal shapes of the quadrilaterals and Triangles

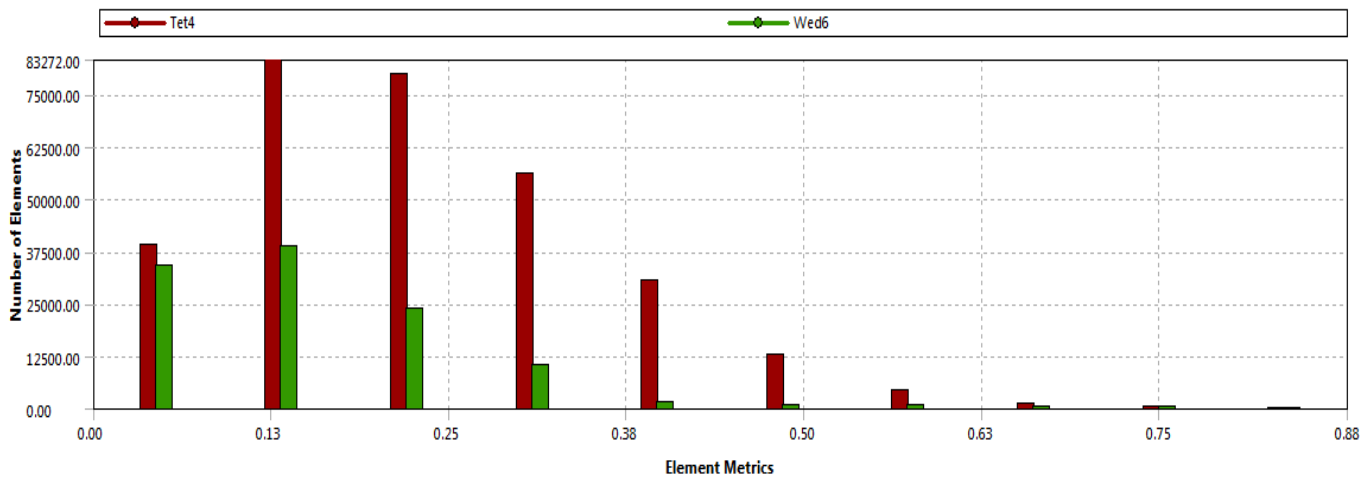


Figure 3.18. Mesh Quality according to the skewness factor

The recommended skewness for a CFD-system analysis is less than 0.98 [45]. The quality of mesh for this study yields skewness value less than 0.75 while the average skewness is around 0.25 which represents using high mesh quality, figure 3.18².

The ANSYS Fluent is the one of the most capable commercial CFD solver on the market, which enables multiple turbulent models such as K-epsilon, K-omega and SST. The k- ϵ and k- ω , are two-transport equation model solving. One of the transport equations solves the system in regard to the kinetic energy “K”. Second transport equation solves turbulent frequency “ ω ” and named as k- ω . In the k- ϵ solving method , the second transport equation solves with regard to the specific turbulent dissipation rate “ ϵ ”[46].

The advantages of the k- ω model consists of better results of the simulation near the walls while for the k- ϵ model, better results of the simulation are yield away from the walls. Thus a combination of both of these techniques represents another solver method which is named as

² Tet4: 4 Node Linear Tetrahedron ; Wed6: 6 Node Linear Wedge (Prism)

“Shear Stress Transport (SST) “model. The recommended setup for the turbulent fluid inside the pipe is SST model [47]. Consequently, the SST model is applied in this simulation.

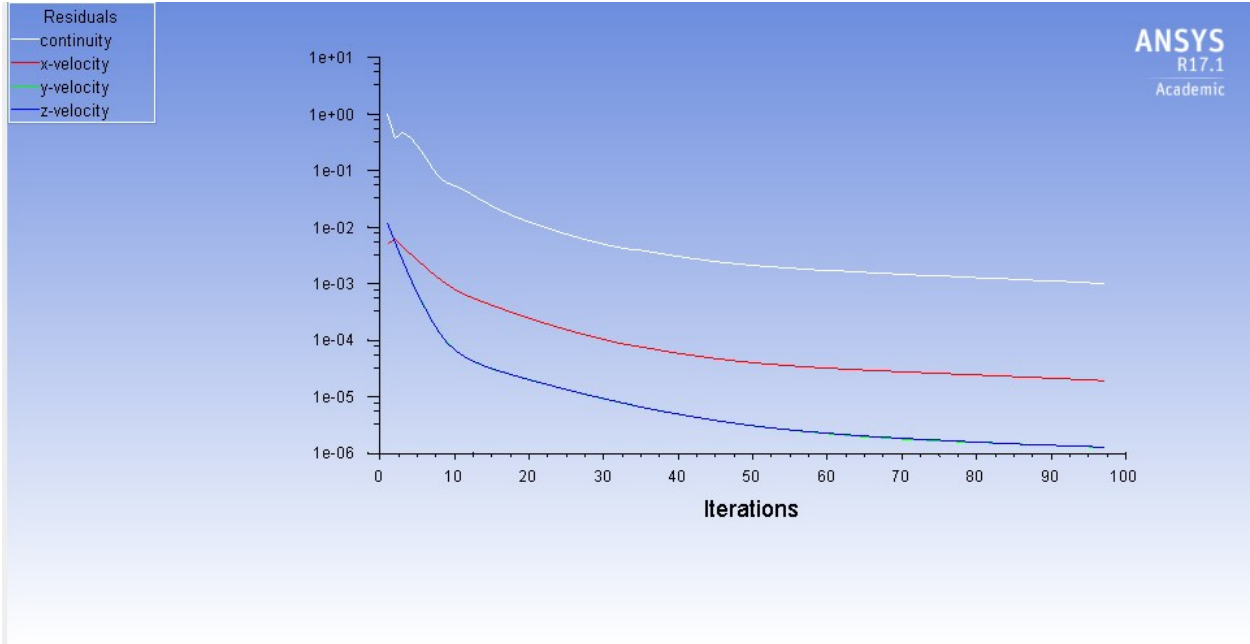


Figure 3.19. Solution convergence yields by ANSYS FLUENT

The solution convergence condition will occur, when the residual of the related parameters in solving process, yield downwards to zero. The figure 3.19, illustrates the convergence trend of the SST-solution, in regard to the four different related parameters. The SST model reaches very good convergence under 1e⁻⁵ of the total residual value.

The fluid flow separation is clearly demonstrated by using velocity vectors. The figure 3.20, shows the impact of the fluid to the beam and creation of a vortex behind it. The induced pressure to the cantilever beam stem from the fluid-solid contact in the front face of the beam and vortex development in the back side of the beam.

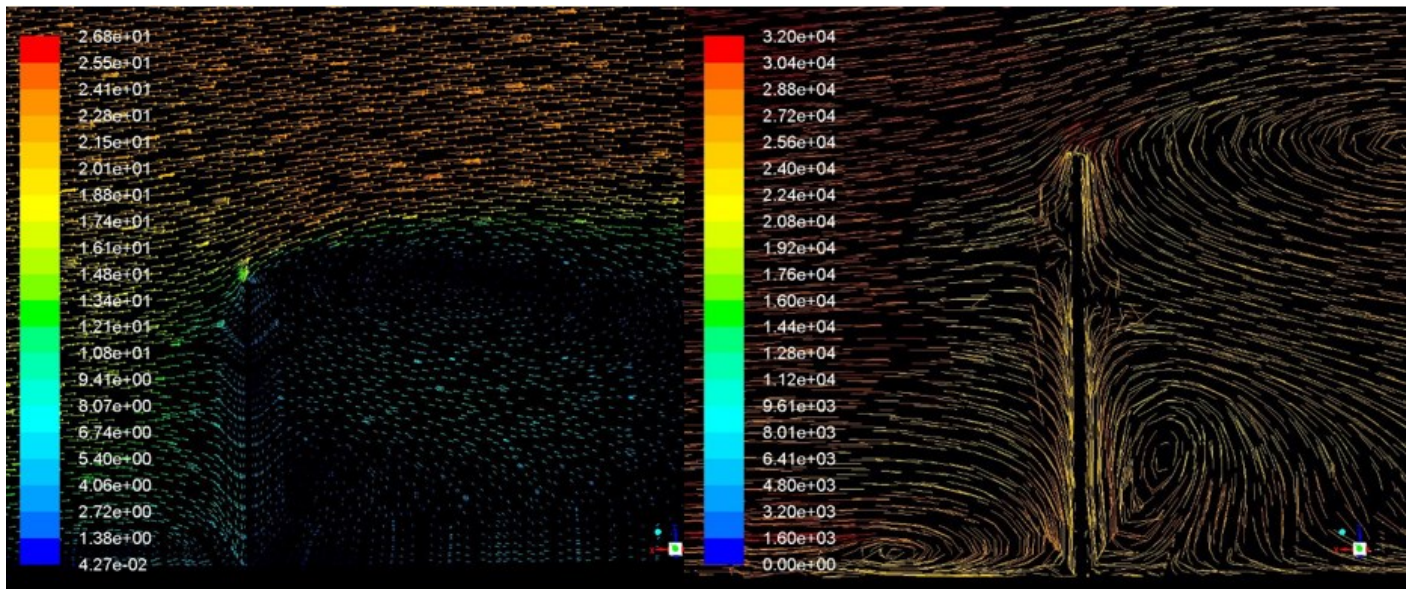


Figure 3.20. The flow hits the beam and creates vortex behind the beam.

3.5.2 Static Structural Solver

Further, the dynamic pressure results from the Fluent solver, are applied on the measurement cantilever beams. The one end of cantilever beams is fixed to the wall of the pipe and the other side is free, so they will bend along the flow direction.

As it was mentioned before, the material of the beam is one type of polyester sheet, which is called Mellinex, thus the material properties of the beams in this phase are well defined based on the Mellinex mechanical properties. The cantilever beam bends under the action of the pressure calculated from the fluid flow. Different type of results are extracted from simulation such as deformation and strain intensity. The below figures illustrate the reaction of the cantilever beams to fluid flow inside the pipe. The figure 3.21 and 3.22 numerically illustrate that, the transferred pressure from FLUENT, will induce deflection / strain to the beam. In the next chapter, the flow value will predict by this induced strain.

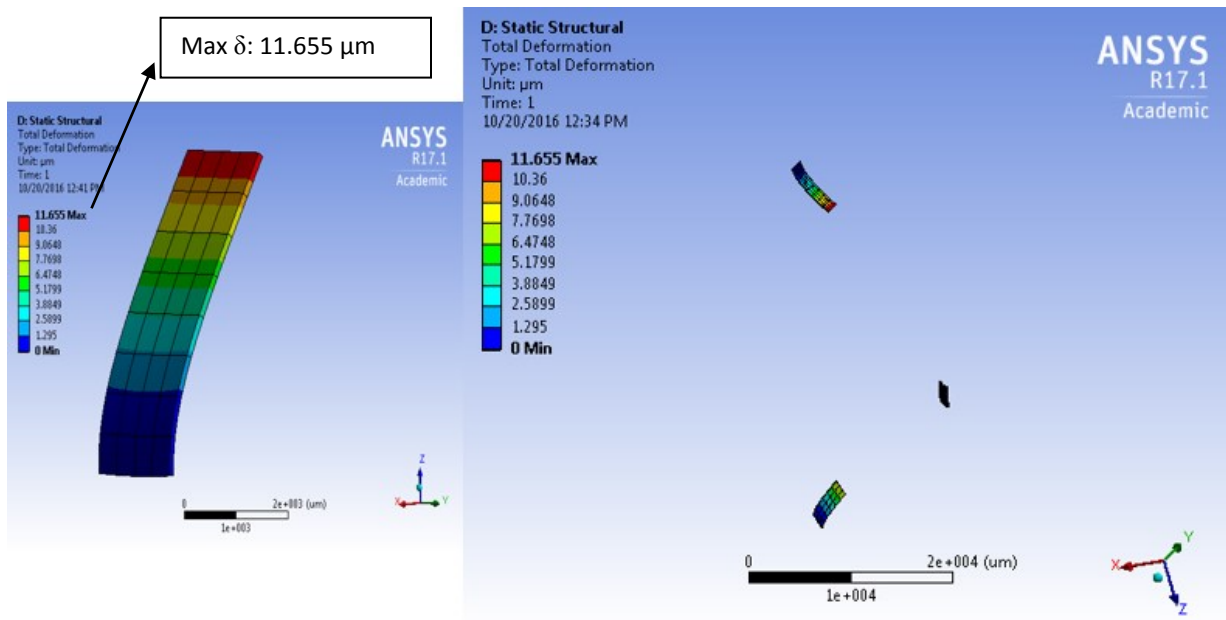


Figure 3.21. Induced deformation in cantilever beams due to water flow
 (The maximum induced deflection is 11.65 μm)

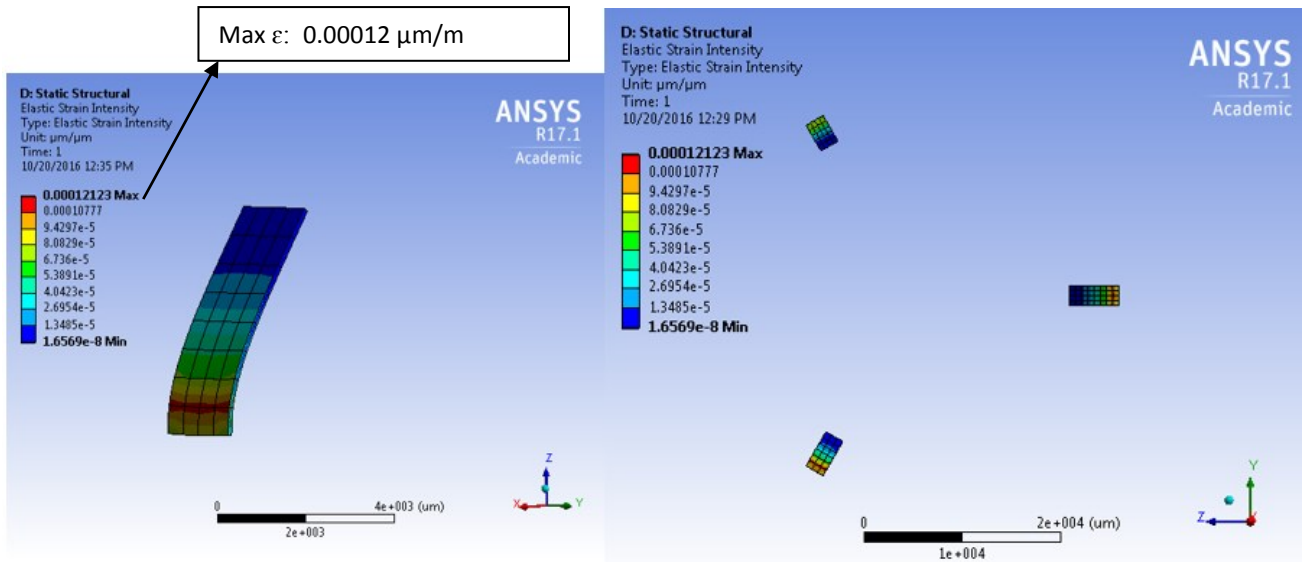


Figure 3.22. Induced elastic strain intensity in cantilever beams due to water flow
 (The maximum induced strain is 0.00012 $\mu\text{m}/\text{m}$)

The figure 3.23 illustrates different strain intensities for different flow values. The figure 3.23 A, shows the $8.9\text{e-}7$ strain in 18.4 litres of the flow. On the other hand, the figure 3.23 B, illustrates the $2.1\text{e-}7$ strain in 1.84 litres of the flow. In fact, strain varies according to the flow variations. Thus the concept of measuring the flow value based on induced strain intensity is proved.

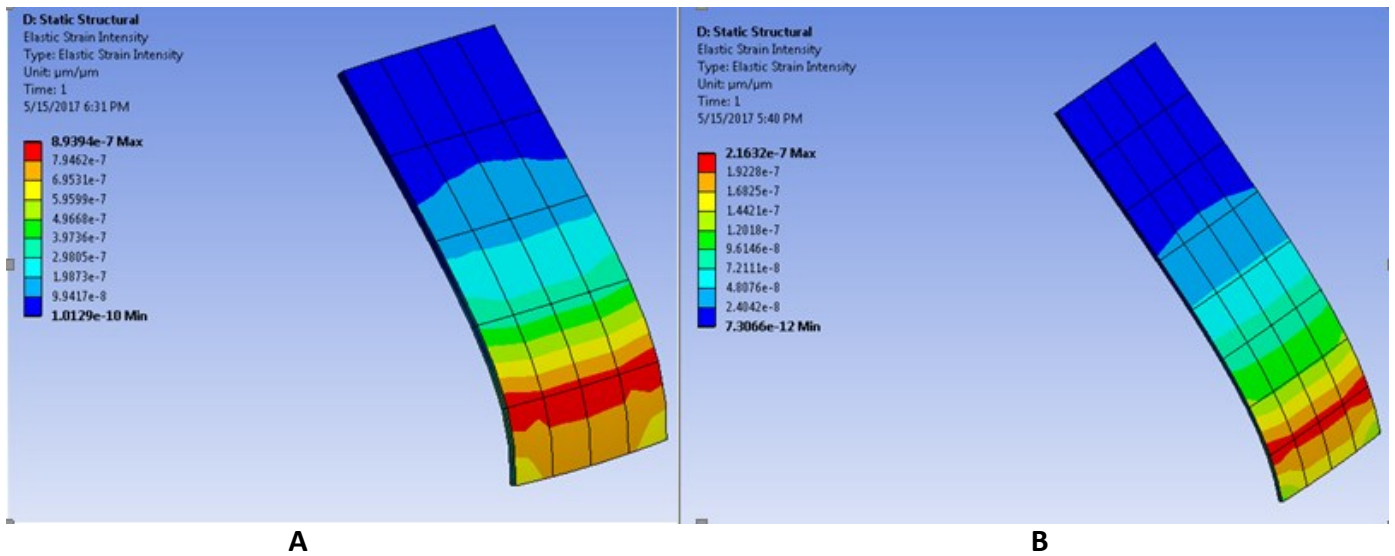


Figure 3.23. A) Strain intensity induced in 18.4 litre flow B) Strain intensity induced in 1.84 litre flow

3.5.3 Analytical induced deflection to a cantilever beam under imported pressure collected from the numerical approach

In this section one example of analytical deflection under distributed pressure collected from the numerical solution of the fluid, is computed. The investigated cantilever beam is a rectangular beam which the length, width and thickness are 5mm, 2mm and 0.05mm, respectively. The material of the beam is Mellinex polyester sheet. The Young modulus for Mellinex is 4×10^9 Pascal. Figure 3.24 shows the imported pressure values and distribution

extracted from the numerical solution to the front face of the cantilever beam. The maximum applied pressure to the beam is 0.06451 Pa.

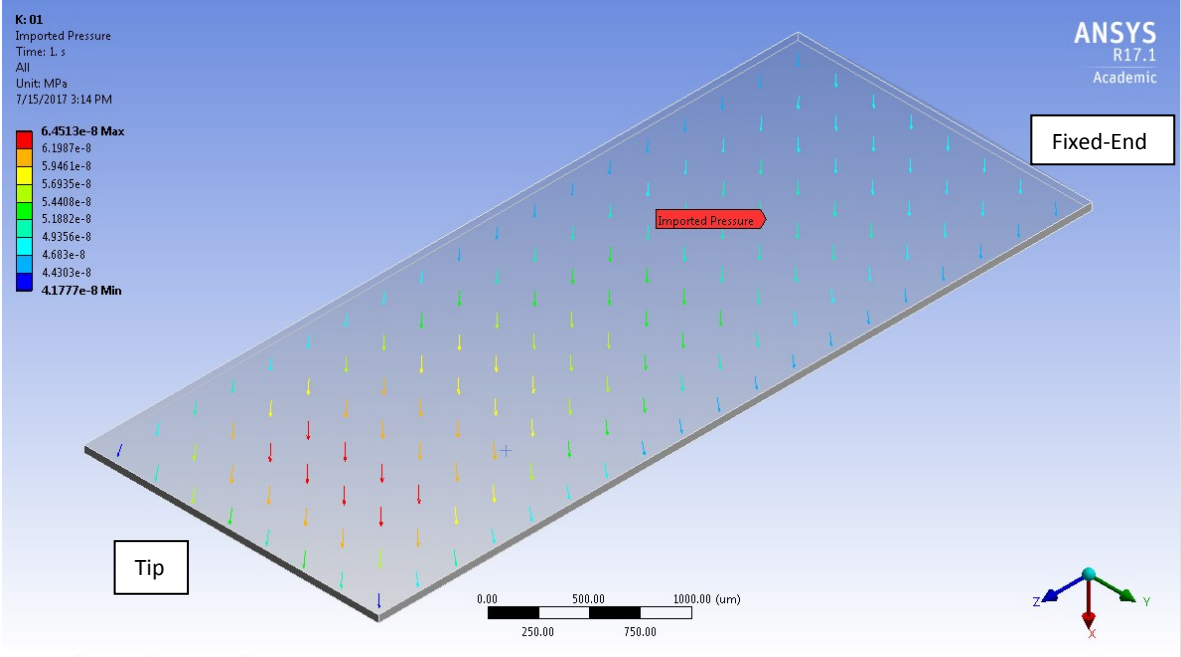


Figure 3.24. Induced pressure distribution to the cantilever beam.

The imported pressure distribution shape in figure 3.24 states that, the triangular pressure distribution assumption in section 3.4.1 is an acceptable hypothesis. The figure 3.25 shows the schematic of this assumption in this case study. The pressure rises from 0 to 0.06451 Pa from the fixed-end to the free-end of the cantilever beam, respectively.

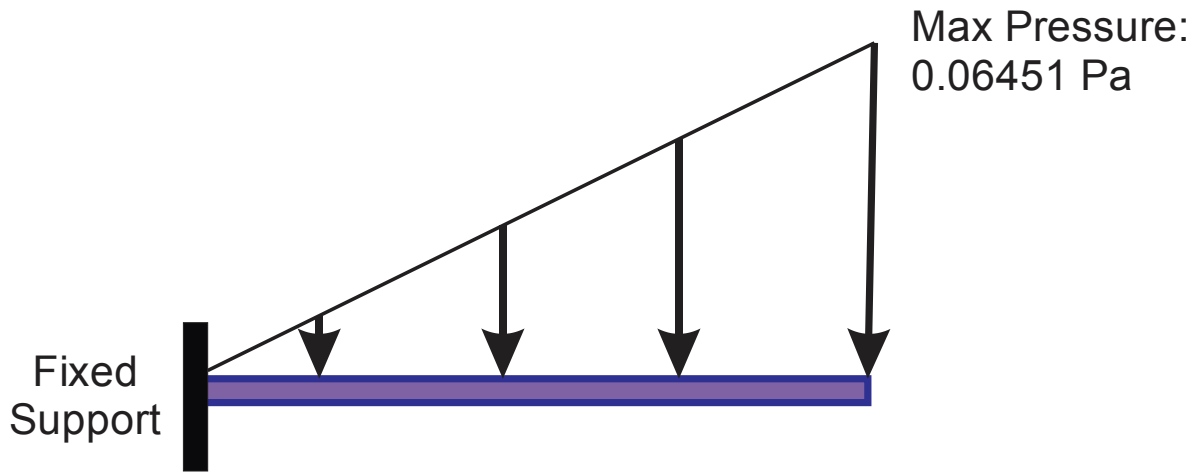


Figure 3.25. The schematic of imported pressure from the numerical solution extracted from the flow simulation

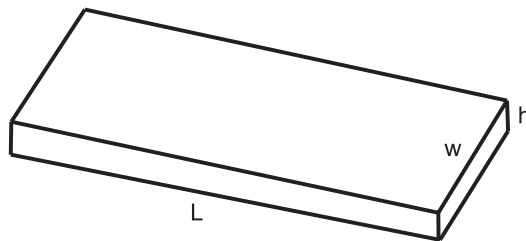
The maximum deflection at the tip of the cantilever beam is given by (3.21). q_0 represents the force over the length of the beam. The unit for q_0 is Newton per meter. Thus the imported pressure should be converted to the q_0 . The equation (3.41) states the relationship between q_0 and the pressure.

$$\text{Pressure} = \frac{\text{Force}}{\text{Area}} \Rightarrow \text{Force} = \text{Pressure} \times \text{Area}$$

$$F = P \times A = P \times (w \times L)$$

$$q_0 = \frac{F}{L} = \frac{P \times (w \times L)}{L} = P \times w = 0.06451 \times 10^6 \times 0.002 = 12.902 \times 10^{-5} \quad (3.41)$$

In the equation (3.21), I is the moment of inertia, which for rectangular cross section beam case is given by:



$$I = \frac{1}{12} w h^3 \Rightarrow I = \frac{1}{12} (0.002) \times (0.00005)^3 = 2.083 \times 10^{-17} \quad (3.42)$$

Consequently the analytical derivation of the deflection value at the tip is given below (3.43).

$$\begin{aligned} \delta_{\max} &= -\frac{11q_0 L^4}{120 EI} = -\frac{11}{120} \frac{(12.902 \times 10^{-5}) \times (0.005)^4}{4 \times 10^9 \times 2.083 \times 10^{-17}} = 0.088 \times 10^{-6} \\ &= 0.088 \mu\text{m} \end{aligned} \quad (3.43)$$

Figure 3.26 illustrates the resulted deflection from the numerical solution, which the maximum deflection value at the tip as “0.094 μm ” yields 6% error with the computed value from the analytic approach (3.43). The generated vortices behind the cantilever beam can be interpreted as one of error sources in this coupled system.

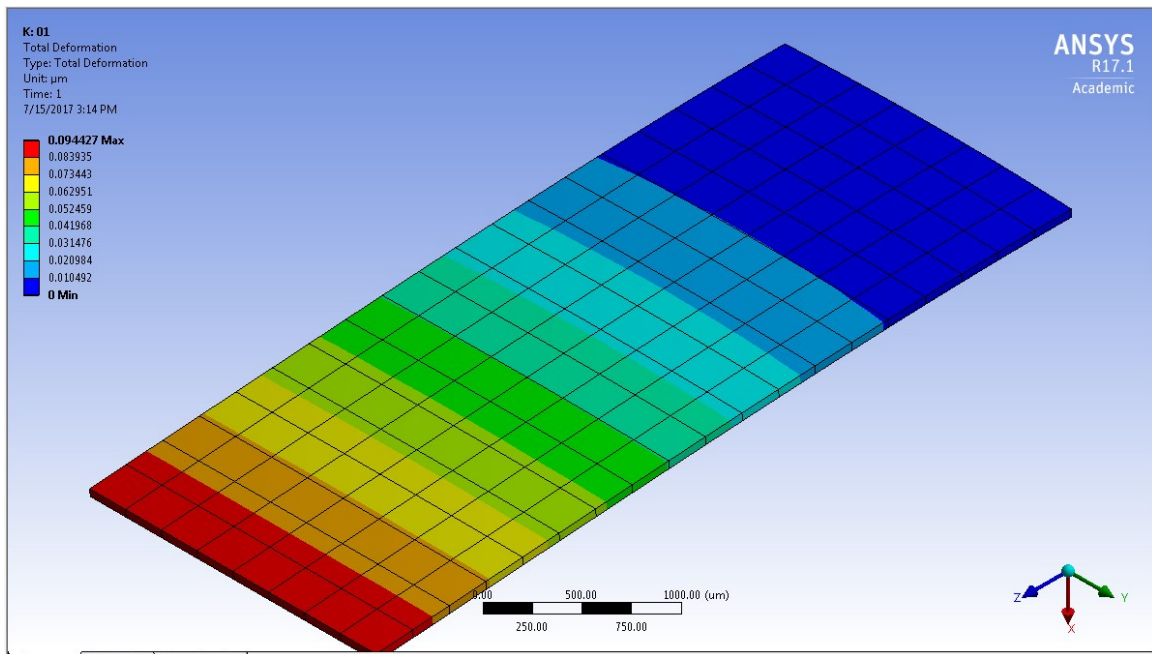


Figure 3.26. The maximum Deflection for the current case study (The maximum deflection is 0.094 μm)

Chapter 4 The Sensor

In the signal detecting phase, the cantilever platform will be used. As it was mentioned in the third chapter, this platform offers capabilities of low-cost large-production of highly sensitive fluid flow sensors for pipes of small cross section. Furthermore, the platform has the ability to minimize or even eliminate the pressure drop and flow disordering through the pipe lines, which represent the traditional issues in the flow-metering process.

As explained in the section 3.2, the dynamic pressure varies across the pipe which is also analytically proved in section 3.3.1. Furthermore, this variation of the dynamic pressure is detectable due to strain variation induced by the dynamic pressure in the small cantilevers. The numerical simulation of the current idea conceptually states the higher induced strain in higher flow value.

More accurate results are obtained by measuring the dynamic pressure at three different levels in the flow. Hence, three rectangular beams with different lengths are used. Close to the pipe wall, the beams are installed to reduce the interference of the beams with the flow. The installed strain gages on the three cantilevers were standard micro Si-strain gages, commercial Cu strain gages or printed strain gages made from conductive ink by printing.

4.1 Miniature strain gage

The idea of measuring the flow according to the dynamic pressure variation is conceptually proved in section 3.5. With regards to this method, the flow will be measured based on different induced strains on cantilever beams at various flow values. In order to convert the induced strains in the cantilever platform into a detectable and processable signal, the piezoresistive principle is applied. As it is explained in section 3.3.2, a thin layer of piezoresistive material located on the cantilever beam generates resistance variation under the imposed strain induced by the fluid flow.

4.1.1 Strain gage types

The strain gages are known as popular types of the strain detecting devices that could be installed on different surfaces. Such strain gages could be classified into two major groups: foil gage and semiconductor strain gage. The foil strain gages are the most common type and consist of the metal pattern which are supported by a flexible backing insulation part. Figure 4.1 illustrates the schematics of a foil strain gage.

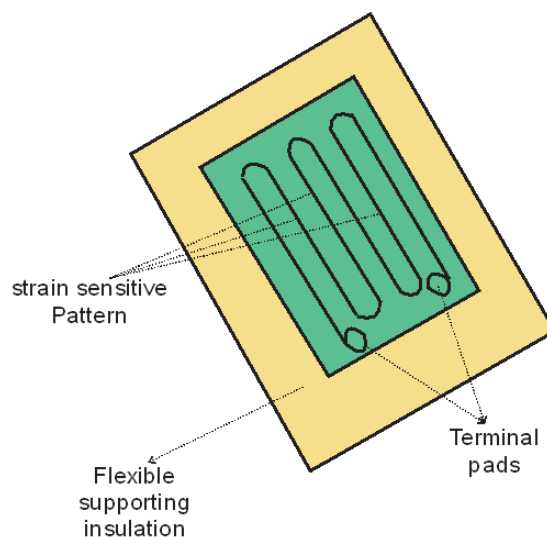


Figure 4.1. Schematic view of a foil strain gages

The electrical resistance depends on the material and the geometry of the electrical conductor. When an electrical conductor becomes narrow and longer due to stretching phenomena induced by a strain, based on the equation (4.1) the total resistance will increase. Conversely, in compressing phenomena the resistance will decrease. The resistance variation interpreted as strain changing in the strain gage.

$$R = \rho \frac{L}{A} \quad (4.1)$$

where the ρ , L and A are the electrical resistivity, length and cross-sectional area of the conductor.

In semiconductor applications, silicon shows better performances due to its higher gage factor and widely used in electric devices. Hence semiconductor strain gages are built from silicon as a piezoresistive material. The main duty of strain gages is converting the micro strains to micro volts in order to feed the generated signals to the post-processing analyzer. The strain gages have been identified by two principal characteristics, gage factor “GF” and thermal coefficient of resistance “TCR”.

The ratio of the electrical resistance to the strain, named as gage factor, which is a dimensionless number. The equation (4.2) represents the formulation of this number. Where the ΔR , R and ε are the resistance variation stems from induced strain, nominal resistance of the strain gage and induced strain to the beam, respectively.

$$GF = \frac{\Delta R}{R} \frac{1}{\varepsilon} \quad (4.2)$$

Generally, the recommended resistance range of piezoresistive strain gages, which represents high performance in strain detecting field is ranging from 120 Ω to around 700 Ω [48]. The formulation (4.2) states that by assuming a standard strain gage resistance around 350 Ω and 2 as a gage factor value, 0.001 Ω resistance variation will detect about 1.428 micro-strains.

The other important character of the strain gages is the thermal coefficient of resistance “TCR”, which is expressed by (4.3). Where the R_1 and R_2 are the resistance in the ambient temperature T_1 and elevated temperature T_2 , respectively.

$$\text{TCR} = \frac{100 (R_2 - R_1)}{R_1 (T_2 - T_1)} \quad (4.3)$$

The major issue of semiconductor strain gages is their large TCR factor, unless using the gages at a constant temperature. For instance, the TCR factor of a common commercial strain gage³ with a regular resistance value of 350 Ω is about 0.06. Therefore in a 20° temperature differences, the gage total resistance will increase to 353.5 Ω .

Generally, the gage factor of the semiconductor based gages is larger than the one on foil gages. On the other hand, they are more expensive, highly sensitive to temperature variation and more fragile than the foil gages. They are also more difficult to install.

4.1.2 Strain gage location

The strain gages are specially designed for strain detecting purposes. Therefore they should be placed at highest possible strain area in the system. Clearly, in cantilever platform sensing,

³ Micron-instrument Company. The product number “SS-095-060-350PU”

the important factor that should be defined is the highest strain area on the cantilever beam. In the experimental phase, the selected dimensions for the three cantilever beams for installing in a 4" pipe are designed, which is illustrated in figure 4.2.

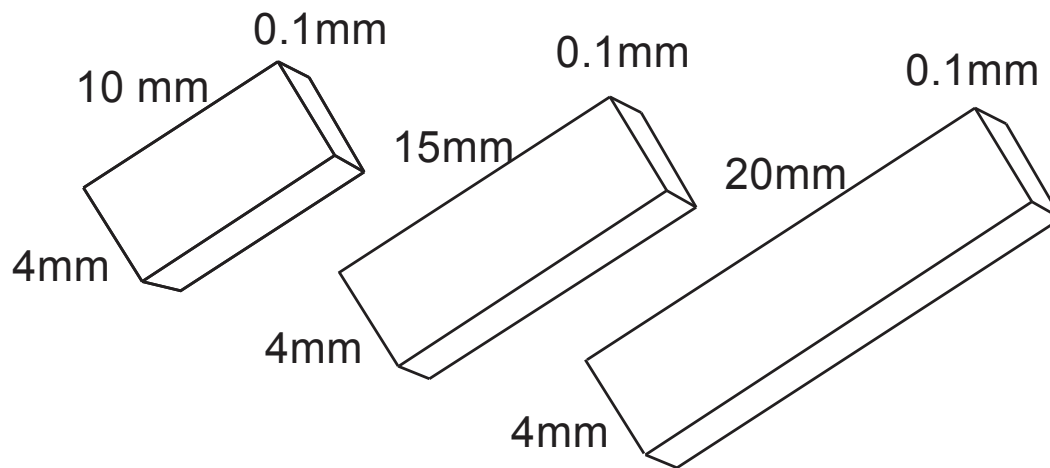


Figure 4.2. The selected dimensions for the three cantilever beams, in order to install in a 4" pipe.

The numerical analysis of these three cantilever beams under the same distributed loads and point loads are carried out by ANSYS. The figure 4.3 and 4.4, illustrates the induced strain to the 20mm length cantilever beam under the distributed load and point load, respectively.

With regards to the dimensions and defined material for the beams (Mellinex), the maximum possible strain area for the point load is approximately from fixed-end to the $\frac{L}{3}$, and for the distributed load is from fixed-end to the $\frac{L}{4}$. Thus mounting the strain gages on the $\frac{1}{3}$ length of the cantilever beam from the fixed-end, will cover highest possible strain location in point load, triangular load and uniform distributed load. Figure 4.5 illustrates the schematic view of the strain gage installing position in the experimental phase.

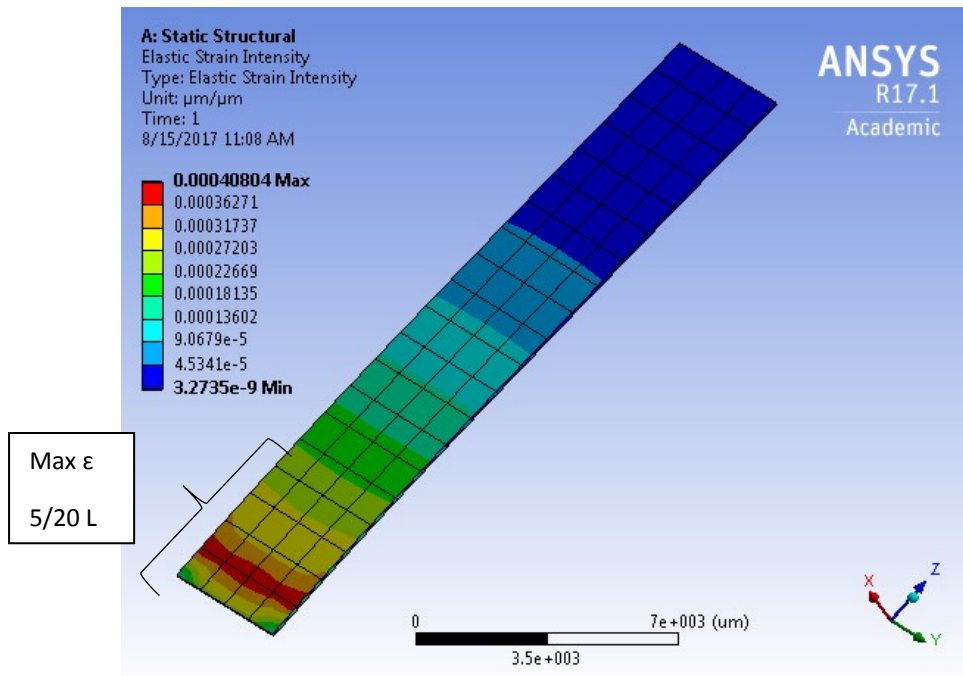


Figure 4.3. The induced strain to the 20mm cantilever beam under the 10 Pa uniform distributed load (Highest strain area $L/4$)

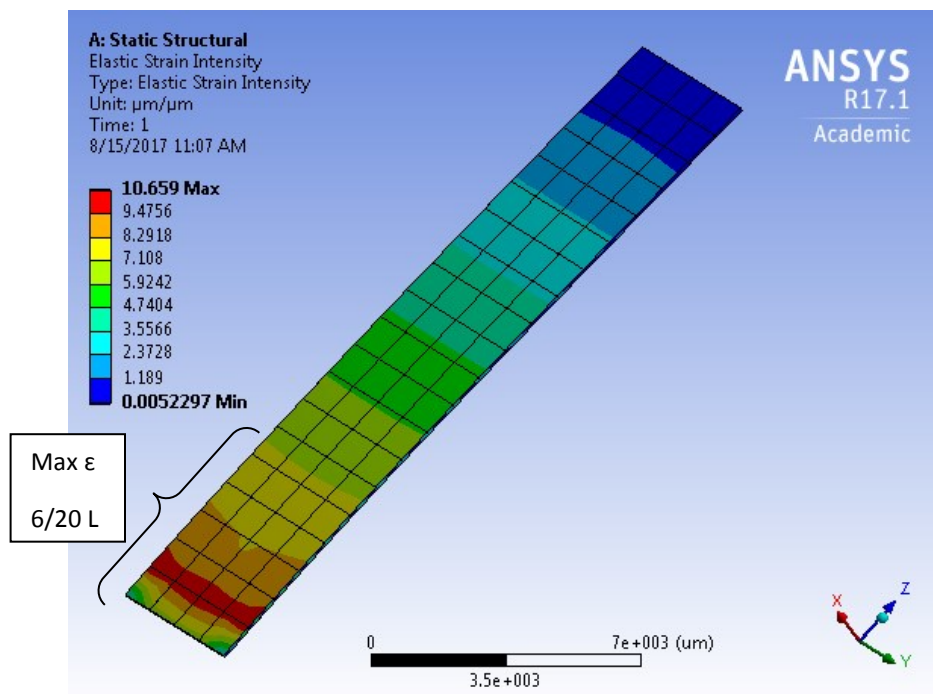


Figure 4.4. The induced strain to the 20mm cantilever beam under the 10 N point load at the free-end (Highest strain area approximately is $L/3$)



Figure 4.5. Schematic view of the strain gage installation location on the cantilever beam

4.1.3 Strain gage mounting

The accurate measurement by a strain gage strongly depends on the installation quality onto the measuring object. The most popular method to install strain gages on surfaces is adhesive bonding. The main duty of the adhesive is transferring the strain from the object to the strain gage. Measurement errors may be produced due to the adhesive delaminating from the surface of the measurement device. The complete and comprehensive transferring depends on strain gage mounting skills and selecting the proper adhesive suitable to the object.

4.1.3.1 Adhesive selection

One of the important steps of strain gage mounting process is the proper adhesive selection phase. The adhesives are categorized based on their different characteristics. The main groups are discussed in this section.

The important characteristics of the adhesives is the operational temperature, which should be considered in adhesive selecting phase. Another character of the adhesive which has a direct influence to the strain measuring is the viscosity of the adhesive. The low viscosity adhesive produces a thin layer of adhesive and more viscous adhesive produces a thick layer of adhesive.

Generally, the thin layer is recommended due to adding more distances between strain gage and object in thick layer adhesives, which generates misreading. On the other hand, thick layer adhesives are used in porous objects. For instance, in the concrete, thin adhesives are simply absorbed to the surface, therefore thick layer is desired.

In this study, few different types of adhesives are investigated such as Z70, X60, X280, EP150 and EP310S⁴. The maximum tolerable temperature for Mellinex is 100°C. Furthermore, the thin layer adhesive is desired due to less misreading is contributed on it. The X60, EP150 and EP310S require higher temperature (250°C) for strengthening and X280 is known as high viscosity (thick layer) adhesive, thus they are phased out.

The Z70 is cold-curing, single component and low-viscosity adhesive. The operational temperature is from (-55°C) to (100°C) and it is the only adhesive which is applicable and sticks to the plastic. Hence the Z70 as a fast-acting superglue is the recommended standard adhesive for experimental purposes and it was used in this study.

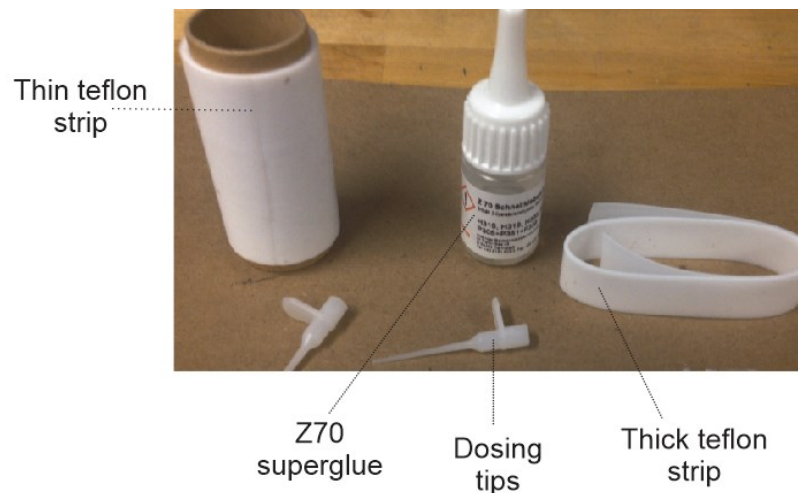


Figure 4.6. Z70 superglue and package equipment

⁴ HBM company website (www.hbm.com)

4.1.3.2 Surface preparation

One of the important aspects required to create an optimum bonding condition is preparation of the surface of the object before the installation. Briefly, the surface should be clean and rough enough to yield a strong bonding. The cleaning and roughening methods are selected based on the material which will be used. As it is mentioned one type of plastic sheet (Mellinex) will be used in this experiment.

The suggested technique for cleaning the plastic sheets is using pure-alcohol and de-ionized water. In the roughening phase, oxygen plasma and superfine sandpaper are recommended [49]. In the current thesis, the P600-sandpaper is used, which represents the average particle diameter of about 25.8 μm .

4.1.3.3 Sensor construction

Once the type of adhesive and the cleaning and roughening are selected, the installation of the strain gauge it follows. In this investigation two types of strain gages are investigated, namely foil and semiconductor strain gauges. As it is explained in section 4.1.1, semiconductor strain gauges have higher gage factor in comparison with foil gages thus they illustrate higher resistance differences over same bending condition.

On the other hand, one of the weak points of semiconductor strain gages is their higher TCR number, which shows more sensitivity to temperature variation. Moreover, these types of strain gages are highly fragile. Their installation requires equipped laboratory and a great deal of small objects handling skills are required. Ultimately we used conventional foil gage and not silicon based one. There have been attempts in Si-based but were not successful.

Figure 4.7 illustrates the size comparison between a semiconductor strain gage and a foil strain gage. The length and width of the foil gage are 7 mm and 4mm, respectively. The width and length of the miniature size semiconductor strain gage are 0.5mm and 1.5mm, respectively.

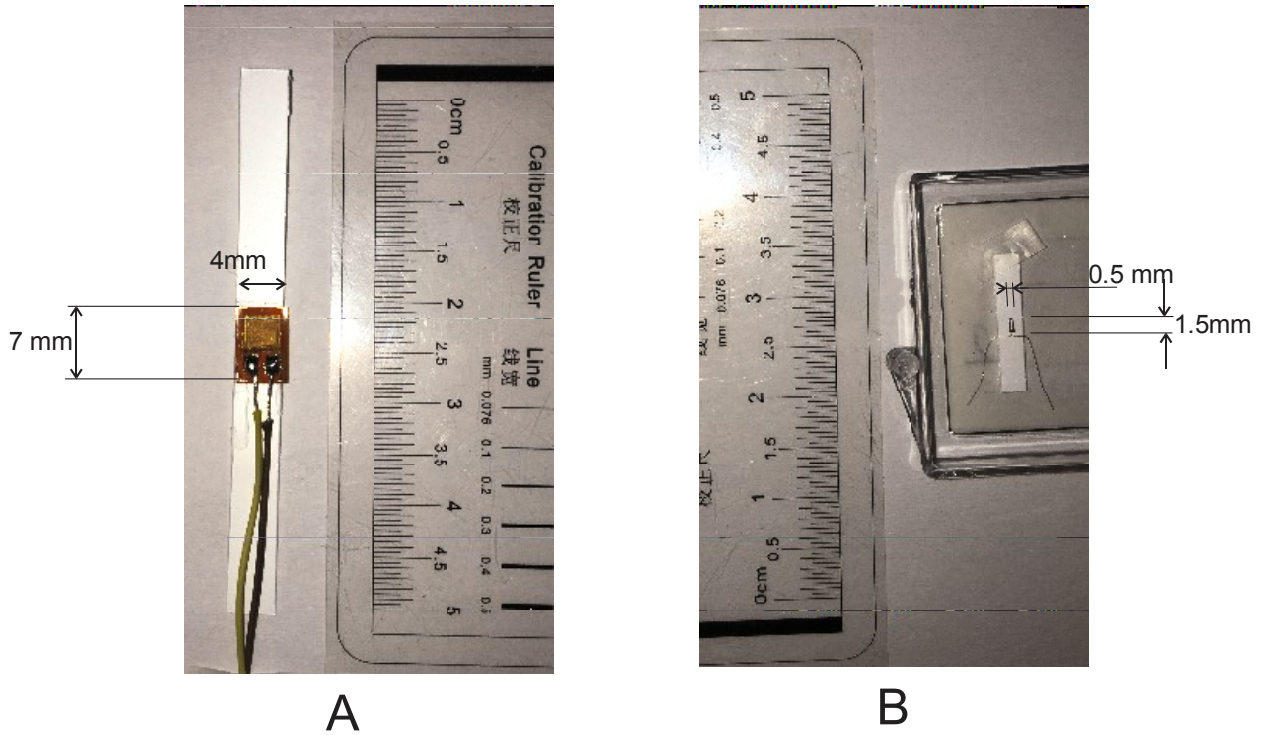


Figure 4.7. Two mounted strain gages A) The foil gage with 350 Ω resistance
B) The miniature size semiconductor strain gage with 520 Ω resistance.

The rectangular beams are designed using Solidworks software and the file is further imported to a cutting machine by “DXF” format. In order to fit the size to the both of strain gages, the strips of the Mellinex are cut into 2 and 4-millimeter width. Further, the cleaning and roughening process are applied to the strips according to the section 4.1.3.2.

As it is explained in section 4.1.2, the strain gage positioning has a strong influence to the strain measurement sensitivity. The strain gages are installed in the center of the polyester

strips and then according to the figure 4.5, the strips are cut to satisfy the optimal position for the strain gage for maximum sensitivity detection.

First, a tiny droplet of superglue will be delivered to the cantilever beam. The drop will be smeared with a Teflon strip. Another Teflon strip will use for applying a uniform thumb pressure to the strain gage for around 5 minutes. The Z70 will completely cure after 24 hours in the room temperature.

The next phase in sensor construction process is soldering the two wires to the connection pads of the strain gage. As it is mentioned before, the maximum tolerable temperature for Mellinex is around 100° C, thus it will be damaged in soldering process. Therefore the wires are soldered to the strain gages before mounting to the plastic beams. In strain gage sensing field the recommended wire type is the low-resistance multi-wires, which it was used in this project. Figure 4.7 illustrates the soldered and mounted foil strain gage.



Figure 4.8. Mounted foil strain gage on Mellinex with the soldered wires to the pads

The constructed sensors is installed in the pipe. For this reason, the illustrated holding pads design in figure 4.8, is carried out by Solidworks and imported to the Robox 3D-printer. Several male and female half-cylinders holding pads are printed. In the next step, the sensor beams are glued to the designed groove of female half-cylinder of one pair. The male part will glue to the female one by epoxy glue. The epoxy glue will fill the empty space between half-cylinders and will cure in a day.

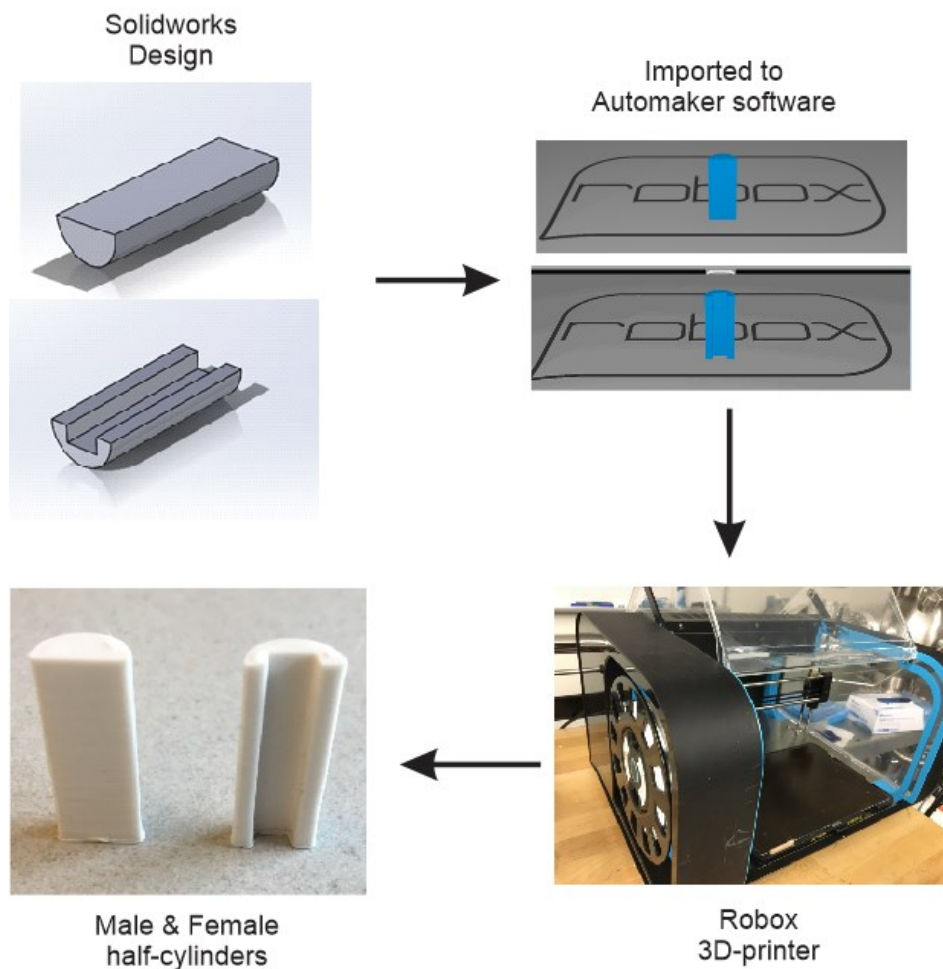


Figure 4.9. The half-cylinders manufacturing process

The constructed sensors will insert to the three radial holes on a piece of pipe, which these holes spaced at 120° as illustrated in figure 4.9. The selected length for the cantilever beams are 10mm, 15mm and 20mm.

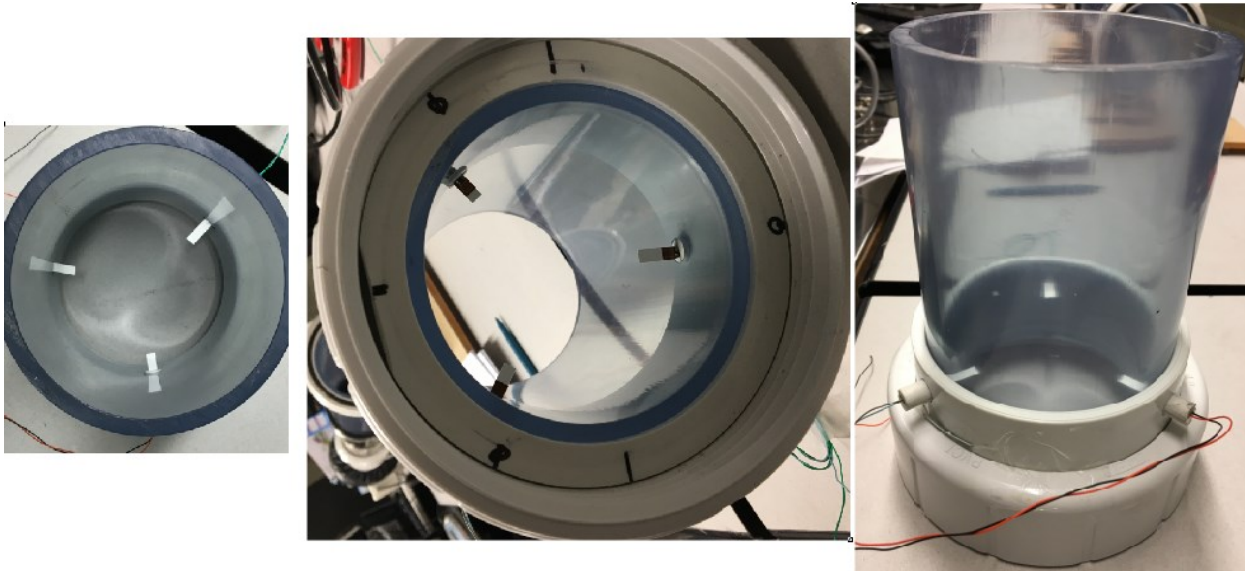


Figure 4.10. The installed sensors in the segment of pipe

4.2 Sensor measurement

Although the investigations were directed towards instrumenting smaller beams using Si strain gauges, the attempt was not successful due to the difficulty to precisely manipulate small and fragile components. Hence, foil gages are used in this research.

Resistance comparing bridges such as Wheatstone bridge, generates electrical output signals from the physical variables they follow (section 2.1.2.2). The generated signals are significantly small therefore high amplification is required to bring them to a readable range.

On the other hand, the amplifier should be equipped with a filter for removing the stray noise produced in the circuit. There are several noise sources such as unsteady wiring or variations in

the contact resistances or noise produced by the quality of soldering, etc.[50]. Figure 4.11 illustrates the basic block diagram of the measurement process. Once the signal is filtered and amplified it should be monitored. An indicator is installed after filtering and amplification.

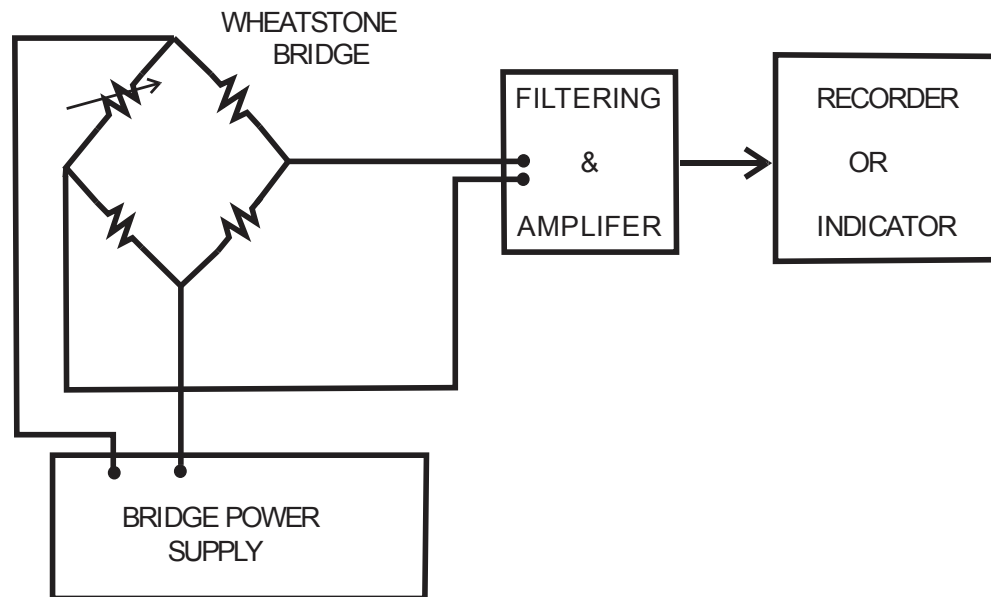


Figure 4.11. Basic Wheatstone bridge- base measurement block diagram

4.2.1 Wheatstone bridge construction

The Wheatstone bridge is the most popular resistance-bridge configuration. In this bridge at least one of four resistances is variable. Another example of use of the Wheatstone bridge is the hot-wire technique which is illustrated in figure 2.7. According to figure 4.11, the constant voltage or current will excite the bridge to produce the electrical signals. As it is discussed in the section 2.1.2.2, in the bridge-balance requires the ratio (R_1/R_2) as equal to (R_g/R_3) , where the R_g is the resistance of strain gage.

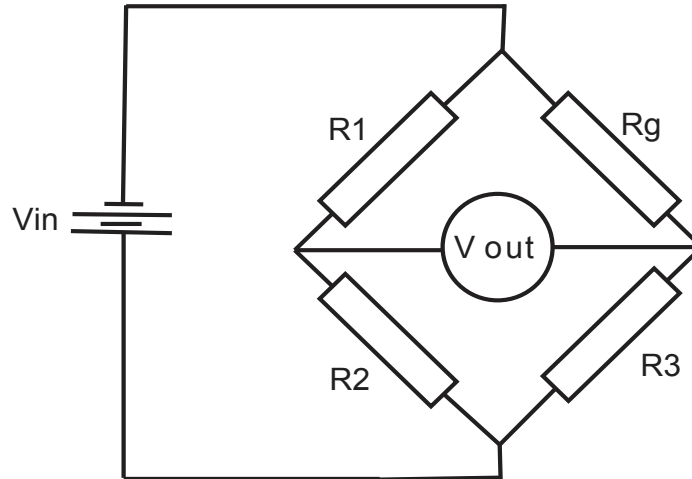


Figure 4.12. Wheatstone bridge with single element varying

In the current investigation all three bridge-completion resistors have the same resistance value (350 Ω). The connection configuration in Figure 4.12 is achieved. Hence, the output voltage of the bridge according to the equation (2.11) will transform to equation (4.4).

$$V_o = \frac{V_{in}}{4} \left[\frac{\Delta R}{R + \frac{\Delta R}{2}} \right] \quad (4.4)$$

One of the important factors, which has direct influence on measurement accuracy is TCR value. In this project, the bridge completion resistors in Wheatstone bridge circuit board, are selected from the same type of strain gages in order to minimize the negative effect of the temperature on measurement. All strain gauges are installed close to the flow such that all gather same temperature variations as the fluid. The above approach represents a standard procedure to compensate for temperature variations during measurement.

4.2.2 Filtering and amplification

The signal generated from Wheatstone bridge is subjected to noise and small amplitude. Thus filtering and amplification is required for solving these initial issues. Generally, in bridge-base measurement systems such as pressure sensors the amplifier part is responsible for amplifying and filtering of output signals. This amplifier consists of a circuit board of several amplifiers.

In addition to amplification and filtering phase, the output signal is monitored for feeding the data to the post-processing phase. The Phidget-Bridge (figure 4.13) as a commercial circuit board will cover all these requirements. This interface board is connectable to 4 un-amplified Wheatstone bridges which are constructed from strain gages. The board is designed to measure the ratio of the output signals to the supply voltage.



Figure 4.13. The Phidget-Bridge interface board

Also, the board includes a USB-port for communicating with the computer. The Phidget-Bridge as a programmable board is supporting different programming languages such as C#,

C++, Java and etc. In the current study one pressure sensor software which is written in C# will be used for communication of the PC with the Phidget-Bridge.

The figure 4.14 illustrates the interface window of the software. The gain values and data rate of the board are controlled by the software. One can preset the gain values to 1, 8,16,32,64 or 128. Generally higher gain values yields higher noise and higher resolution. Also, the data acquisition rate is adjustable from 8ms to 1000ms in increments of 8ms.

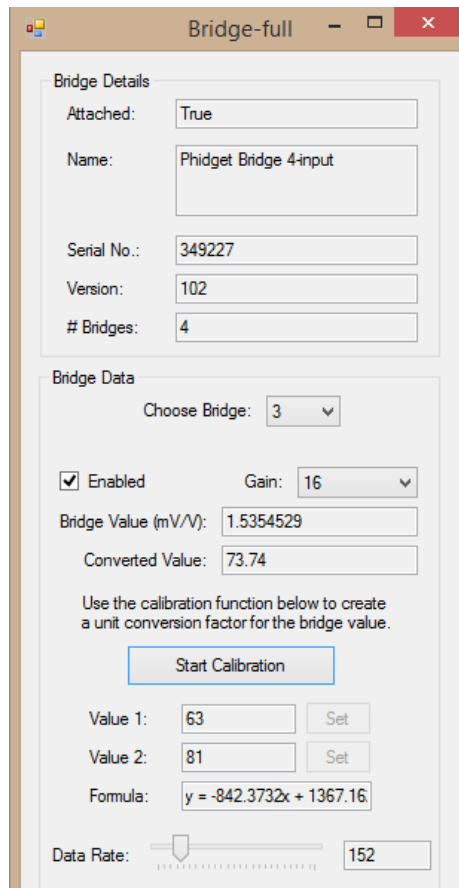


Figure 4.14. The communicating window of software with Phidget-Bridge

Each of the four terminals on Phidget-Bridge includes 4 ports, where 2 ports (5V & G) are assigned to provide the required voltage for activation of the Wheatstone-Bridge. The two other ports (+ and -) are assigned for the output signals from Wheatstone bridge. The figure 4.15 shows the physical Wheatstone bridge with the strain gages and the connection to a Phidget-Bridge.

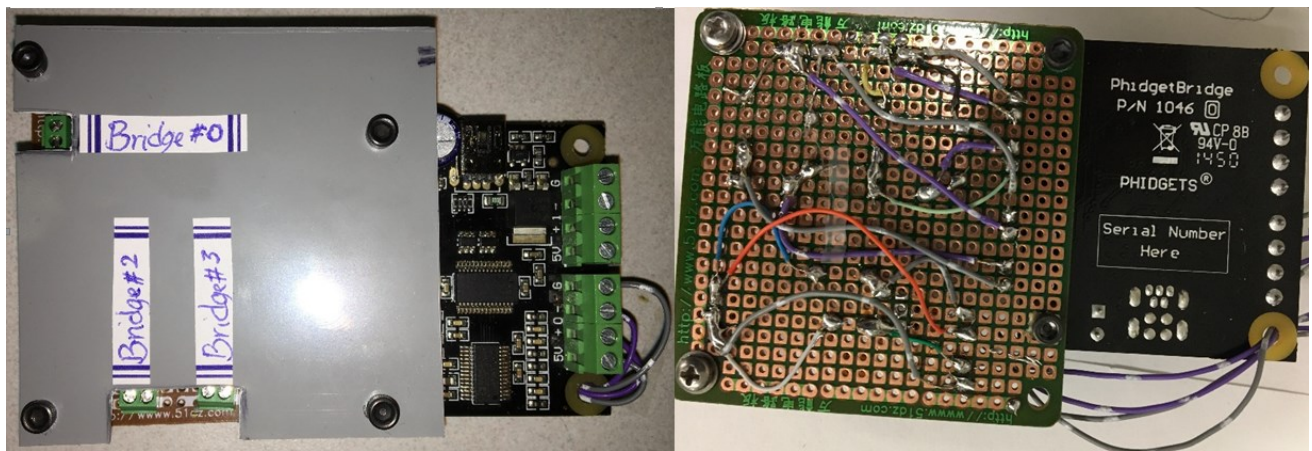


Figure 4.15. The constructed Wheatstone bridge board along with the Phidget-Bridge

The configuration of the bridge-board consists of three Wheatstone bridges and three terminals. Each Wheatstone bridge includes three same strain gages, which will complete by connecting the 4th one through designed terminals. The required excitation voltage for Wheatstone bridge comes from the 5V and G ports of the Phidget-Bridge. The USB-port ensures the power for Phidget-Bridge.

4.3 The experimental set-up and the results

As it was mentioned in chapter 3, due to limitations in the available equipment in the university laboratory, air was used as flow fluid instead of water. In order to generate different

flowrates in pipe-line, a 4" fan along with a regulator were used. The connecting piping system to the fan consists of 4" PVC pipes, which their connections are properly sealed by suitable adhesive as shown in figure 4.16.

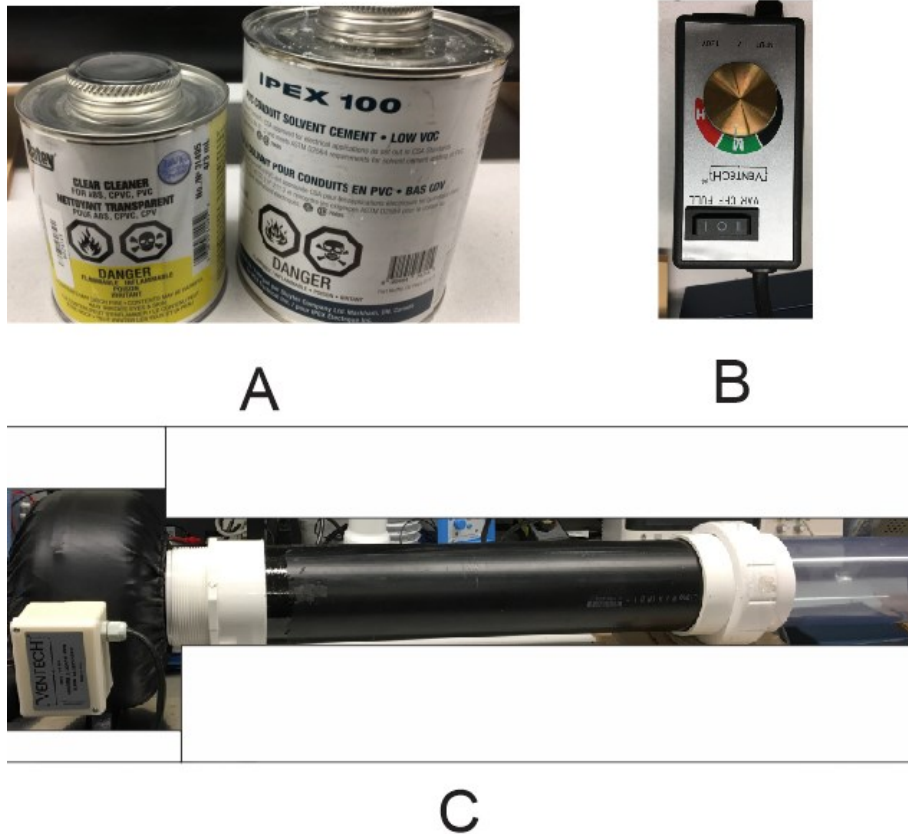


Figure 4.16. A) PVC pipe adhesive. B) Regulator. C) Connected fan to the pipe-line

As previously discussed in section 3.2, it is strongly recommended to install the sensors within the 14D distance far from the inlet of the pipe. Thus the sensor part (figure 4.9) is installed around 142cm far from the fan. In order to provide uniform flow at the entrance of the pipe, the fan is installed to induce vacuum. The figure 4.17 illustrates the complete experiment set-up configuration. One well-known commercial flow meter, namely “REED” is also installed in the pipe for accurate measurement of the flow within the flow system.

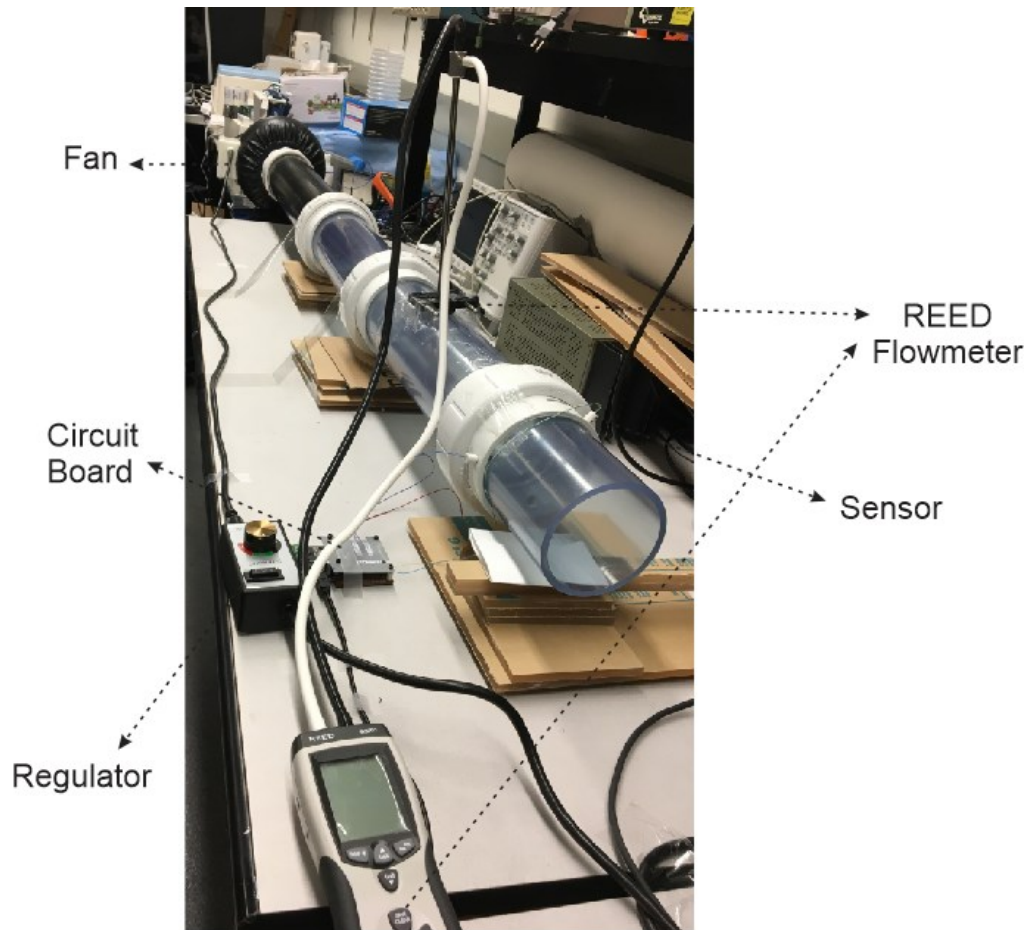


Figure 4.17. The entire set-up of experiment

Then the sensor wires are connected to the three terminals of the Wheatstone board as illustrated in figure 4.18. The maximum accuracy in measurement will occur when all connection wires are same length and gauge number. The temperature variation might sensitively change the resistance of the wires but if they exhibit same variation, the errors will be eliminated.

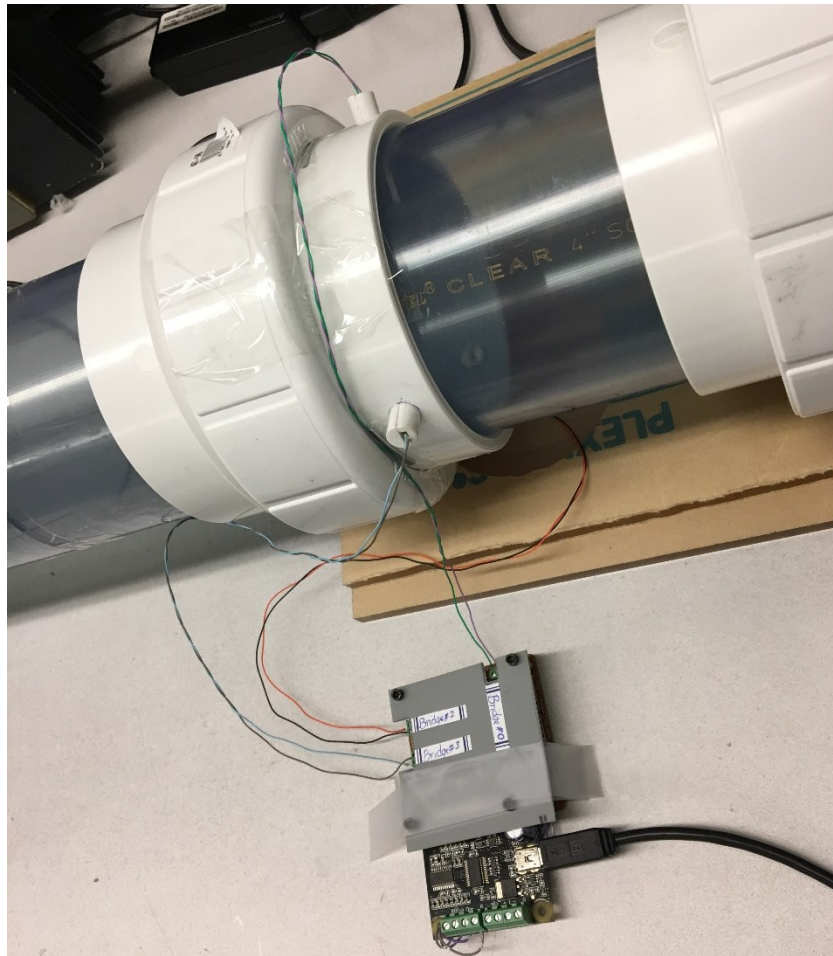


Figure 4.18. The wires from the sensor are connected to the Wheatstone bridge

Once the Phidget-Bridge software is installed on the computer and the board is connected by the USB cable to the computer, the Phidget will be recognized as illustrated in figure 4.19. In the current study the gain factor and data rate set to the 16 and 160, respectively. Two procedures of flow measurement methods will be described below and they include both the non-linear and the linear approach.

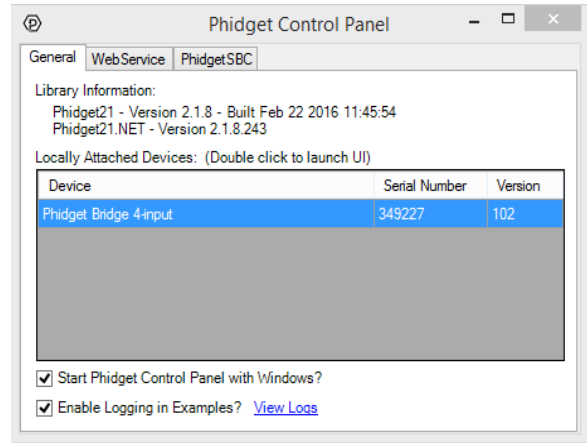
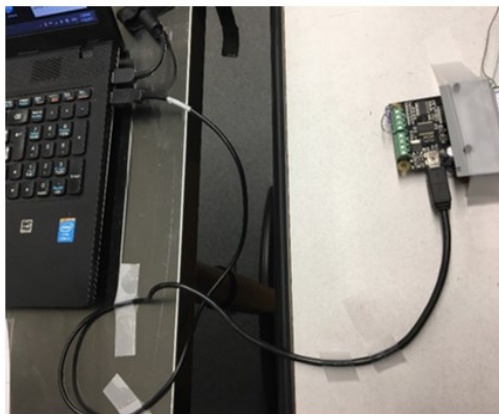


Figure 4.19. The USB cable connected and recognized by the computer

4.3.1 Triple sensor non-linear measurement

As it was discussed in section 2.2, the dynamic pressure variation in the cross-section of the pipe is proportional to the velocity variation across the pipe. Theoretically, the idea is to find the values of the dynamic pressure at three different points in half cross section of the pipe. The three measurements are used to finding the velocity profile by fitting a parabolic curve passing through these control points. In fact, the flow value is computable by integrating the velocity profile in the area of the cross-section of the pipe.

In the experimental approach at the same flow value condition three different signals “S1, S2, S3” are collected from 10mm, 15mm and 20mm sensors, respectively. Figure 4.20 illustrates the configuration of the measurement. The parabolic velocity profile for this configuration is given by (4.5). Here y is the distance of the measured position from the wall of the pipe and x represents the measured value at that point.

$$x = a y^2 + b y + c \quad (4.5)$$

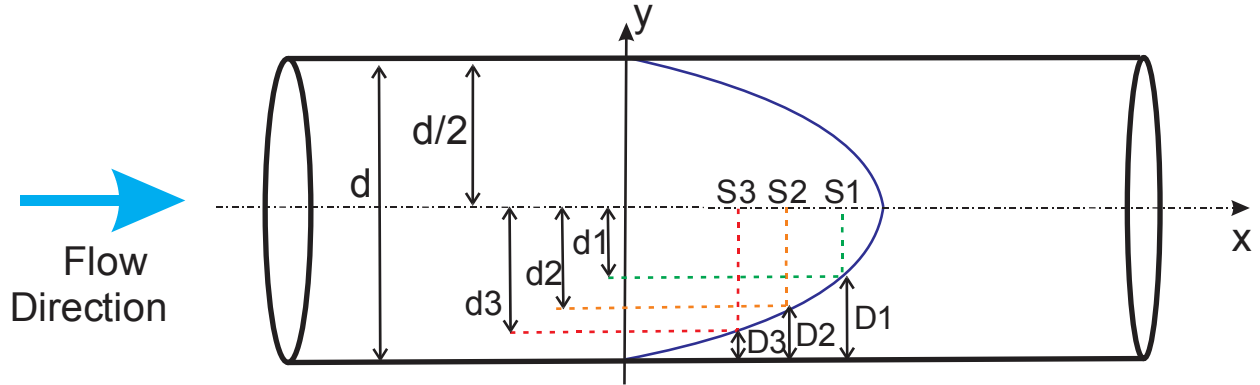


Figure 4.20. Configuration of the measurement in experimental phase

According to the figure 4.20, the position of every point on the parabolic profile in the y-axis is known as the gage distance from the wall “ D_i ” and is given by (4.6). The D_1 , D_2 and D_3 are distances of the gages from the wall of the pipe. Based on the (4.9) the three equations for three different sensors are shown in (4.7). Where the a , b and c are the coefficients of the parabolic profile.

$$D_i = \frac{d}{2} - d_i \quad (4.6)$$

$$\begin{cases} S_1 = a D_1^2 + b D_1 + c \\ S_2 = a D_2^2 + b D_2 + c \\ S_3 = a D_3^2 + b D_3 + c \end{cases} \quad (4.7)$$

Thus the coefficients of the parabolic profile are given by:

$$\begin{bmatrix} \mathbf{a} \\ \mathbf{b} \\ \mathbf{c} \end{bmatrix} = \begin{bmatrix} \mathbf{D}_1^2 & \mathbf{D}_1 & 1 \\ \mathbf{D}_2^2 & \mathbf{D}_2 & 1 \\ \mathbf{D}_3^2 & \mathbf{D}_3 & 1 \end{bmatrix}^{-1} \begin{bmatrix} \mathbf{S}_1 \\ \mathbf{S}_2 \\ \mathbf{S}_3 \end{bmatrix} \quad (4.8)$$

The area under the parabolic curve is computed by integrating the (4.5) across the half of the pipe (4.9) and named as “Z”. Where the term d is the diameter of the pipe, which is 101.6mm (4”) in this study.

$$|\mathbf{Z}| = \int_{-\frac{d}{2}}^0 (\mathbf{a} x^2 + \mathbf{b} x + \mathbf{c}) dx = \left. \frac{\mathbf{a} x^3}{3} + \frac{\mathbf{b} x^2}{2} + \mathbf{c} x \right|_{-\frac{d}{2}}^0 \quad (4.9)$$

The term Z is proportional to the real flow value “Q_{REAL}” due to the axi-symmetric nature of the flow phenomena as illustrated in figure 4.21. This relationship is shown in (4.10), where the K-coefficient is known as the correction factor for the considered sensor.

$$\frac{\mathbf{Z}}{\mathbf{Q}_{\text{REAL}}} = \mathbf{K} \quad (4.10)$$

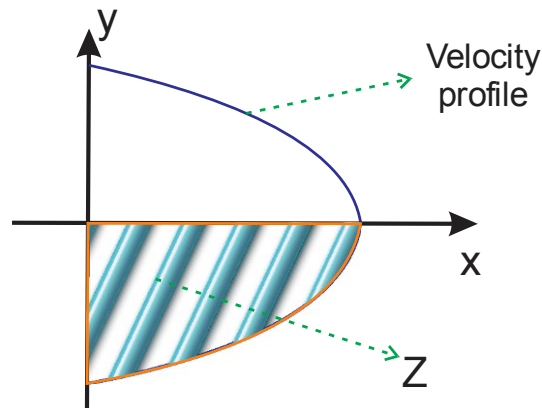


Figure 4.21. The area under the half parabolic velocity profile is named as Z which value is proportional to the flow by K-correction factor

The K correction factor is one of the important characteristics of the flow-measuring device. It should be defined correctly and be validated in different flow-values with acceptable error percentages. In the current study, the fan speed-regulator provides different flow values. Then the measured signals from the three sensors are used for drawing the graph 4.22.

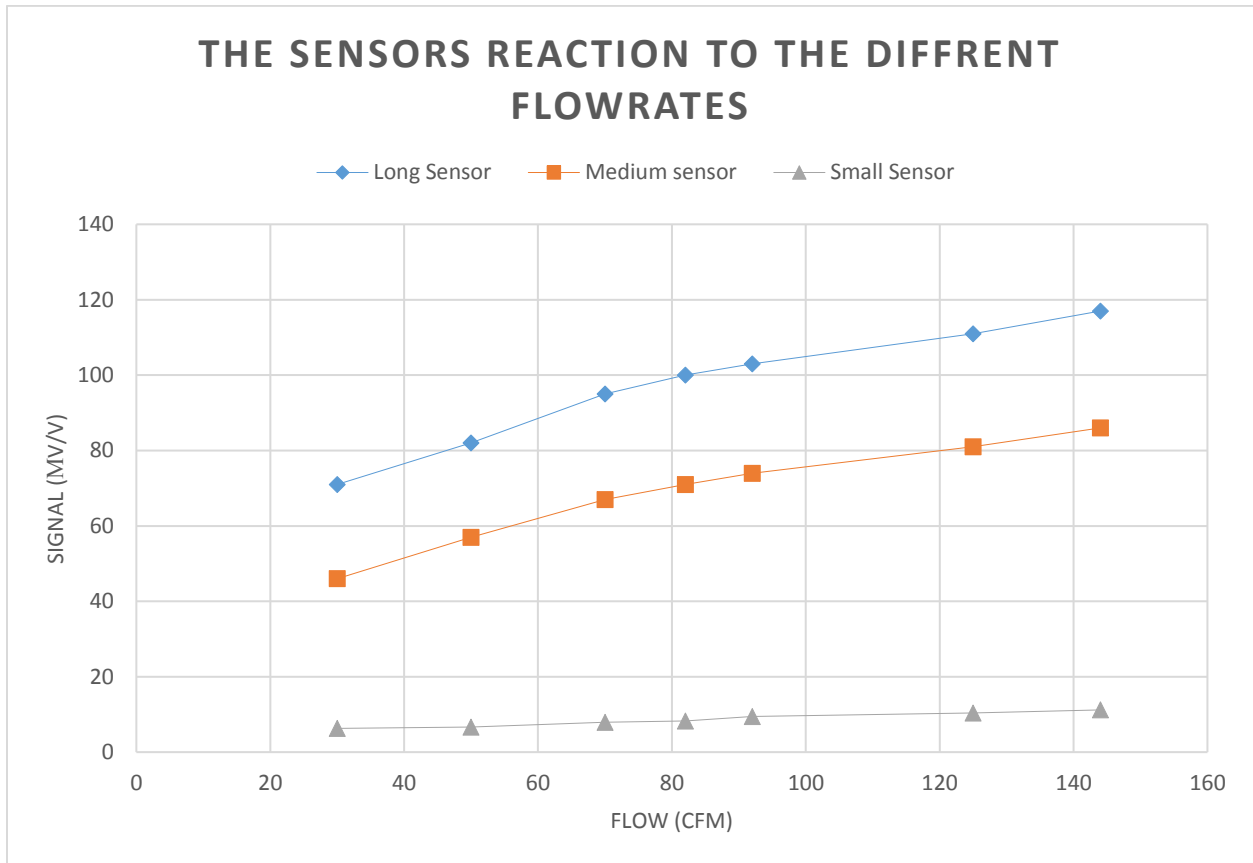


Figure 4.22. The measured signals from sensors in different flowrates

At every flow condition, the (4.9) is used for finding the Z-area. The Q_{REAL} comes from REED flow-meter reading. A K-conversion factor will be computed by comparing the Q_{REAL} and Z values based on the (4.10). For instance in “ $Q_{REAL}= 70$ CFM”, the measured signals S1, S2 and S3 are 95, 67 and 7.9 (mv/v). According to the equations (4.6) and (4.7), the below relationships are obtained.

$$\begin{cases} D_1 = \frac{d}{2} - d_1 \\ D_2 = \frac{d}{2} - d_2 \\ D_3 = \frac{d}{2} - d_3 \end{cases} = \begin{cases} D_1 = \frac{101.6}{2} - 20 \\ D_2 = \frac{101.6}{2} - 15 \\ D_3 = \frac{101.6}{2} - 10 \end{cases} = \begin{cases} D_1 = 30.8 \\ D_2 = 35.8 \\ D_3 = 40.8 \end{cases} \quad (4.11)$$

$$\begin{cases} S_1 = a D_1^2 + b D_1 + c \\ S_2 = a D_2^2 + b D_2 + c \\ S_3 = a D_3^2 + b D_3 + c \end{cases} \Rightarrow \begin{cases} 95 = a (30.8)^2 + b (30.8) + c \\ 67 = a (35.8)^2 + b (35.8) + c \\ 7.9 = a (40.8)^2 + b (40.8) + c \end{cases} \quad (4.12)$$

Therefore the parabolic velocity profile coefficient “a, b, c” based on the (4.7) is given by:

$$\begin{bmatrix} a \\ b \\ c \end{bmatrix} = \begin{bmatrix} 30.8^2 & 30.8 & 1 \\ 35.8^2 & 35.8 & 1 \\ 40.8^2 & 40.8 & 1 \end{bmatrix}^{-1} \begin{bmatrix} 95 \\ 67 \\ 7.9 \end{bmatrix} \Rightarrow \begin{bmatrix} a \\ b \\ c \end{bmatrix} = \begin{bmatrix} -0.6215 \\ 35.7871 \\ -417.6607 \end{bmatrix} \quad (4.13)$$

According to the equation (4.9), the Z area is:

$$|Z| = \int_{-\frac{d}{2}}^0 (a x^2 + b x + c) dx = \quad (4.14)$$

$$\frac{(-0.6215) x^3}{3} + \frac{(35.7871)x^2}{2} + (-417.6607)x \Big|_{-\frac{d}{2}}^0 = 2200.7$$

Thus based on the (4.10), the K-coefficient is computable.

$$K = \frac{Z}{Q_{\text{REAL}}} = \frac{2200.7}{70} = 31.4385 \quad (4.15)$$

Table 4.1 demonstrates the K-conversion factor for seven different flow values. The K-coefficient is varying from 28.57 to 32.07. Thus the average value of K, which is approximately

equal to 30.3 is considered as the conversion factor of the specific used flow-meter. The predicted value is achieved by substituting the “K=30.3” in (4.10). In the last column of the table the error percentage of the predicted value and real flow value “Q_{REAL}” is illustrated, which proves that the readings yield values of flow within in the acceptable error range.

Table 4.1. Comparison the error percentage between real value and predicted value by individual K value for the constructed sensor “K=30.3”.

Flow Value "CFM" (Q _{REAL})	K-correction Coefficient	Predicted Flow Value by K=30.3	Error %
30	31.03	30.73	2.4
50	28.57	47.15	5.6
70	31.43	72.63	3.7
82	31.80	86.06	4.9
92	32.07	97.39	5.8
125	31.15	128.51	2.8
144	30.66	145.72	1.2

4.3.2 Alternative linear single sensor approach

In this technique, the flow will be predicted by only one sensor and two calibration flow values. At first, two known flows will be used for system calibration then a linear approach will be applied for finding a relationship between two calibration flows. The equation (4.16) shows the linear relationship between the flow “Q” and the induced voltage to the sensor “S”. Here, a and b are the coefficients of the equation, which will be further found.

$$Q = aS + b \quad (4.16)$$

According to the (4.16) in two different flows, two different signals are generated in the sensor which are noted as S1 and S2. Thus the coefficients of the (4.16) are given by (4.18).

$$\begin{cases} Q_1 = a S_1 + b \\ Q_2 = a S_2 + b \end{cases} \quad (4.17)$$

$$\begin{bmatrix} Q_1 \\ Q_2 \end{bmatrix} = \begin{bmatrix} S_1 & 1 \\ S_2 & 1 \end{bmatrix} \begin{bmatrix} a \\ b \end{bmatrix} \Rightarrow \begin{bmatrix} a \\ b \end{bmatrix} = \begin{bmatrix} S_1 & 1 \\ S_2 & 1 \end{bmatrix}^{-1} \begin{bmatrix} Q_1 \\ Q_2 \end{bmatrix} \quad (4.18)$$

The principle of the Phidget-Bridge software for the predicting the flow value is based on the equation (4.16). For instance, in the figure 4.23, only the longest sensor which is connected to the bridge number 2, is used for flow measurement. This sensor due to its larger area shows higher sensitivity. The calibration points for this example are 57CFM and 74CFM and the induced signal to the sensors are 0.539 (mV/V) and 0.579 (mV/V), respectively. The assigned linear equation for these calibration points is given in (4.19).

$$y = 421.6008 x - 170.254 \quad (4.19)$$

In unknown flow condition the predicted flow value is 66.37CFM⁵, which is indicated in figure 4.23. On the other hand, the measured flow by REED at the same time is 64.284. These two values show approximately 3% differences between two flow-metering devices.

⁵ This value is also available by substituting the Bridge Value "0.5612522" to the equation (4.19).



A



B

Figure 4.23. Bridge # 2 is calibrated. A) Calibrated in 74 and 57 CFM. "Converted value = 66.37", B) Measured value by REED flow-meter "64.284 CFM"

Chapter 5 The Conductive Ink Printed Sensor

As it was presented in Chapter 4, tiny strain gage mounting on different substrates includes complex preparing phase. Moreover, due to the strain gage duty for detecting small strain values, the gauge should be located in an accurate position which in conjunction with selection of the substrate makes the procedure quite difficult. Hence, printed piezo-resistive resistors have been considered, as they have the capability to overcome to both of these issues.

Ability to print piezo-resistive resistor as a strain gage, directly on the substrate, depends on different types of parameters. Obviously, conductive ink properties, viscosity and particle sizes play major roles in this direct printing. Furthermore, printing technology should be selected based on ink properties and on the set of objectives. Inkjet printing technology as a low-cost process is widely used on flexible printed circuit board applications [51]. Hence printing of conductive materials will be used in this study. In current research the gage factor “GF” of the inkjet-printed resistors is introduced, which has not been so far investigated.

5.1 Inkjet printing

There have been proposed various types of printing such as screen printing [52], contact printing [53], aerosol printing [54-56] and transfer printing [57] for depositing conductive inks on various substrates. However, inkjet printing offers specific benefits in comparison with other techniques. Prefabrication process on substrate is the first and primary phase in every printing process but inkjet printing does not require this phase. Hence, low cost printing is enabled by this method.

Moreover, multiple materials could be deposited on different substrates by using simultaneously multiple cartridges containing various inks. Due to nozzle diameter and droplet size controlling, the amount of deposited conductive ink is controllable with relatively high precision thus, post-trimming steps are not required. Furthermore, based on inkjet printing technology nature, it is possible to print multiple layers, one on the top of the other [58]. Inkjet printing also is used to deposit other type of conductive material such as gold [59, 60] and silver inks [61, 62]. The designed pattern of the piezo-resistive gauge will be precisely printed in the desired position without post printing steps or any other post-processing, which demonstrates the valuable advantages of this method.

As it is explained in chapter 4, one of the important characteristics of a strain gage is gage factor "GF". It is defined as the ratio of the electrical resistance to the strain. Strain gages are widely used for detecting the mechanical deformation of a structure. Metallic base strain gages have gage factor around 2, while gage factor of single crystal silicon is around 200 [63]. The idea in the current study is the possibility of getting at least same gage factor as for the metal.

The inkjet printers are categorized based on the type of printing technology that they use. There are two main categories of inkjet technology: “continuous” & “drop-on-demand”. The continuous technology provides continuous stream of droplets. The droplets flow will charge according to the image signal, after leaving the nozzle. The un-charged droplets are projected onto the substrate, while the charged ones are deflected by the electric flux and will follow recycling path to the gutter [64]. The schematics of this process is illustrated in figure 5.1.

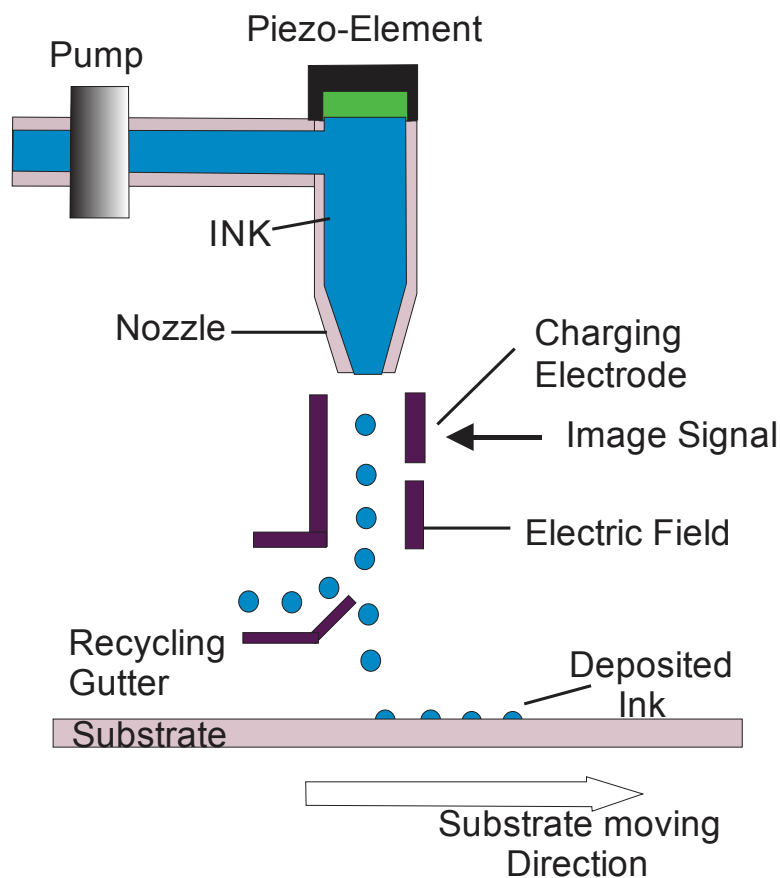


Figure 5.1. Continuous inkjet printing process (Adapted from [64])

The other inkjet printing technique is called drop-on-demand. As suggested by its name, the droplets only eject when it is commanded to do so. In this method, the continuous ejecting ink from nozzle is eliminated. The drop-on-demand may be provided by two means: piezoelectric

and thermal, which methods are illustrated in figure 5.2. The thermal inkjet printing consists of a thin film resistor integrated in the nozzle.

By passing voltage through the resistor, a heat spike is created. This heat causes water in the ink to vaporize inside the nozzle. This condition will create bubble stemmed from vaporization induces pressure to push ink droplets out of the nozzle. Some well-known printer brands such as Canon and Lexmark are using the thermal inkjet printing technology.

The other inkjet printer manufacturers such as Epson and Fujifilm Dimatix, are using piezo-electric technology. Hence, one piezo-electric actuator is located inside the nozzle. The actuator experiences deflection when a voltage is applied on the piezo-electric actuator. The deflection produces a pressure which forces out a droplet from the nozzle.

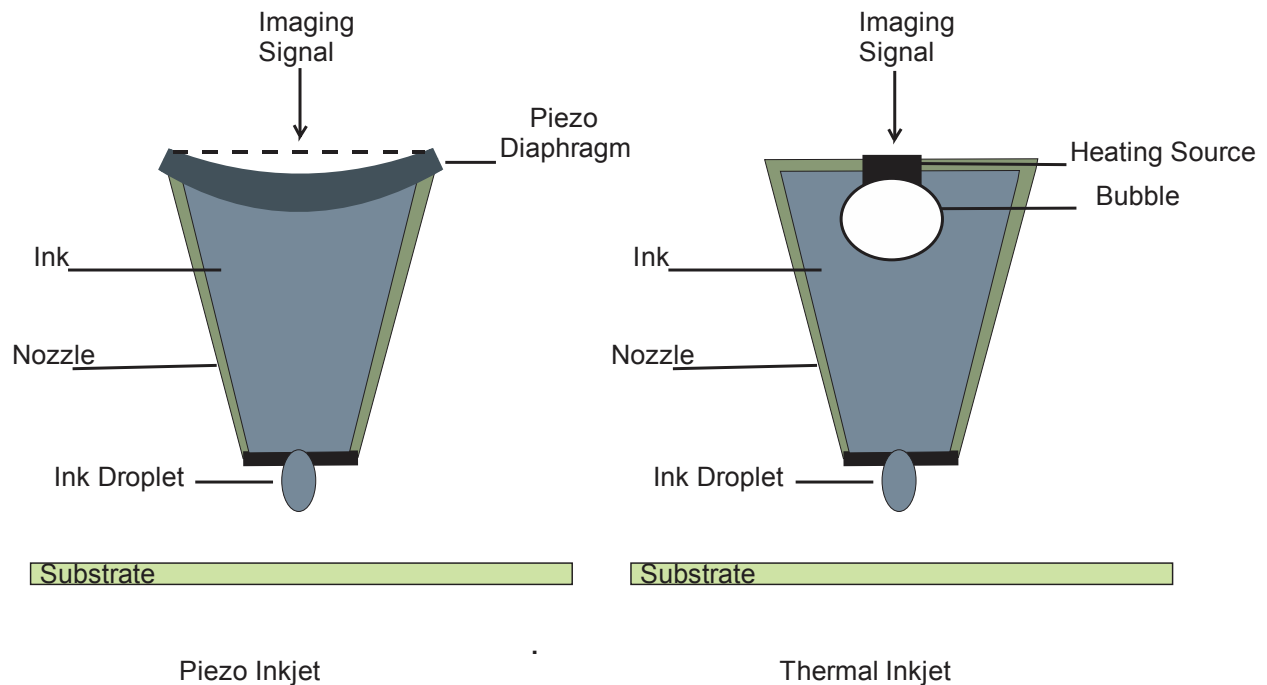


Figure 5.2. Drop-on-demand Inkjet printing Technology " Piezo & Thermal"

5.2 Color forming process

The color printing forms with small dots of ink on the substrate which configured in a certain pattern will yield the desired color. The generated pressure inside the nozzle induces the force for ejecting and depositing the selected color of ink droplets onto the desired position on substrates. The three basic colors are “Red, Green and Blue”. The other three principal colors are “Magenta, Cyan and Yellow”, which are known as the secondary colors. This arrangement enables deposition of different inks with different conductive properties. Basically, wide spectrum of colors can be made by mixing three different secondary colors as illustrated in figure 5.3. The color quality on printed area depends on the size of the dots and the amount of ink for each color. As an example, a saturated red produces by printing same amount of magenta and yellow ink onto the substrate. This type of color mixing is known as subtractive color mixing.

In subtractive color mixing devices such as ink-jet printers, one individual color is visible, when every different colors absorb (subtract) one individual color of light, so ultimately one special resulting color only will be perceived. Thus the purple, green and red colors will create by overlapping the Cyan, Magenta and Yellow ink. It means that for printing black area, same amount of all three principal colors are required for absorbing the entire color range and would not allow to reflect any light of colors. Traditionally the black ink cartridges are included in most printers because it is common that paper printing often includes black as the dominant color. In modern printing technology, the black ink is added to CYM to provide better black hue, to improve the image quality and economize the consumption of the CYM inks.

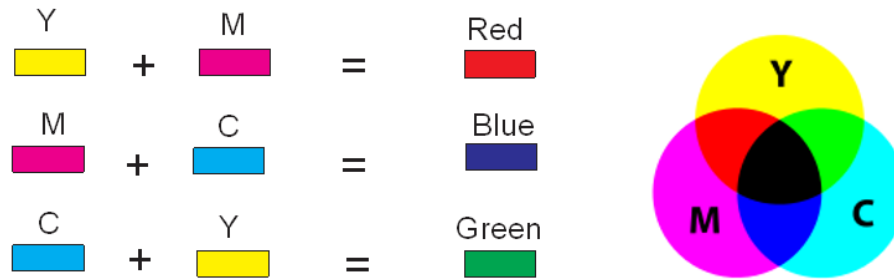


Figure 5.3. Color Composition in Inkjet printing

5.3 The properties of inkjet printing

Beside whole inkjet printing advantages from the economical and technological point of view there are also some drawbacks. Ink properties play a major role in this field. Generally, printable conductive inks exhibit either very low or very high conductivity. Conductive particles, binder and solvents are homogeneously mixed in a solution with viscosity of a jet ink. The solvent of the nano-conductive particles can be simply water [65-72] or even organic solvent [65, 73, 74]. When the ink is free from flocculation it is practically a well-dispersed printable conductive ink.

5.3.1 Surface tension & viscosity

Two physical characteristics of the ink liquid which play a significant influence in inkjet printing process are surface tension and viscosity. According to the surface tension phenomena, the free molecules on the surface of the fluid have higher energy than in the bulk. In fact, the spherical shape of the droplets is due to the low surface energy of a spherical surface than any other shape. Hence, the droplets tend to have spherical form. In printing process of the ink onto the substrate, the surface energy between substrate and ink should be considered. In this

case, the equilibrium of these two surface energies (free surface and the interface surface between ink & substrate) causes the spherical cap shape, as illustrated in figure 5.4.

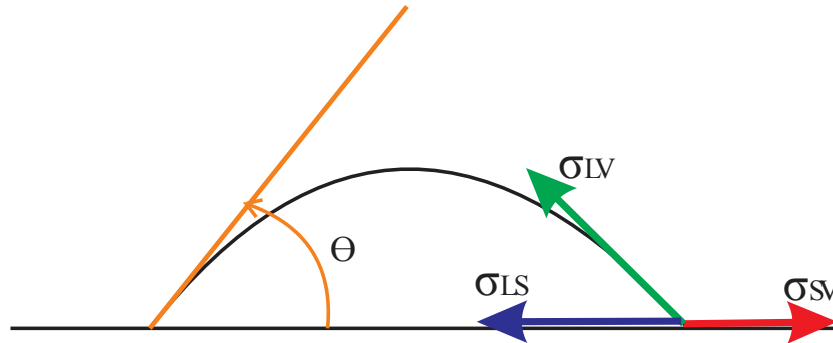


Figure 5.4. Schematic of Surface Energy Equilibrium and contact angle in droplet

According to the figure 5.4, the surface energy between substrate and surrounded environment (σ_{SV}) is resulted from the outcome of first, (i) surface energy between droplet and surrounded environment (σ_{LV}) and second, (ii) surface energy between droplet and substrate (σ_{LS}). The formulation is known as Young equation and is given by:

$$\sigma_{SV} = \sigma_{LS} + \sigma_{LV} \cos \theta_{eqm} \quad (5.1)$$

$$\sigma_{LV} = \frac{\sigma_{SV} - \sigma_{LS}}{\cos \theta_{eqm}} \quad (5.2)$$

The natural tendency of liquid molecules to form the shape with the lowest surface energy causes the guttering effect after ejecting from nozzle in inkjet printing process. This type of instability of ink is known as Lord Rayleigh-Plateau instability phenomena, which was observed and described in 1879.

Actually, the force which stems from the interactions between liquid molecules called as viscous force. As an example, water has dynamic viscosity value around “1 mPa s” at 20° C, while the dynamic viscosity of the inkjet printable liquids are ranging from 2 to 50 “mPa s”⁶. The dynamic viscosity of the ink varies due to the temperature variation, thus modifying the viscosity of the ink droplet is possible by adjusting the print-head temperature.

In fact, the high surface tension and more viscous ink are not eject-able from the nozzle, thus the low viscosity and surface tension are desired. Organic liquids have smaller intermolecular energy in comparison with water, so in case of using water as a solvent for conductive inks, addition of surfactants is necessary. The surfactants molecules are located in the air-water interface which causes huge reduction in cohesive force in water. Thus, the generated lower surface tension enables a more freely spread out of the water based droplets on the substrate.

Figure 5.5 illustrates the comparison between two 12μl droplets without surfactant “condition-A” and in presence of surfactant “condition-B”. In this case ethanol 70% is used as surfactant. The θ – angle is decreased in condition-B, which it means lower surface tension for the droplet. Theoretically, according to the equation (5.2), the surface tension σ_{LV} will decrease by decreasing the θ – angle.

⁶ One milliPascal-second “mPa s” in SI unite is equal to one centipoise “cp” in CGS units

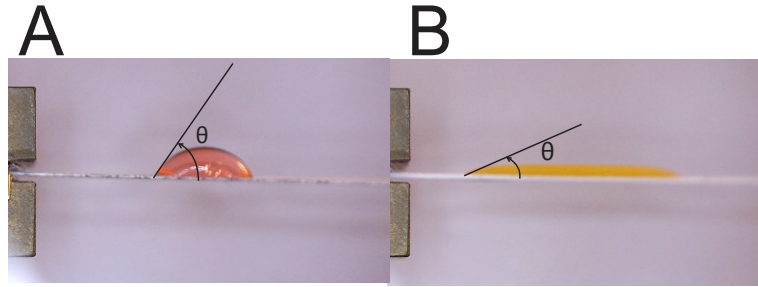


Figure 5.5. Surfactant influence on surface tension (a) 12 μl droplet of water (b) 12 μl droplet of water mixed with ethanol 70%.

5.3.2 Surface resistance

As it is mentioned in section 4.1.1, the recommended resistance range for piezo resistive strain gages is from 120 Ω to around 700 Ω [48]. Thus the resistance of printed conductive ink should be ranging in the above defined standard span. In order to calculate the resistance of the printed resistor, first the “Surface/Sheet Resistance” term should be defined.

$$R = \frac{\rho}{T} \frac{L}{W} \quad (5.3)$$

The resistance formulation is illustrates by the equation (5.3), where the “L & W” are the length and width of the film, respectively. The resistance is directly related to the “bulk resistivity (ρ)” of material and reversely to the thickness of the film “T”. The terms of “ ρ/T ” is known as the sheet resistance.

Typically sheet resistance “ R_s ” is used for measuring the resistance of the thin film with uniform thickness. The common unit for R_s is “ $\Omega/\square/\text{mil}$ ”, which it means sheet resistance in case of equal “L” and “W” (one square) and in uniform thickness value equal to one mil (25.4 μm).

Different companies are providing various types of ink-jet printable inks such as Methode, Mitsubishi, and Ag-IC Electronics. It should be mentioned here that, all ink producers recommend their own fabricated special coated substrates, which inks are only curable upon them. Moreover, the inks should be suitable with printing technology of the used printers. For instance, the Mitsubishi ink may not be printable by Epson printer, which is recommended for Methode inks.

Methode Company, as one of the well-known conductive inkjet-printable ink producer, provides silver and carbon based inks. According to the technical data sheets provided by the company, the inks are inkjet-printable by Epson printer with “5000 $\Omega/\square/\text{micron}$ ” sheet resistance for the carbon ink and “25 miliohms/ \square/micron ” sheet resistance for silver ink. Hence, for a uniform one micron thickness, printed rectangular area “L= 3 mm and W= 1 mm”, the resistances will be 15000 Ω and 0.075 Ω for carbon based and silver based inks, respectively.

As it is mentioned, the targeted range of resistance for our application is between 120 and 700 ohms. Thus the resistance of the printed resistor, even by modifying the rectangular design, will not meet the criteria of the application. The first suggested solution could be mixing the carbon and silver ink. The carbon-based and silver-based ink are full of floating carbon and silver nano-particles, which they have clustering and flocculation potential through mixing process, thus by mixing them some new-born problems will appear, such as clogging of the nozzle during the ejecting ink process. Below, the “Halftoning Theory” is introduced for solving the mixing issue.

5.4 Halftoning

In new-color production techniques in addition of the subtractive method, halftoning is used [75]. Generally, halftone is the reprographic⁷ method that used continuous tone for spreading the dots, which they may vary in size or their inter-dot spaces. Thus as it is illustrated in figure 5.6, they have potential to create gradient trend. Halftoning phenomena enables to produce a wide range of colors that without using this theory, the three principal colors could print only solid color spot, so they can only produce seven colors.

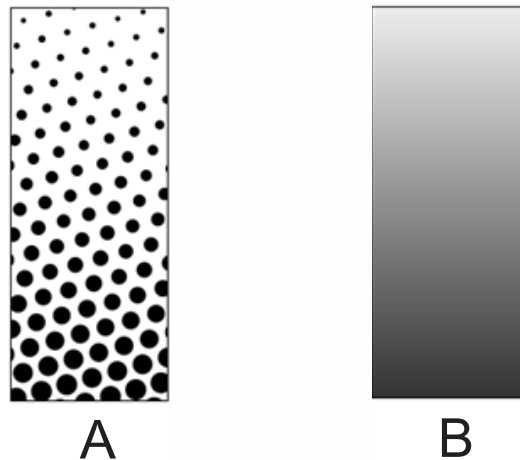


Figure 5.6. Halftone dots. B: Human eye seeing ability from sufficient distance

Three types of common dot placement methods, which are used for creating multiple-color from superimposing single color planes are: dot-on-dot, dot-off-dot and rotated dot. The dot-on-dot technique, places the dots of color on top of the dots of another color. The dot-off-dot technique, places the dot of one color next to another color dot without overlapping. In rotating dot method, the primary dots of colors are arranged in different screen angle with partially overlapping.

⁷ Reprography: re-creating / re-forming the image or graphic by electrical or mechanical means

The rotating method is frequently used as a printing technique. As it is illustrated in figure 5.7, different printing angle are used in this technique. These different screen angles produce partial overlapping, which is useful for electrical connection in case of using conductive inks of different characteristics.

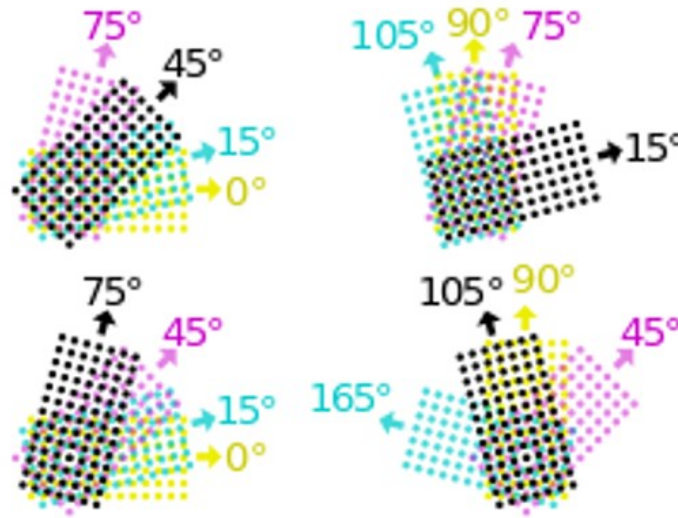


Figure 5.7. The different recommended angles for CMYK (adapted from [64])

By using the halftoning technique, color printing with less than full saturation of primary color is possible. For instance, the pink color produces by printing the magenta color onto the 20% of the area of a large white paper. Thus the halftoning method deposit the dots of magenta ink with larger interface space, such that the 20% of the white paper area will be covered. The printed area is perceived pink for human eyes. The halftone method gives possibility to make three different colors, with the same composition of Cyan, Magenta, Yellow, and Black as illustrated in figure 5.8.

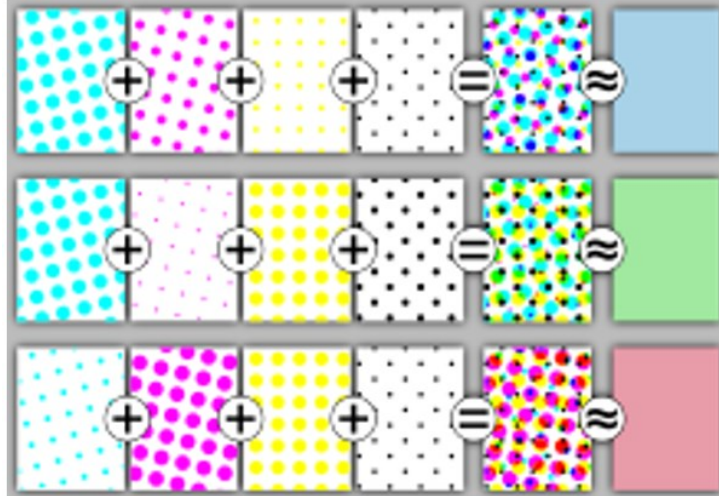


Figure 5.8. Three different color results by the same color composition (Adapted from [64])

5.5 Sensor construction

The main goal of the current study is constructing the piezo-resistive sensors by printing a pattern of silver and carbon conductive dots and providing a network of resistors with the desired total resistance value. Since the recommended resistance for strain sensing applications are not achievable by printing silver and carbon dots separately (section 5.3.2), the halftoning composition theory will be used.

5.5.1 Compatible ink and printer

In field of printed electronics, developing the conductive inks which is digitally printable in a rapid manufacturing process represents a remarkable progress. Due to the importance of the conductive particle size in inkjet printing process, particularly in particle ejecting from the nozzle, some manufacturer such as Methode company are using nano-technology to overcome

this issue. Moreover the viscosity of the selected carbon ⁸and silver⁹ inks are 12 and 3.5 cps, respectively, which is in the acceptable range for the inkjet printing.

The recommended printing technology for nano conductive inks of Methode Company, is drop-on-demand piezo/thermal inkjet technology. In the current study one type of Epson printer, namely “XP620” will be used. The applied printing technology for this type is drop-on-demand piezo inkjet. Moreover, according to the printer catalogue, the minimum ink droplet size is as small as 0.3 picoliters. Thus the diameter of droplet sphere based on (5.4) will be 8.3µm. The droplet diameter is in micron-scale, which is large in comparison with the nano-scale diameter of the conductive-ink particles, such selected to prevent the nozzle clogging.

$$\text{Droplet Sphere volume} = \frac{4}{3} \pi r^3 \Rightarrow r = \sqrt[3]{\frac{0.3 \times 3}{4\pi} \times 10^{-15}} = 4.15 \text{ micron} \quad (5.4)$$

5.5.2 Refillable cartridge and coated sheet

The Epson XP-620 has five ink cartridges, which 5 colors include CMYK and photo-black. The photo-black is used for make the background color in images. According to the policy of the Epson Company, they are not selling the empty refillable cartridges. As it is illustrated in figure 5.9, every cartridge has a reset chip. The duty of reset chip is to provide information about the remaining ink volume in reservoir part. It means that, after finishing the ink, even if one refills the cartridge, it will show as empty for the printer processor. The issue will be solved by auto-reset chip, which is produced by some companies such as InkOwl. In this study the conductive

⁸ The carbon ink from Methode Company. The type name is “3804”

⁹ The silver ink from Methode Company. The type name is “9101”

5.5.3 Printing with conductive ink

One of the most important points in inkjet printing of conductive inks is the cleaning of color inks from the ink channels. It means that the ink passing paths through the printer should be sufficiently clean to avoid color and conductive ink mixing issue. Thus, the original delivered cartridges by manufacturer should not be installed to the printer. Generally the final quality test of the printer run by a manufacturer is one-time test print that could contaminate the ink channels. The issue will be solved by using a solvent which known as cleaning solution. The solvent is a mixed liquid that includes water, glycerol, polyethylene glycol, etc.

First, one set of refillable cartridges (CMYK + photo-black) are filled with cleaning solution. Then the nozzle cleaning option in the printer is activated and it will clean all paths of the five colors by the solvent. Another set of refillable cartridges which assigned to the conductive inks, will be filled according the figure 5.10 by nano-carbon and silver inks.

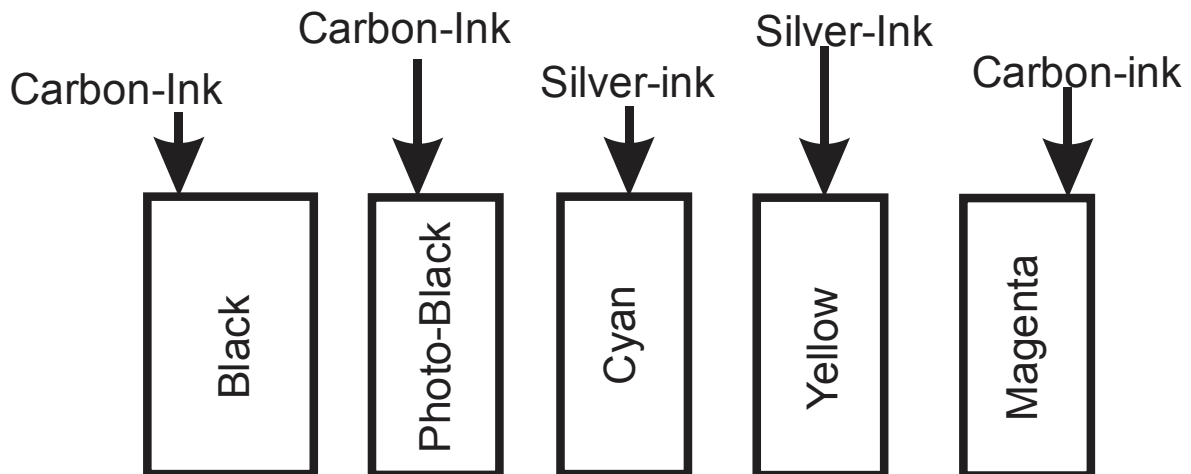


Figure 5.10. Filling five cartridges with carbon and silver inks

The schematic view of the resistor is demonstrated in figure 5.11. The leads of the resistors will be printed by 100% Cyan color, which is nano-silver ink according to the figure 5.10.

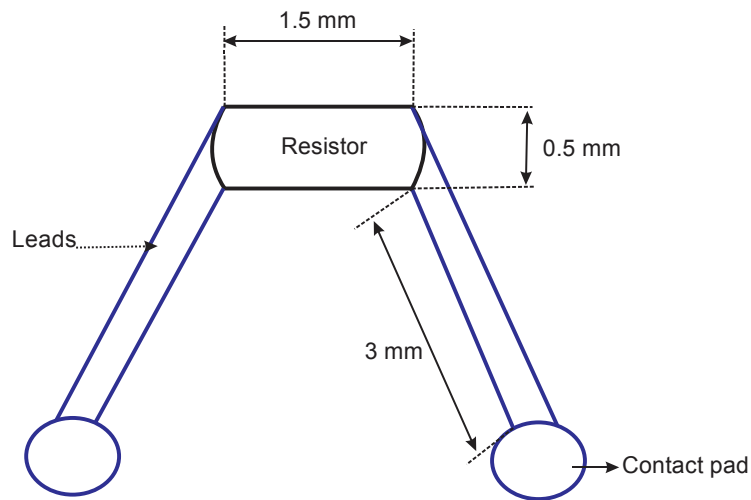


Figure 5.11. The schematic view of the printed resistor

Figure 5.12 illustrates the printed piezo-resistors on coated polyester by different ink compositions. The Corel software provides the capability for adjusting every color percentage in the printed area.

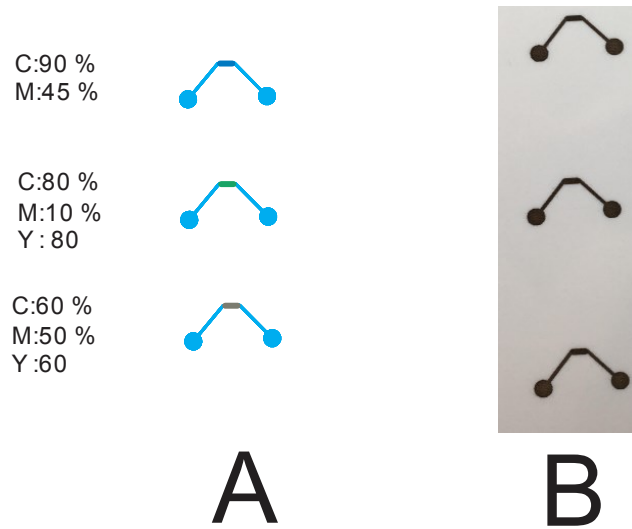


Figure 5.12. A) Color composition on Corel software B) Printed resistors on coated polyester

A remarkable progress can be achieved if one has the ability to print the entire piezoresistive-sensor and Wheatstone-Bridge on a substrate (polyester ring), in one-time printing. Figure 5.13 illustrates the idea, which the V_{in} -electrodes will be connected to DC-power source for supplying the voltage in the circuit. The V_{out} -leads will connect to the monitoring device for recording the voltage variation during the different flow condition. Figure 5.14 shows the fabricated sensor.

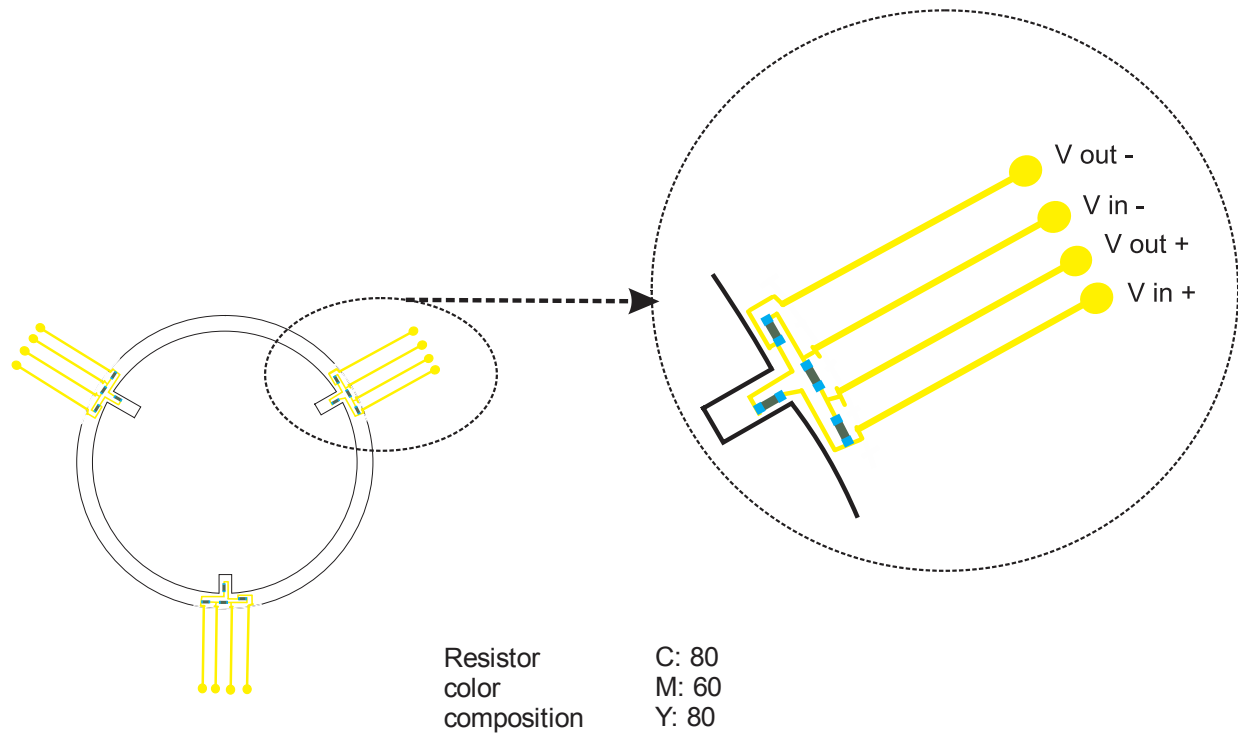


Figure 5.13. The layout design of inkjet printing the sensor and Wheatstone bridge.

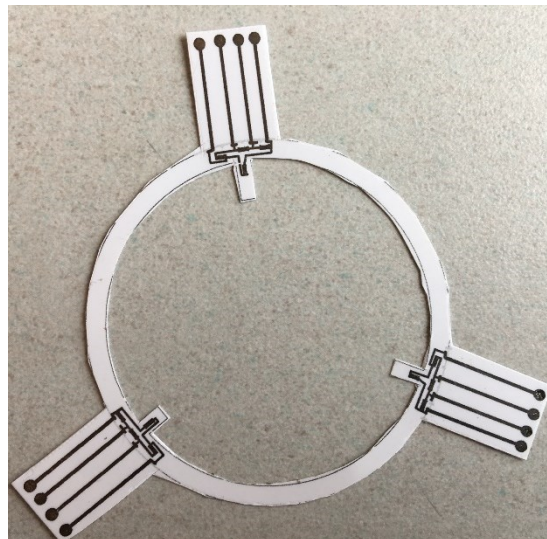


Figure 5.14. The fabricated sensor and Wheatstone-Bridge in one-time inkjet printing

5.5.4 Measurement the achieved resistance

In order to apply the standard method for measuring the resistance of printed resistors, the ASTM standard [76] will be used. In current study the KEITHLEY® multi-meter is used for resistance measurement. The measured resistance of the printed resistor by the ohmmeter, depends on the pressure which applied on the electrode. If the applied pressure is high, the contact surface between printed resistor and electrode will be increased and the monitored resistance will be lower and vice versa. Figure 5.15 illustrates the resistance measurement jig, which the electrodes of the ohmmeter are attached to the lever part of the jig. The applied pressure to the electrode is from the weight of the lever, thus it will be achieved a constant pressure.

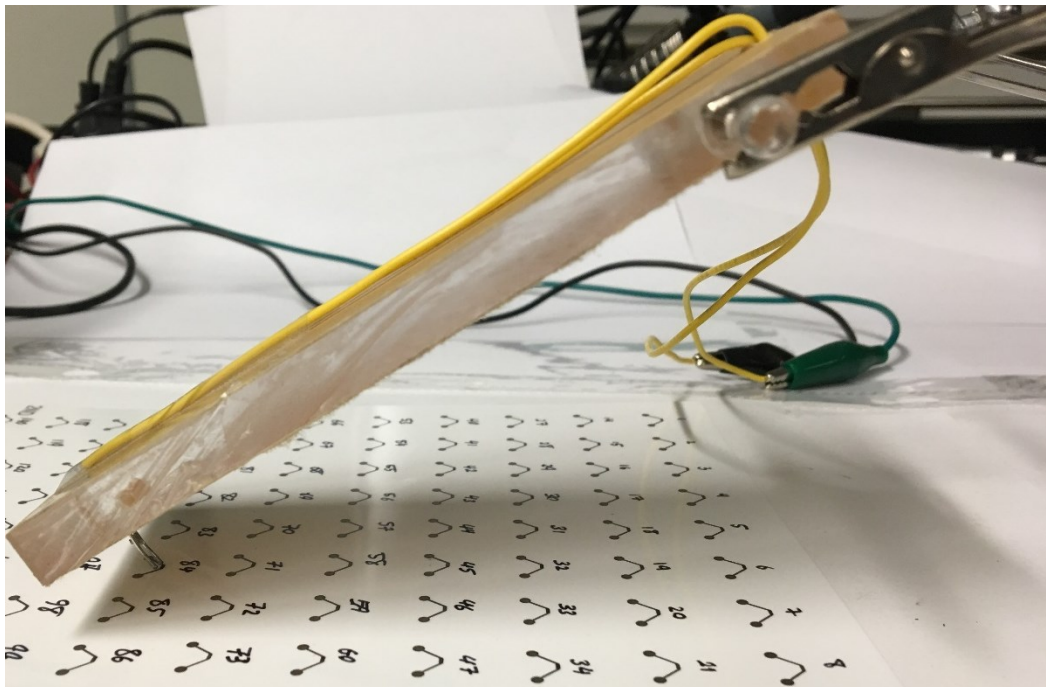


Figure 5.15. The measurement jig of the printed resistors

5.5.5 Gage factor setup and calculation

In order to find the gage factor of the inkjet-printed resistors, three parameters (ΔR , R , ε) should be defined based of the equation (5.5).

$$GF = \frac{\frac{\Delta R}{R}}{\varepsilon} \quad (5.5)$$

Where the ΔR is the resistance variation, R is the nominal resistance and ε is the strain (μ m/m). Theoretical strain equation can be written as below:

$$\varepsilon = \frac{Mc}{EI} \quad (5.6)$$

Where the M is the moment ($N \times m$) and c is the distance of the strain gage position to the centerline of the beam, E is the modulus of elasticity (kN/mm^2), b is the width (mm) and h is the thickness (mm). Figure 5.16 demonstrates the schematic view of cantilever beam under a point load at the tip. The induced deflection at the free-end is given by (5.7).

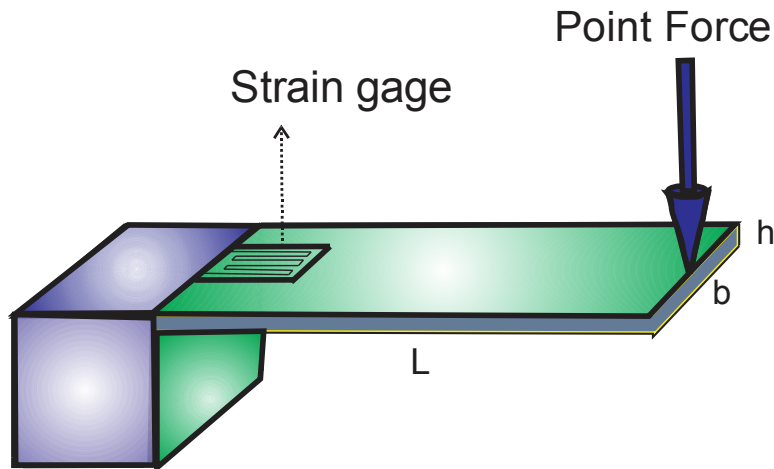


Figure 5.16. The configuration of the cantilever beam under the point load

$$\delta_{\max @ x=L} = \frac{p L^3}{3 EI} \quad (5.7)$$

According to the equation (5.6) and (5.7) in the condition of known deflection value at the free end, the induced strain to the cantilever beam under the point load is written by (5.8).

$$\varepsilon = \frac{(P \times L) c}{EI} = \frac{\left(\frac{\delta \times 3 EI}{L^3} \times L\right) \times \frac{h}{2}}{EI} = \frac{3\delta h}{2L^2} \quad (5.8)$$

Figure 5.17 illustrates the dimensions of the cantilever beam and inkjet-printed U-shape resistor. The thickness of the beam is 0.1mm. In experimental phase the known deflection is applied to the tip of the cantilever beam by a screw. The deflection value is adjustable by twisting the screw.

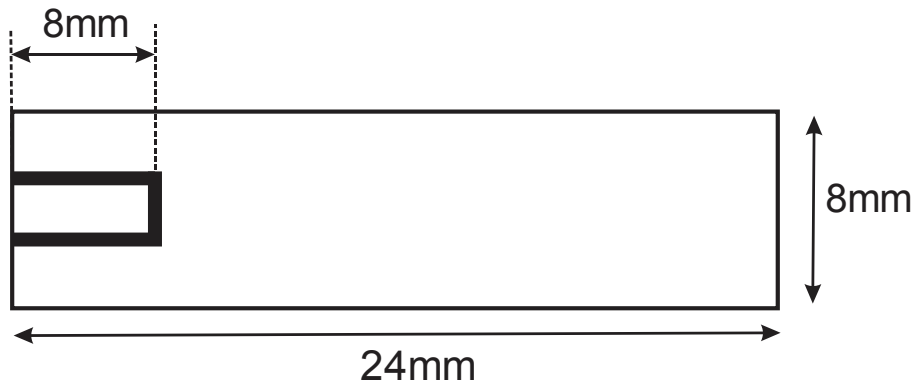


Figure 5.17. Dimensions of the cantilever beam and U-shaped inkjet-printed resistor

The color composition of the investigated resistor is “C 80, M 20, Y 80”, which is illustrated at the figure 5.18. The silver ink is printed from C and Y cartridges. The carbon ink is printed from M-cartridges. The halftoning angle of printing for C, Y and M are 0°, 60° and 30°, respectively. The diameter of the selected dot size for this experiment is 0.2 mm.

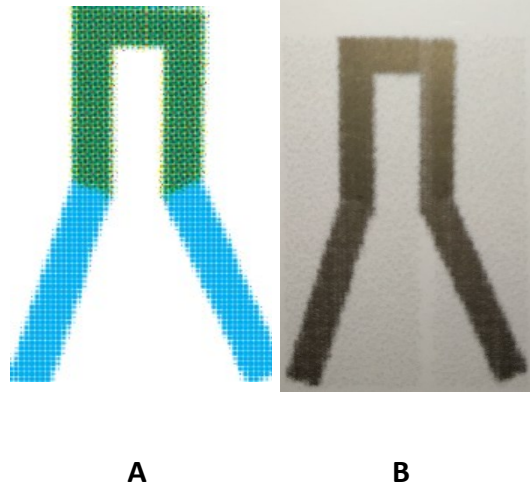


Figure 5.18. The image of the U-shaped resistor A) at the Corel-software B) Inkjet-printed resistor

The figure 5.19 shows the experimental setup. In the condition of 6mm deflection at the tip of the cantilever beam, the resistance of the U-shape resistor is varying from 38.6 Ω to 39.5 Ω . Thus according to the equation (5.8) the induced strain value can be calculated (5.9).

$$\varepsilon = \frac{3\delta h}{2L^2} = \frac{3 \times 0.006 \times 0.0001}{2 \times (0.024)^2} = 0.00156 \quad (5.9)$$

Based on the equation (5.5) the gage factor of the resistor is around 15 (5.10).

$$GF = \frac{\frac{\Delta R}{R}}{\varepsilon} = \frac{\frac{39.5 - 38.6}{38.6}}{0.00156} = 14.95 \quad (5.10)$$

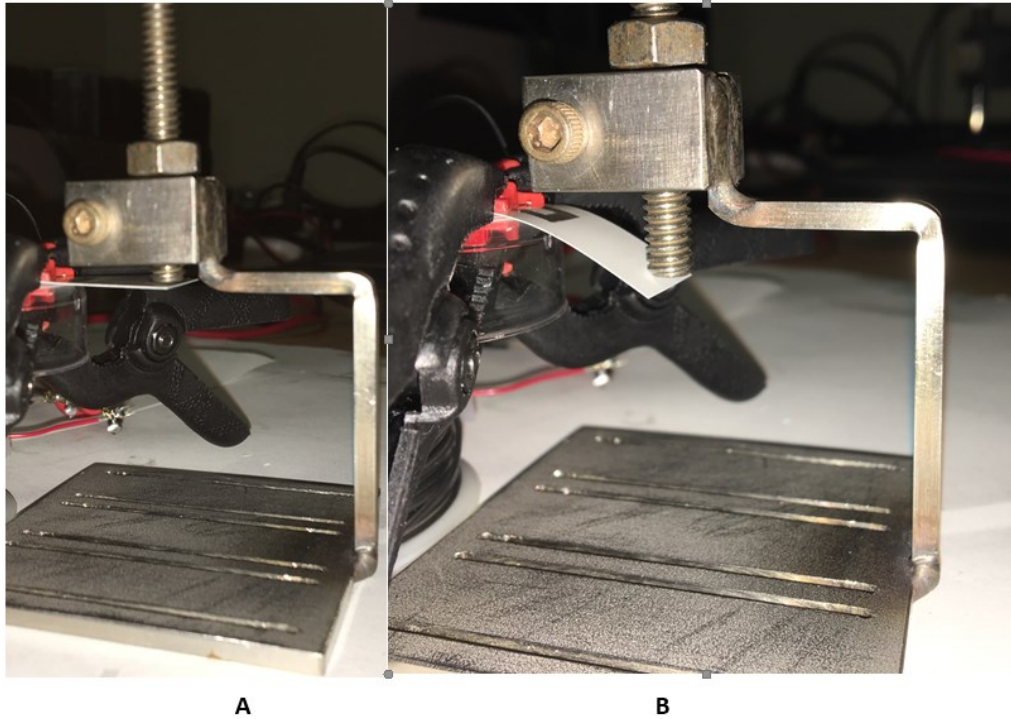


Figure 5.19. The experimental setup for GF-measurement. A) Before deflection B) After deflection

5.6 Experiments and Results

A collection of resistors with 130 different color compositions are inkjet-printed on coated polyester sheets. The carbon ink is printed from K and M cartridges, which their angle of halftoning for this experiment are 15° and 75° , respectively (figure 5.7). The silver ink is printed from C and Y cartridges, which their angle of halftoning in current experiment is 105° and 90° , respectively (figure 5.7).

The printing process is done four times, thus for one color composition, four inkjet-printed resistors are in hand. In this section color compositions are controlled by the Corel-software. The main goal of this process is finding one set of color composition that shows standard

resistivity for sensor applications [48]. Moreover, the resistance of every individual color composition resistors, should be repeatable in different printing process.

Table 5.1. The resistance of the selected color composition at four different printing process

Number of the resistor	Color composition by Corel-software	Resistance (Ω) @ First Printing (i)	Resistance (Ω) @ Second Printing (ii)	Resistance (Ω) @ Third Printing (iii)	Resistance (Ω) @ Forth Printing (iv)
No.1	100% Silver (Y) + 20% Carbon (K)	78	144	100	34
No.2	100% Silver (Y) + 40% Carbon (K)	55	47	33	27
No.3	100% Silver (Y) + 20% Carbon (M)	108	285	228	180
No.4	100% Silver (Y) + 40% Carbon (M)	53	117	45	48
No.5	100% Silver (C) + 20% Carbon (K)	30	25.5	18.3	17.4
No.6	100% Silver (C) + 40% Carbon (M)	28	28	26	23.5
No.7	80% Silver (C) + 80% Silver (Y) + 40% Carbon (K)	35	98	53	43
No.8	80% Silver (C) + 80% Silver (Y) + 40% Carbon (M)	29	39	24	23

The design of the resistors are based on the figure 5.12. Table 5.1 shows eight selected resistors from 130 inkjet-printed resistors. The resistors are named by numbers. As it is illustrated in table 5.1, one individual resistor shows four different resistances in four different

printing processes, thus they are not satisfying our requirements for sensor construction. The resistance of the resistors are measured according to the demonstrated set up illustrated in figure 5.16.

One of the important achievements of this study is illustrated in figure 5.16 and 5.17. The graphs show that in the conditions of the equal carbon and silver percentage, both of the diagrams demonstrate the same trend (5.11). The resistance difference between two diagram stems from different halftoning angle for carbon ink. In one of the investigated color composition in figure 5.20 and 5.21, the carbon is printed from K-cartridge and for the second one, is printed from M-cartridge. Due to the difference printing-angle between K and M cartridges (figure 5.7), the resistance differences is recorded.

$$\text{Resistance}_{@ (i)} < \text{Resistance}_{@ (ii)}$$

$$\text{Resistance}_{@ (ii)} > \text{Resistance}_{@ (iii)} \quad (5.11)$$

$$\text{Resistance}_{@ (iii)} > \text{Resistance}_{@ (iv)}$$

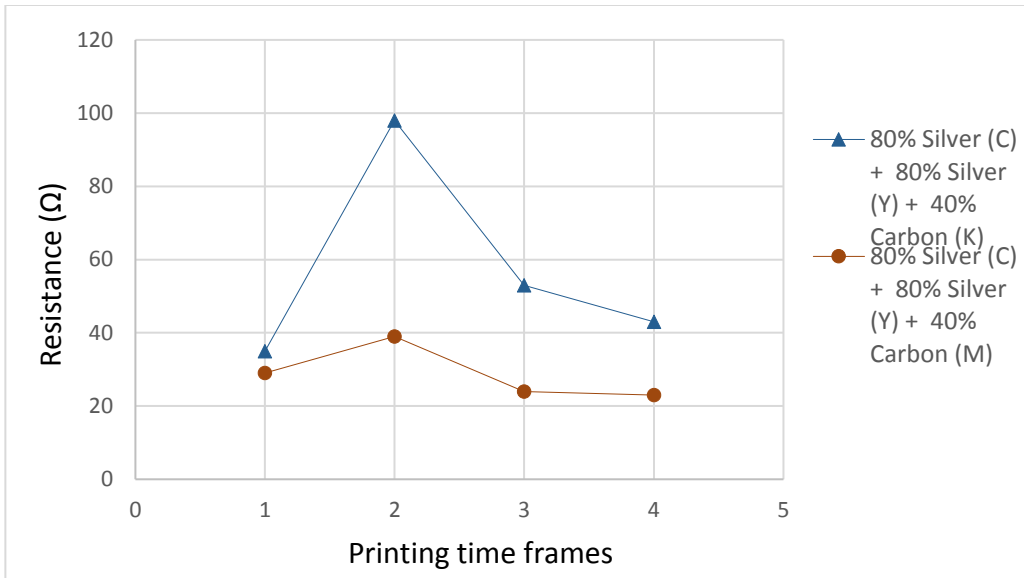


Figure 5.20. Comparison between resistors No. 7 & 8.

Equal carbon and silver percentage by different halftoning for carbon, but the same silver halftoning in both cases

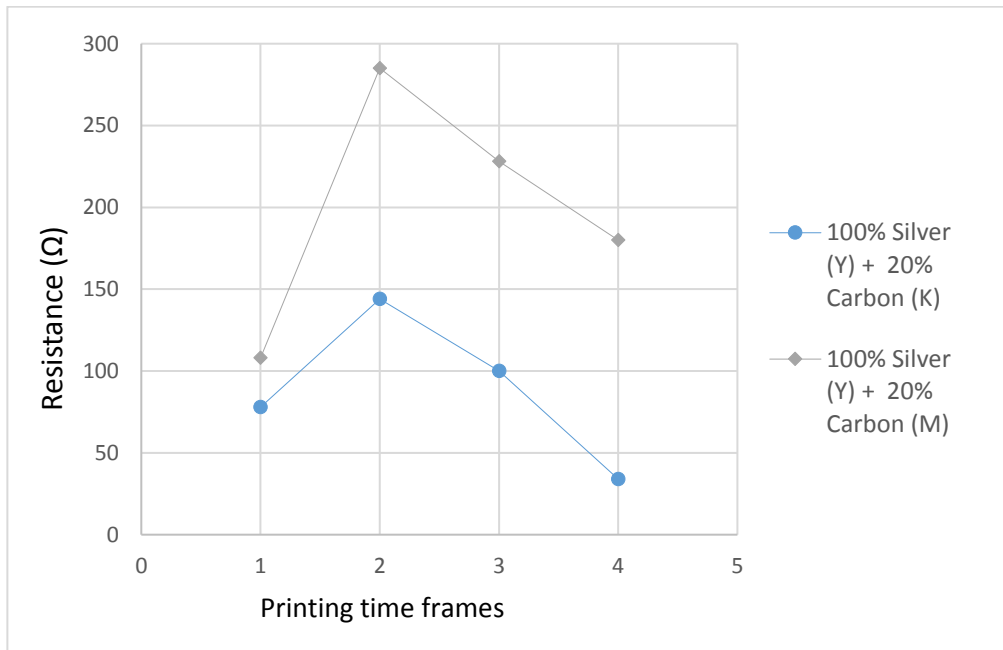


Figure 5.21. Comparison between resistors No. 1 & 3.

Equal carbon and silver percentage by different halftoning for carbon, but the same silver halftoning in both cases

Figure 5.22 shows the above achievement, which in this case the same percentage of carbon and silver are printed, but the silver and carbon halftoning pattern for the first one are Y and K, respectively. For the second one halftoning pattern of the silver and carbon are C and M, respectively.

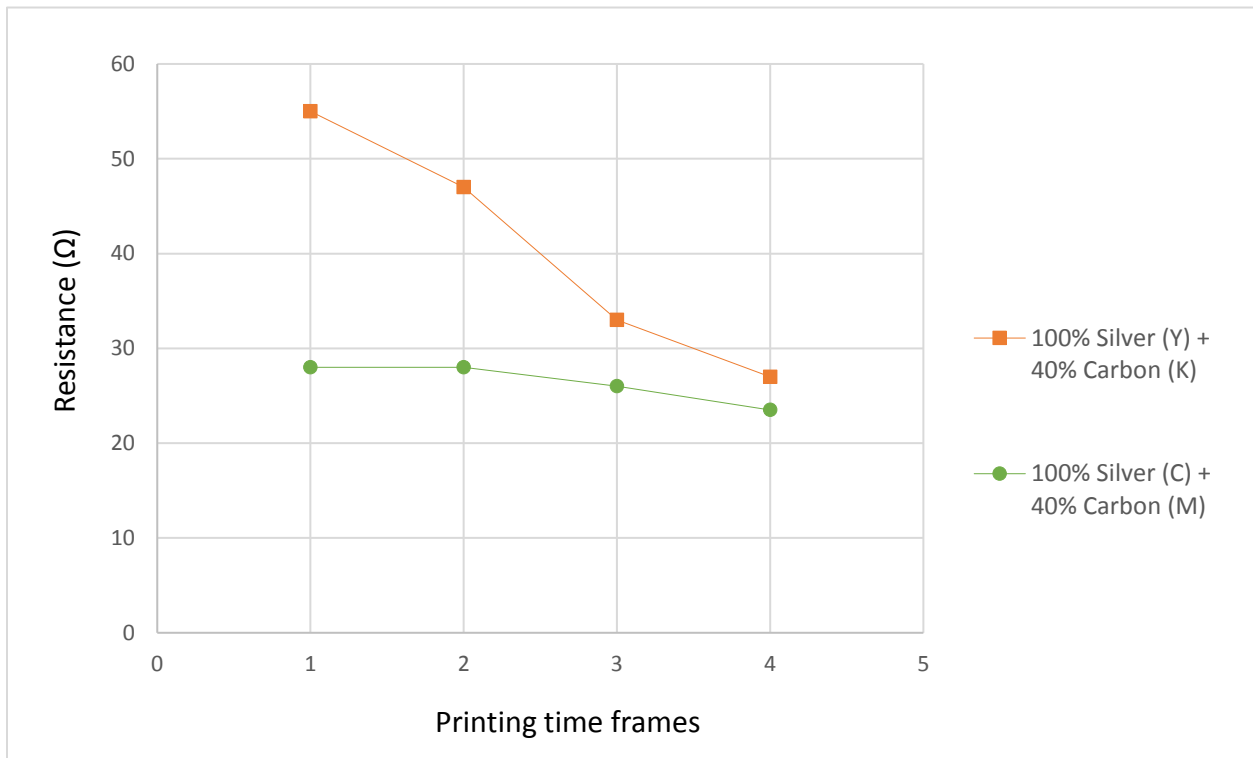


Figure 5.22. Comparison between resistors No. 2 & 6.

Equal carbon and silver percentage by different halftoning for carbon and silver

The microscopic scale investigation yields to another aspect of fabrication. According to this, the microscopic image of the resistors are investigated by image analyzing software such as Imagj. The color of the silver-ink and carbon-ink are metallic-gold and black, respectively. In image analyzing phase, the image will be converted to black and white as illustrated in figure 5.23. The black-zones and white-zones are carbon and silver, respectively.

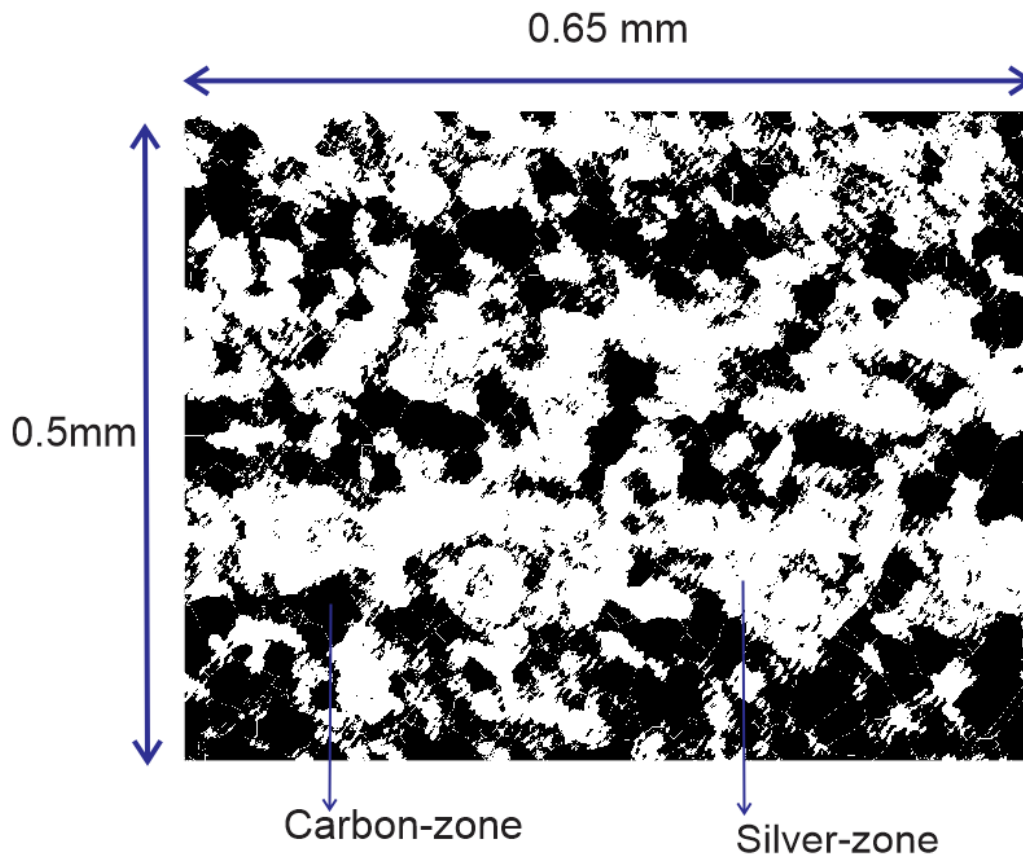


Figure 5.23. The microscopic view of the resistor.

The magnification is 5x and the area of the zones are computed by Imagj

The table 5.2 illustrates the three samples of inkjet-printed resistors that they are selected from the table 5.1. As it is noticed in the table, the user controls of the pattern is done through

the software (Corel). Then the area of the carbon and the area percentage of the carbon over the entire area of the image are computed by Imagj software. The percentage of the color composition in Corel software, represents the covered area percentage by one individual color.

Table 5.2. The three sample resistors analyzed by Imagj

Number of the resistor From Table 5.1	Color composition in Corel-software	Area of the carbon (mm ²)	Area percentage of the carbon	Resistance (Ω)
NO.5 (iv)	100% Silver (C) + 20% Carbon (K)	0.126	38.383	17.3
NO.8 (iv)	80% Silver (C) + 80% Silver (Y) + 40% Carbon (M)	0.128	39.063	23
NO.2 (iv)	100% Silver (Y) + 40% Carbon (K)	0.137	41.989	27

According to the table 5.2, by increasing the carbon percentage in design controlling software (Corel), the area percentage of the carbon will increase. This causes resistance boosting of the resistors.

On the other hand, the comparison between resistance of the resistors No.8 and No.2 shows that, designing and printing of the silver-ink in two different halftones (Resistor No.8), will decrease the area percentage of the carbon. Thus the resistance of the resistor No.8 is less than the resistance of the resistor No.2.

Chapter 6 - Conclusion

This chapter presents the conclusion of the current investigation which was outlined in three sections below. The first section is focusing on general conclusion of the thesis as well as a brief comparison between the fabricated flowmeter in this study and the commercial flowmeter available on the market.

Contribution of the inkjet printing as an alternative method in sensor fabrication field is stated in the second part of the conclusions. The final section is reserved to the possible future works.

6.1 Conclusion

Over the past few decades, considerable attention has been expended to develop different types of flow-meter technologies and devices. Some of these methods are investigated in the second chapter. High pressure drop after passing the metering device and the partial obstruction of the flow are known as the common problems for the majority of the flow-metering devices. The main intention of the current study was attempt to overcome or minimize these particular issues.

In the majority of fluid engineering sources, the entry length distance was suggested 10D for feasible engineering measurement of flow. At the maximum Reynolds number “80000” which is investigated in current research, the error percentage at 10D entry length was around 5.6%. Thus the 14D entrance distance is required for an acceptable error percentage of around 3%. This distance has been suggested in the thesis as an optimal distance to the flow measurement cross-section for sensor position.

The behavior inside the pipe following both analytical and numerical solutions were discussed. Both these solutions indicate that the flow will experience a parabolic velocity profile in one cross-section at the fully flow developed region. In one cross-section of the pipe, the dynamic pressure value which is directly correlated to the velocity, is varying. The collected signals induced by the dynamic pressure variation at three different levels in the same cross-section will be used to reconstruct the parabolic velocity profile.

Since the generated signals from the designed Wheatstone-Bridge circuit board are significantly small, another filtering and amplifying board is added to the system. Theses output

signals are monitored by a sensor software that is written in C# programming language. The area under reconstructed velocity profile correlate to the real flow value with a coefficient “K”. The K is introduced as the correction factor of the designed flowmeter. The predicted flow by the defined K yields acceptable error percentage which is around “ $\cong 5\%$ ”.

Table 6.1 is a comparison between two types of flowmeters from REED Company and the current research flowmeter. The declared error percentage in the catalogue of the REED hot-wire and differential pressure flowmeters are 5% and 2.5%, respectively, which it shows acceptable error percentage for current investigation. Moreover, the developed sensor obstructs around 2% of the cross-section area of the pipe, thus comparable with REED flowmeters. The configuration also yields small disordering and less pressure drop along the pipe. Also, the proposed technique requires low-cost components in small diameter pipes where flow measurement has always been a problem.

Table 6.1. A comparison between two types of flowmeters from REED Company and the current research flowmeter

Maker company/ Model	working principle	probe disordering area (mm²)	percentage of probe disordering area over the cross-section	accuracy	price (\$ CDN)
REED/ IA797	Hot-wire	406.4	5%	5%	568.53
REED/ R3001	Differential pressure	406.4	5%	2.5%	453.24
The current investigated flowmeter	Dynamic pressure	180	2%	(\cong)5%	(\cong) 120

6.2 Contribution to inkjet printing technique as an alternative method of beams

instrumentation

Due to the fabrication difficulties, especially in strain gage mounting on a defined position, inkjet printing of piezoresistive resistors in a pre-determined position on cantilever beam is introduced as an alternative method. The inkjet-printing technique comes with high economic benefits. Easiness and fast-fabrication process are two important parameters which give ability to mass production of low-cost piezoresistive sensors. Thus they have the principal competitive characteristics in disposable sensor market.

The resulting resistance for the different inkjet-printed resistors have been collected and analysed. An investigation on the measured resistances, color composition, and the area percentage of the carbon in microscopic view, proved the presence of some correlations between them, that some of these achievements are presented in chapter 5. Also the gage factor of the inkjet-printed restore was measured. However, more research and experiments are required for implementation of this alternative method as novel disposable sensor production idea. Another aspect that needs to be further considered is the repeatability of the printing.

6.3 Future work

In order to use the designed sensor in the fluid, one layer of hydrophobic materials is required to insulate the sensor from the environment. This cover is suggested for two reasons. First, to prevent the negative effect of fluid on bonding strength between the mounted strain gages and cantilever beam. Second, the electrical connection between fluid and strain gages

may induce some interferences in generated signals, thus misreading may happen in the system.

Some of the temperature variation faced problems can be compensate by substituting the resistors of Wheatstone-Bridges by the same strain gages. On the other hand, temperature changing will cause viscosity variation in the fluid and strain effect on the sensor. Thus designing a system with capability to compensate all temperature variation side-effects, is a suggestable future work.

References

- [1] Liu, Xinyu, Mwangi, Martin, Li, XiuJun, O'Brien, Michael, & Whitesides, George M. (2011). Paper-based piezoresistive MEMS sensors. *Lab on a Chip*, 11(13), 2189-2196.
- [2] Miller, Richard W. (1983). Flow measurement engineering handbook.
- [3] Manshoor, Bukhari bin, Nicolleau, FCGA, & Beck, SBM. (2011). The fractal flow conditioner for orifice plate flow meters. *Flow Measurement and Instrumentation*, 22(3), 208-214.
- [4] De Maagd Donald, R. (1965). Turbine flow meter. *U.S. Patent No. 3,217,539*. Washington, DC: U.S. Patent and Trademark Office..
- [5] Pankanin, Grzegorz L. (2005). The vortex flowmeter: various methods of investigating phenomena. *Measurement science and technology*, 16(3), R1.
- [6] Luker, Graham James. (2011). Positive displacement flow meter. *U.S. Patent Application No. 13/136,307*.
- [7] Van Der Wiel, Appolonius Jacobus. (2010). Calorimetric flow meter. *U.S. Patent No. 7,691,652*. Washington, DC: U.S. Patent and Trademark Office.
- [8] Ueno, Kazuo. (1983). Electromagnetic flow meter. *U.S. Patent No. 4,409,846*. Washington, DC: U.S. Patent and Trademark Office.
- [9] Younger, G. (1973). *U.S. Patent No. 3,745,826*. Washington, DC: U.S. Patent and Trademark Office
- [10] Baker, Roger C. (2005). *Flow measurement handbook: industrial designs, operating principles, performance, and applications*: Cambridge University Press.

- [11] Cengel, Yunus A, Cimbala, John M, & Kanoğlu, M. Fluid mechanics, fundamentals and applications, 2006: McGraw Hill, New York.
- [12] Szanislo, Andrew J. (1975). Experimental and analytical sonic nozzle discharge coefficients for Reynolds numbers up to 8×10^6 . *Journal of Engineering for Power*, 97(4), 521-525.
- [13] Arnberg, BT. (1962). Review of critical flowmeters for gas flow measurements. *Journal of Basic Engineering*, 84(4), 447.
- [14] Eichenhorn, MS, Beauchamp, RK, Harper, PA, & Ward, JC. (1982). An assessment of three portable peak flow meters. *Chest*, 82(3), 306-309.
- [15] Cusick, C. F. (Ed.). (1968). *Flow meter engineering handbook*. Honeywell Automation, Industrial Division.
- [16] Al-Salaymeh, A. (2005). On the convective heat transfer from circular cylinders with applications to hot-wire anemometry. *Int. Journal of Heat and Technology*, 23(2), 109-114.
- [17] King, Louis Vessot. (1914). On the convection of heat from small cylinders in a stream of fluid: determination of the convection constants of small platinum wires with applications to hot-wire anemometry. *Philosophical transactions of the Royal Society of London. series A, containing papers of a mathematical or physical character*, 214, 373-432.
- [18] Sugden, Harry. (1974). Parity check for turbine meter electronic counting instrumentation or the like: *U.S. Patent No. 3,783,248*. Washington, DC: U.S. Patent and Trademark Office.

- [19] Galili, Igal, Kaplan, Dov, & Lehavi, Yaron. (2006). Teaching Faraday's law of electromagnetic induction in an introductory physics course. *American journal of physics*, 74(4), 337-343.
- [20] Huebscher, Werner, & Anliker, Max. (1982). Ultrasonic doppler flowmeters. *U.S. Patent No. 4,324,258*. Washington, DC: U.S. Patent and Trademark Office.
- [21] Fletcher-Haynes, Peter. (1998). Sampling method and apparatus for use with ultrasonic flowmeters. *U.S. Patent No. 5,753,824*. Washington, DC: U.S. Patent and Trademark Office.
- [22] Stillwell, L. W., & Riffle, G. K. (1977). *U.S. Patent No. 4,043,198*. Washington, DC: U.S. Patent and Trademark Office.
- [23] Oddie, Gary Martin. (2016). Coriolis flow meter: *U.S. Patent No. 9,366,559*. Washington, DC: U.S. Patent and Trademark Office.
- [24] Anklin, Martin, Drahm, Wolfgang, & Rieder, Alfred. (2006). Coriolis mass flowmeters: Overview of the current state of the art and latest research. *Flow Measurement and Instrumentation*, 17(6), 317-323.
- [25] Corwon, Michael E, & Oliver, Randy L. (1989). Omega-shaped, coriolis-type mass flow rate meter. *U.S. Patent No. 4,852,410*. Washington, DC: U.S. Patent and Trademark Office.
- [26] Lanfrit, Marco. (2005). Best practice guidelines for handling Automotive External Aerodynamics with FLUENT: Version.

- [27] Shih, Tsan-Hsing, Liou, William W, Shabbir, Aamir, Yang, Zhigang, & Zhu, Jiang. (1995). A new k- ϵ eddy viscosity model for high reynolds number turbulent flows. *Computers & Fluids*, 24(3), 227-238.
- [28] Chiu, Jeng-Jiann, & Chien, Shu. (2011). Effects of disturbed flow on vascular endothelium: pathophysiological basis and clinical perspectives. *Physiological reviews*, 91(1), 327-387.
- [29] Eliahou, S, Tumin, A, & Wygnanski, I. (1998). Laminar-turbulent transition in Poiseuille pipe flow subjected to periodic perturbation emanating from the wall. *Journal of Fluid Mechanics*, 361, 333-349.
- [30] Bhatti, MS, & Shah, RK. (1987). Turbulent and transition flow convective heat transfer in ducts. *Handbook of single-phase convective heat transfer*, 4.1-4.166.
- [31] Weigand, B, Ferguson, JR, & Crawford, ME. (1997). An extended Kays and Crawford turbulent Prandtl number model. *International journal of heat and mass transfer*, 40(17), 4191-4196.
- [32] Zhi-qing, Wang. (1982). Study on correction coefficients of liminar and turbulent entrance region effect in round pipe. *Applied Mathematics and Mechanics*, 3(3), 433-446.
- [33] Maehara, Yuki, Kondo, Masatoshi, & Takahashi, Minoru. (2016). *Study on Stability of Liquid Jet for Liquid Lithium Target of Boron Neutron Capture Therapy (BNCT)*. Paper presented at the 2016 24th International Conference on Nuclear Engineering (pp. V005T15A074-V005T15A074). American Society of Mechanical Engineers.

- [34] Lien, Kim, Monty, JP, Chong, MS, & Ooi, A. (2004). *The entrance length for fully developed turbulent channel flow*. Paper presented at the 15th Australian Fluid Mechanics Conference, (Vol. 15, pp. 356-363)
- [35] Swanson, David A, Tayman, Jeff, & Bryan, TM. (2011). MAPE-R: a rescaled measure of accuracy for cross-sectional subnational population forecasts. *Journal of Population Research*, 28(2-3), 225-243.
- [36] Chaudhary, Monika, & Gupta, Amita. (2009). Microcantilever-based sensors. *Defence Science Journal*, 59(6), 634.
- [37] Singh, M. P. (1974). Entry flow in a curved pipe. *Journal of Fluid mechanics*, 65(3), 517-539.
- [38] Bausells, Joan. (2015). Piezoresistive cantilevers for nanomechanical sensing. *Microelectronic Engineering*, 145, 9-20.
- [39] Kim, Sangkil, Bito, Jo, Jeong, Soyeon, Georgiadis, Apostolos, & Tentzeris, Manos M. (2015). *A flexible hybrid printed RF energy harvester utilizing catalyst-based copper printing technologies for far-field RF energy harvesting applications*. Paper presented at the Microwave Symposium (IMS), 2015 IEEE MTT-S International.
- [40] Beer, Ferdinand P, Johnston, R, Dewolf, J, & Mazurek, D. (1981). *Mechanics of Materials*, McGraw-Hill. New York, 150-233.
- [41] Changizi, M Amin, Stiharu, Ion, & Sahin, Davut Erdem. (2017). *A New Approach for the Non-linear Analysis of the Deflection of Beams Using Lie Symmetry Groups*. Paper presented at the International Conference of Mechatronics and Cyber-Mixmechatronics.

- [42] Liaw, Kai. (2005). *Simulation of flow around bluff bodies and bridge deck sections using CFD* (Doctoral dissertation, University of Nottingham).
- [43] Nagarajan, Vijaisri, Chen, Yitung, Wang, Qiuwang, & Ma, Ting. (2014). Hydraulic and thermal performances of a novel configuration of high temperature ceramic plate-fin heat exchanger. *Applied Energy*, 113, 589-602.
- [44] Jasak, H. (1996). *Error Analysis and Estimation for the Finite Volume Method with Applications to Fluid Flows, 1996*. Ph. D. Thesis, University of London Imperial College.
- [45] MM, Noor, Andrew, P, & Talal, Yusaf. (2013). Detail guide for CFD on the simulation of biogas combustion in bluff-body mild burner.
- [46] Menter, Florian R. (1994). Two-equation eddy-viscosity turbulence models for engineering applications. *AIAA journal*, 32(8), 1598-1605.
- [47] Kuntz, Martin, & Menter, FR. (2004). *Simulation of fluid-structure interactions in aeronautical applications*. Paper presented at the European Congress on Computational Methods in Applied Sciences and Engineering.
- [48] Eren, Halit, & Webster, John G. (2014). *Measurement, Instrumentation, and Sensors Handbook: Spatial, Mechanical, Thermal, and Radiation Measurement*: Taylor & Francis.
- [49] Hoffmann, Karl. (1996). Practical hints for the installation of strain gages. *Applying the Wheatstone Bridge Circuit, Documentation of HBM*.
- [50] Groupe, Vishay Precision. (09-Jul-2013). Noise Control in Strain Gage Measurements. Tech Note TN-501-502.
- [51] Yang, Li, Zhang, Rongwei, Staiculescu, Daniela, Wong, CP, & Tentzeris, Manos M. (2009). A novel conformal RFID-enabled module utilizing inkjet-printed antennas and carbon

- nanotubes for gas-detection applications. *IEEE Antennas and Wireless Propagation Letters*, 8, 653-656.
- [52] Li, Juntao, Lei, Wei, Zhang, Xiaobing, Zhou, Xuedong, Wang, Qilong, Zhang, Yuning, & Wang, Baoping. (2003). Field emission characteristic of screen-printed carbon nanotube cathode. *Applied surface science*, 220(1), 96-104.
- [53] Liu, Chao-Xuan, & Choi, Jin-Woo. (2009). Patterning conductive PDMS nanocomposite in an elastomer using microcontact printing. *Journal of Micromechanics and Microengineering*, 19(8), 085019.
- [54] Jones, Carissa S, Lu, Xuejun, Renn, Mike, Stroder, Mike, & Shih, Wu-Sheng. (2010). Aerosol-jet-printed, high-speed, flexible thin-film transistor made using single-walled carbon nanotube solution. *Microelectronic Engineering*, 87(3), 434-437.
- [55] Vaillancourt, Jarrod, Zhang, Haiyan, Vasinajindakaw, Puminun, Xia, Haitao, Lu, Xuejun, Han, Xuliang, Stroder, Mike. (2008). All ink-jet-printed carbon nanotube thin-film transistor on a polyimide substrate with an ultrahigh operating frequency of over 5 GHz. *Applied Physics Letters*, 93(24), 444.
- [56] Ha, Mingjing, Xia, Yu, Green, Alexander A, Zhang, Wei, Renn, Mike J, Kim, Chris H, . . . Frisbie, C Daniel. (2010). Printed, sub-3V digital circuits on plastic from aqueous carbon nanotube inks. *ACS nano*, 4(8), 4388-4395.
- [57] Zhou, Yangxin, Hu, Liangbing, & Grüner, George. (2006). A method of printing carbon nanotube thin films. *Applied physics letters*, 88(12), 123109.
- [58] Tortorich, Ryan P, & Choi, Jin-Woo. (2013). Inkjet printing of carbon nanotubes. *Nanomaterials*, 3(3), 453-468.

- [59] Chow, Edith, Herrmann, Jan, Barton, Christopher S, Raguse, Burkhard, & Wieczorek, Lech. (2009). Inkjet-printed gold nanoparticle chemiresistors: influence of film morphology and ionic strength on the detection of organics dissolved in aqueous solution. *Analytica Chimica Acta*, 632(1), 135-142.
- [60] Zhao, Ni, Chiesa, Marco, Sirringhaus, Henning, Li, Yuning, Wu, Yiliang, & Ong, Beng. (2007). Self-aligned inkjet printing of highly conducting gold electrodes with submicron resolution. *Journal of applied physics*, 101(6), 064513.
- [61] Kim, Dongjo, & Moon, Jooho. (2005). Highly conductive ink jet printed films of nanosilver particles for printable electronics. *Electrochemical and Solid-State Letters*, 8(11), J30-J33.
- [62] Lee, SH, Shin, KY, Hwang, JY, Kang, KT, & Kang, HS. (2008). Silver inkjet printing with control of surface energy and substrate temperature. *Journal of micromechanics and microengineering*, 18(7), 075014.
- [63] Yang, Shixuan, & Lu, Nanshu. (2013). Gauge factor and stretchability of silicon-on-polymer strain gauges. *Sensors*, 13(7), 8577-8594.
- [64] Kipphan, Helmut. (2001). *Handbook of print media: technologies and production methods*: Springer Science & Business Media.
- [65] Ham, Hyeong Taek, Choi, Yeong Suk, & Chung, In Jae. (2005). An explanation of dispersion states of single-walled carbon nanotubes in solvents and aqueous surfactant solutions using solubility parameters. *Journal of Colloid and Interface Science*, 286(1), 216-223.

- [66] Islam, MF, Rojas, E, Bergey, DM, Johnson, AT, & Yodh, AG. (2003). High weight fraction surfactant solubilization of single-wall carbon nanotubes in water. *Nano letters*, 3(2), 269-273.
- [67] Liu, Jie, Rinzler, Andrew G, Dai, Hongjie, Hafner, Jason H, Bradley, R Kelley, Boul, Peter J, Huffman, Chad B. (1998). Fullerene pipes. *Science*, 280(5367), 1253-1256.
- [68] Moore, Valerie C, Strano, Michael S, Haroz, Erik H, Hauge, Robert H, Smalley, Richard E, Schmidt, Judith, & Talmon, Yeshayahu. (2003). Individually suspended single-walled carbon nanotubes in various surfactants. *Nano letters*, 3(10), 1379-1382.
- [69] O'connell, Michael J, Bachilo, Sergei M, Huffman, Chad B, Moore, Valerie C, Strano, Michael S, Haroz, Erik H, Kittrell, Carter. (2002). Band gap fluorescence from individual single-walled carbon nanotubes. *Science*, 297(5581), 593-596.
- [70] O'Connell, Michael J, Boul, Peter, Ericson, Lars M, Huffman, Chad, Wang, Yuhuang, Haroz, Erik, Smalley, Richard E. (2001). Reversible water-solubilization of single-walled carbon nanotubes by polymer wrapping. *Chemical physics letters*, 342(3), 265-271.
- [71] Zhang, Xiefei, Liu, Tao, Sreekumar, TV, Kumar, Satish, Moore, Valerie C, Hauge, Robert H, & Smalley, Richard E. (2003). Poly (vinyl alcohol)/SWNT composite film. *Nano letters*, 3(9), 1285-1288.
- [72] Zheng, Ming, Jagota, Anand, Semke, Ellen D, Diner, Bruce A, Mclean, Robert S, Lustig, Steve R, Tassi, Nancy G. (2003). DNA-assisted dispersion and separation of carbon nanotubes. *Nature materials*, 2(5), 338-342.

- [73] Ausman, Kevin D, Piner, Richard, Lourie, Oleg, Ruoff, Rodney S, & Korobov, Mikhail. (2000). Organic solvent dispersions of single-walled carbon nanotubes: toward solutions of pristine nanotubes. *The Journal of Physical Chemistry B*, 104(38), 8911-8915.
- [74] Nguyen, Thi Thuy, Nguyen, Sy Uan, Phuong, Dinh Tam, Nguyen, Duc Chien, & Mai, Anh Tuan. (2011). Dispersion of denatured carbon nanotubes by using a dimethylformamide solution. *Advances in natural sciences: nanoscience and nanotechnology*, 2(3), 035015.
- [75] Kang, Henry R. (1999). *Digital color halftoning*: SPIE press.
- [76] ASTM. (2004). Test Method for Determining the Electrical Resistivity of a Printed Conductive Material. *F 1896-98*.

Appendix A

Small Deflection

According to the equation (3.19), the below equations are achievable. Where the V , M and θ are the transverse shear force , bending moment ,and slop of the elastic curve, respectively [40].

$$EI \frac{d^3y}{dx^3} = V \quad (A.1)$$

$$EI \frac{d^2y}{dx^2} = M \quad (A.2)$$

$$\frac{dy}{dx} = \theta \quad (A.3)$$

The figure A.1 represents the defined boundary conditions at the both ends of beam. The bending moment and the transverse shear force at the tip of cantilever beam are zero. Also, the deflection and the slop of the fixed end are zero.

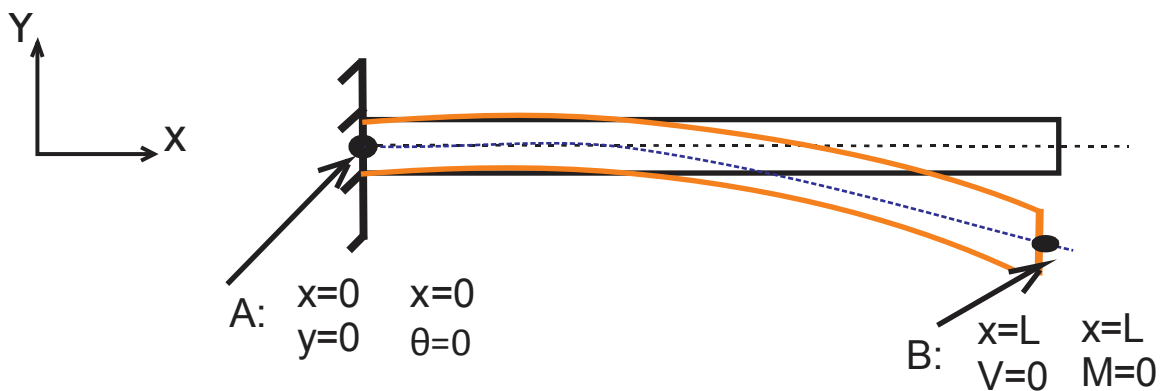


Figure A.1. The boundary condition at the both ends of cantilever beam

The figure A.2 illustrates the geometrical relationship between q and z (A.4), where the term z is the value of distributed load in x distance from the fixed end of cantilever beam. Based

on (A.4) the value of distributed load at the fixed end is zero and it gradually increases until the free end of the beam, which is equal to q .

$$\frac{q_0}{L} = \frac{z}{x} \rightarrow z = \frac{q_0}{L} x \quad (\text{A.4})$$

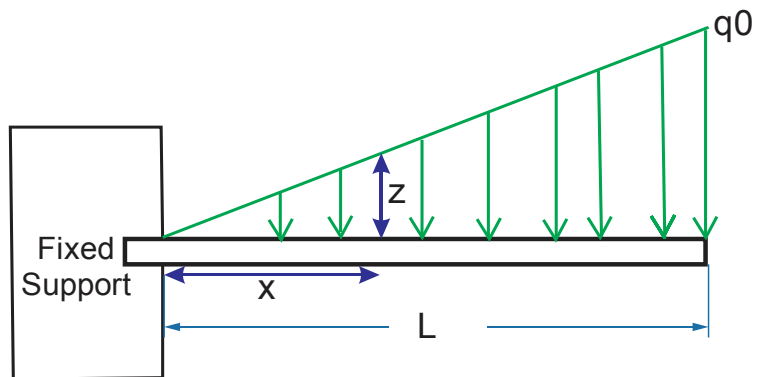


Figure A.2. The geometric relationship between q_0 and z .

According to the equation (A.4), the $q(x)$ term in the equation (3.19) is " $q(x) = -(x/L) q_0$ ". By integrating the equation (3.19), the shear force equation is achievable (3.25).

$$EI \frac{d^4 y}{dx^4} = -\frac{x}{L} q_0 \quad (\text{A.5})$$

$$V = EI \frac{d^3 y}{dx^3} = -\frac{q_0}{L} \frac{x^2}{2} + C_1 \quad (\text{A.6})$$

By substituting the known boundary condition at the tip " $V_{x=L}=0$ ":

$$C_1 = \frac{q_0 L}{2} \quad (\text{A.7})$$

The C_1 will replace to the (A.6) and then will integrate for the second time (A.8).

$$M = EI \frac{d^2 y}{dx^2} = -\frac{q_0}{L} \frac{x^3}{6} + \frac{q_0 L}{2} x + C_2 \quad (\text{A.8})$$

The figure A.1 illustrates the known value for the moment at the tip, which is zero. The constant C_2 will be found by substituting the boundary condition in (A.8).

$$C_2 = -\frac{q_0 L^2}{3} \quad (\text{A.9})$$

By substituting the C_2 in the (A.8) and integrating the equation one will obtain:

$$EI \frac{dy}{dx} = -\frac{q_0}{L} \frac{x^4}{24} + \frac{q_0 L}{4} x^2 - \frac{q_0 L^2}{3} x + C_3 \quad (\text{A.10})$$

At the fixed end of cantilever beam “ $x=0$ ”, the slope of bending curve is zero. By substituting this condition in (A.10), the C_3 will be zero. The final integrating phase will yield to the relation in (A.11).

$$EI y = -\frac{q_0}{L} \frac{x^5}{120} + \frac{q_0 L}{12} x^3 - \frac{q_0 L^2}{6} x^2 + C_4 \quad (\text{A.11})$$

The C_4 will be zero by substituting the zero-deflection value at the fixed end of the cantilever beam. Finally the deflection equation can be written as following:

$$y = -\frac{q_0}{6EI} \left[\frac{x^5}{20L} + \frac{L}{2} x^3 - L^2 x^2 \right] \quad (\text{A.12})$$

According to the (A.10) and (A.12) the slope and the maximum deflection at the tip are given by:

$$\delta_{\max} = y_{x=L} = -\frac{11q_0 L^4}{120 EI} \quad (\text{3.32})$$

$$\theta = \frac{dy}{dx} = -\frac{q_0 L^3}{8 EI} \quad (\text{3.33})$$

Appendix B

Large deflection

According to the [41], in the large deflection condition the slope and the elastic deflection curve are given by :

Slope of the elastic curve:

$$\theta(x) = \frac{dy}{dx} = \frac{\int M(x)dx + C_1}{\sqrt{-(\int M(x)dx)^2 - 2C_1 \int M(x)dx - C_1^2 + (EI)^2}} \quad (\text{B.1})$$

Elastic deflection curve:

$$y(x) = \int \frac{\int M(x)dx + C_1}{\sqrt{-(\int M(x)dx)^2 - 2C_1 \int M(x)dx - C_1^2 + (EI)^2}} dx + C_2 \quad (\text{B.2})$$